



DISSERTATION

Analysis of coupled coated conductors for fusion magnet applications

Ausgeführt zum Zwecke der Erlangung
des akademischen Grades eines
Doktors der technischen Wissenschaften
unter der Leitung von

Univ.Prof. Dr.phil. Dr.h.c. H. W. Weber
E141

Atominstitut

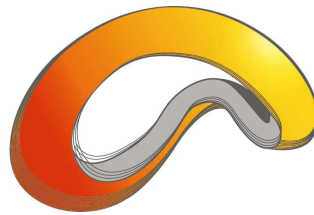
eingereicht an der Technischen Universität Wien
Fakultät für Physik

von

Dipl.-Ing. Johann Emhofer
Matrikelnummer: e0025752
Lavendelweg 15
1220 Wien

Wien, am 29. Mai 2012

This work was supported in part by the



Friedrich Schiedel Foundation for Energy Technology, Vienna

by the

Commission for the Coordination of Nuclear Fusion Research in Austria

and by the



**European Communities under the Contract of Association between EURATOM
and the Austrian Academy of Sciences**

It was carried out within the framework of the European Fusion Development Agreement. The views and opinions expressed herein do not necessarily reflect those of the European Commission.

Danksagung (Acknowledgement)

Ich möchte mich bei Prof. Harald Weber für die fortwährende Unterstützung seit meiner ersten Projektarbeit am Atominstitut bedanken. Durch die von ihm geschaffenen Rahmenbedingungen, konnte ich während meiner Dissertation größtenteils meinen eigenen Weg gehen und mich dadurch, nicht nur fachlich, weiterentwickeln.

Michi, ich danke dir für die Geduld bei fachlichen Diskussionen und für unzählige Text-Korrekturen. Viele Dinge hätten durch deine zündenden Ideen bei weitem nicht so gut realisiert werden können.

Franz, danke für viele interessante morgendliche Gespräche und dass du dir immer Zeit genommen hast, wenn man mit einer Problemstellung zu dir gekommen ist.

Einige Messungen, bzw. Experimente, die in dieser Arbeit gezeigt werden, entstanden unter Mithilfe von Projektarbeiten von Alex, Martin J. und Jasmin, sowie einer Diplomarbeit von Ventsi. Bei euch möchte ich mich für euren Einsatz und euer selbstständiges Arbeiten bedanken.

In den letzten Jahren durfte ich mir das Büro unter anderem mit Martin teilen. Martin, ich hoffe, dass du diese gemeinsame Zeit in ebenso guter Erinnerung behältst wie ich.

Florian, danke für die vielen hilfreichen Ideen, deine tatkräftige Unterstützung und für viele interessante Gespräche über Themen abseits der Physik.

Bei der Montage von radioaktiven Proben haben mir Rainer und Michaela während vieler Stunden assistiert. Danke, dass ihr euch immer die Zeit genommen habt.

Bei allen anderen Kollegen der Arbeitsgruppe, allen voran Thomas, Enric und Harald Fil-lunger möchte ich mich für die gute Zusammenarbeit bedanken.

Mike, Nick, Rod, Christian, Nathan and Ben always supported me during my research stay in New Zealand. Thanks for all.

Furthermore, I wish to thank American Superconductor (AMSC), SuperPower Inc., Industrial Research Limited (IRL) and Karlsruhe Institute of Technology (KIT) for providing us with their state-of-the-art coated conductors and Roebel cables.

Bei unserem Werkstättenteam Barbara, Herbert, Rudi und Andi möchte ich mich für die Zusammenarbeit und die hilfreichen Ratschläge bei technischen Problemen bedanken.

Ebenso möchte ich mich an dieser Stelle bei meinen Freunden und meiner Familie, allen voran meiner Freundin Christine bedanken. Dank eurem Rückhalt ist es mir möglich, in auch noch so stressigen Zeiten, mit Freude meiner Arbeit nachzugehen. Etwas wertvolleres kann man sich im Leben nicht mehr wünschen!

Kurzfassung

In den letzten Jahren zeigten Studien über die mögliche Verwendung technischer Hochtemperatursupraleiter (Bandleiter) für zukünftige Fusionskraftwerksspulen durchwegs positive Ergebnisse. Nach der Bestrahlung mit Neutronen erreichten Bandleiter annähernd gleiche kritische Stromdichten und Temperaturen wie im unbestrahlten Zustand. Das Einbringen künstlicher Verankerungszentren durch Neutronenbestrahlung, deren Größe ungefähr der Kohärenzlänge des Supraleiters entspricht, führte sogar zu größeren Verankerungskräften im Supraleiter und dadurch zu höheren kritischen Strömen bei hohen Feldern.

Zur Verwendung in zukünftigen Magnetspulen, müssen die Bandleiter zu Kabeln verarbeitet werden. Eines der erfolversprechendsten Kabelkonzepte ist das Roebelkabel. Der Stromfluss zwischen gekoppelten Einzelleitern in einem Roebelkabel, sowie die Wechselstromverluste verursacht durch gekoppelte Schleifen, sind bisher jedoch noch nicht gänzlich verstanden.

Weiters wurden die mechanische Zugfestigkeit und die Abhängigkeit des kritischen Stroms von der mechanischen Zugspannung bisher nie an bestrahlten Proben untersucht. Aus diesen und anderen Gründen ist die Eignung von Bandleitern bzw. von Roebelkabeln in Fusionsspulen nach wie vor ungeklärt. Einige dieser Fragen sollen mit Hilfe dieser Arbeit geklärt werden.

Supraströme sollten die Möglichkeit haben, Defekte in einem einzelnen Leiter zu umfließen, weshalb die Einzelleiter eines Roebelkabels resistiv verbunden werden sollten. Diese Verbindungen bilden jedoch geschlossene Schleifen, wodurch in Wechselfeldern Kopplungsströme induziert werden, die wiederum zu Wechselstromverlusten führen.

Bisher wurden Roebelkabel mittels verschiedener Techniken gekoppelt, ohne allerdings Einzelheiten des lokalen Stromflusses zu untersuchen. In dieser Arbeit wurden deshalb Einzelleiter eines Roebelkabels in verschiedenster Weise miteinander gekoppelt und untersucht. Zusätzlich wurde ein Modell zur Berechnung der Wechselstromverluste bei niedrigen und hohen Feldern erstellt. Verlustmessungen an den gekoppelten Proben, sowie zeit-aufgelöste Messungen der lokalen Felder zeigten gute Übereinstimmung mit den theoretischen Modellen.

Weiters wurde ein Inversionsalgorithmus geschrieben, mit dessen Hilfe man den lokalen Stromfluss und die Wechselstromverluste aus der Messung des lokalen Feldes berechnen kann.

Die lokale Stromverteilung während einer Zeitperiode konnte dadurch aus Messungen der lokalen Feldverteilung berechnet werden. Sowohl Feldverteilung als auch Stromverteilung wurden in Bezug auf schwach-, mittel- und stark gekoppelte Zustände in Wechselfeldern untersucht. Es zeigte sich, dass die Breite der Bänder (wie auch der Widerstand der Verbindungen, Frequenz,...) eine kritische Größe für die induzierten Ströme sowie für die Verluste darstellt.

Wie schon in vorhergehenden Arbeiten wurden aktuelle Bandleiter vor und nach Neutronenbestrahlung charakterisiert, um den Fortschritt in der Entwicklung der Materialien nicht aus den Augen zu verlieren. In dieser Arbeit wurde erstmals eine deutliche Reduzierung der kritischen Stromdichte J_c und der kritischen Temperatur T_c in einem Bandleiter nach der

Bestrahlung beobachtet.

Ein Zugversuchsaufbau für Bandleiter, mit dem die Abhängigkeit des kritischen Stromes von der Zugspannung gemessen werden kann, wurde im Rahmen dieser Arbeit entwickelt. Winkel aufgelöste Messungen in Magnetfeldern bis 1.4 T wurden bei angelegten Zugspannungen realisiert. Die weltweit ersten Zugversuche an Bandleitern nach einer Neutronenbestrahlung demonstrierten außergewöhnliche mechanischen Eigenschaften der Bandleiter. Des Weiteren erhöhte sich die Sensitivität von I_c bezüglich der Zugspannung in einem Bandleiter deutlich nach der Bestrahlung.

Die Ergebnisse zeigen viel-versprechende Aussichten für die Verwendung von HTS-Bandleitern in zukünftigen Fusionsspulen. Um jedoch allen Anforderungen einer Fusionsspule gerecht zu werden, sind weitere substanzielle Entwicklungen von Bandleitern und Kabeln notwendig.

Abstract

In recent years several studies on the usability of technical high temperature superconductors (coated conductors) for future fusion power plants reported promising results. Neutron irradiation to the expected fluence has not shown significant reductions in critical currents and temperatures. On the contrary, the introduction of defects with a size matching the superconducting coherence length has led to enhanced flux pinning. Nowadays, manufacturers are trying to introduce artificial pinning centres during the fabrication process in order to achieve the same pinning force enhancement. Coated conductors have to be assembled somehow for engineering high field magnet coils and therefore powerful cables are needed. The Roebel Assembled Coated Conductor - concept (RACC or Roebel-cable) and/or Rutherford cables are promising options for such cables.

Many questions about inter strand coupling and therefore about AC losses in Roebel cables have not yet been answered. Furthermore, mechanical stress, critical current and temperature behaviour of state-of-the-art coated conductors before and after neutron irradiation are unknown. Therefore, the usability of Roebel cables made of coated conductors for fusion applications is still open. Important issues for the development of suitable cables are addressed in this work.

Super-currents should be able to bypass defects in single strands of a superconducting Roebel-cable. Therefore, resistive connections between these strands are needed. These connections form closed loops and coupling currents induced by external AC fields lead to additional losses.

Strands of Roebel cables were coupled by different techniques in the last years and were measured without a detailed knowledge about the mechanisms in the resistively connected superconducting loops. Therefore, different coupling situations with different geometries have been realised in this study. Models for AC losses at low and high fields were developed in order to calculate the induced currents and their resulting losses. AC loss measurements and time resolved maps of the local field penetration confirm the model calculations. An inversion algorithm was written for the calculation of the local current flow and the global AC losses from the field penetration. Current and field distributions have been mapped in detail during one AC cycle for uncoupled, fully coupled and intermediate situations. This study shows that the width (besides the resistive joints, frequency, ...) of the coated conductor plays a crucial role for the induced currents and consequently for their losses.

Similar to previous work, state-of-the-art coated conductors have been measured before and after neutron irradiation in order to monitor recent developments. For the first time a significant reduction of J_c and T_c has been observed in a coated conductor after neutron irradiation.

A tensile stress apparatus for assessing the dependence of J_c on tensile stress and strain in

coated conductors was developed in this work. Angular resolved measurements in magnetic fields up to 1.4 T were performed. The world's first tensile stress tests on coated conductors after neutron irradiation demonstrate the outstanding mechanical properties of coated conductors even after irradiation. Furthermore, a significant enhancement of the stress sensitivity of I_c after irradiation was found in the reversible region in one tape.

Promising perspectives for coated conductors and cables for fusion magnet applications can be deduced from our results, but a substantial further development of conductors and cables is needed to meet the requirements of future nuclear fusion plants.

Contents

A	Introduction	1
A.1	Expectations on HTS coated conductors for fusion magnets	3
A.2	Cuprates and coated conductors	7
A.3	Cable concepts	11
A.4	Neutron irradiation	12
B	Coupling losses in different geometries	15
B.1	Samples	15
B.1.1	Two strand Roebel loops	15
B.1.2	Striated tape	16
B.2	Experimental details and evaluation	18
B.2.1	Calibration free method (CFM)	18
B.2.2	Hall-scans in AC fields	19
	Set-up	19
	Evaluation of the local applied field	19
	Evaluation of the current distribution by inversion of Ampere’s law . .	20
	Evaluation of the magnetic moment and the AC loss	21
B.3	Calculation of the current distribution and the AC coupling losses	21
B.3.1	General	22
B.3.2	Low field regime (coupling current $I_{coupling} \ll I_c(0\text{ T})$)	23
B.3.3	High field regime (coupling current $I_{coupling} \geq I_c(0\text{ T})$)	32
B.4	Single Roebel strand characterisation	38
B.5	Results of the scanning measurements	40
B.5.1	Two-strand Roebel loop	40
	AC scans at 2 mT (low field regime)	41
	AC scans at 26 mT (penetration field regime)	45
	AC scans at 50 mT	49
	Frequency dependence	52
B.5.2	Striated single Roebel strand	53
B.6	Results of the AC loss measurements by calibration free method (CFM) . . .	54
B.6.1	Short sample	55

Contents

B.6.2	Intermediately long samples	56
B.6.3	Long sample	58
B.7	Prospects for coupled Roebel cables and conclusion	61
C	Homogeneity of Roebel single strands	64
C.1	Samples	64
C.2	Experimental details and evaluation	65
C.2.1	Magnetoscan measurements	65
C.2.2	Hall-scan measurements under current flow	66
C.3	Results and discussion	67
C.3.1	Homogeneity	67
IRL - 2 mm strand	67	
KIT - striated 5.5 mm strand	69	
C.3.2	Field distribution	71
C.3.3	Current distribution calculated from the field distribution	72
C.3.4	Local defects	74
C.4	Conclusion	76
D	Neutron irradiation	78
D.1	Samples	78
D.1.1	SuperPower SCS4050	79
D.1.2	SuperPower SCS 4050AP	81
D.1.3	AMSC 344C	81
D.1.4	AMSC 344S	82
D.2	Experimental details and evaluation	84
D.2.1	Irradiation facility	84
D.2.2	Transport and irreversibility line measurements in the 17 T-magnet	85
D.2.3	Anisotropy measurements in the 6 T-magnet	85
D.2.4	Tensile stress measurements	86
Set-up	86	
Measurement loop	92	
D.2.5	I_c -Evaluation	93
D.2.6	Irreversibility line and $T_{irr}(B)$ -evaluation	93
D.3	Results and discussion of transport measurements	94
D.3.1	Homogeneity of the tapes	94
D.3.2	Transport properties in the main field orientations at high fields (0 to 15 T)	94
Irreversibility line	97	
Critical current density J_c	100	

Contents

D.3.3	Anisotropy at intermediate fields (0 to 6 T)	105
	SuperPower SCS4050	107
	SuperPower SCS4050AP	107
	AMSC 344C	108
D.4	Results and discussion of tensile stress measurements	110
D.4.1	Stress-strain dependence	112
	SuperPower SCS4050	112
	AMSC 344C	113
D.4.2	Self-field critical current (I_c)	114
	SuperPower SCS4050	114
	AMSC 344C	115
D.4.3	Homogeneity	116
D.4.4	Anisotropy	118
	SuperPower SCS4050	118
	AMSC 344C	122
E	HTS for fusion magnet coils	126
	Bibliography	129
	Curriculum vitae	134

A Introduction

With the discovery of superconductivity in 1911 by Heike Kamerlingh Onnes, scientists and engineers started to dream of large superconducting magnets. It took many decades before the first superconducting magnet, cooled by liquid helium, was realised at the University of Illinois in 1954. This magnet reached nearly 1 T and was wound with cold worked Nb. In the following years one field record after another was broken with different niobium based materials. In subsequent years, most magnets were made of NbTi or Nb₃Sn and still work at liquid helium temperatures.

In 1986, Bednorz and Müller discovered superconductivity in Ba-La-Cu-O with a transition temperature of 35 K and a new class of superconductors (High Temperature Superconductors HTS) was born. Many copper-oxide compounds (cuprates) have been found to be superconducting. The highest transition temperature (164 K) was found in 1994 in HgBa₂Ca₂Cu₃O_{8+δ} under high pressure. Transition temperatures above liquid nitrogen temperatures (64-77 K) and high critical fields started a revival of the dream of high field superconducting magnets in the scientific community. It was only a matter of time until technical problems of manufacturing and handling of the brittle HTS materials could be solved. While the origin of HTS is not yet understood, the manufacturing process for technical conductors made of (RE)BCO-compounds has become highly developed. So far, it appears that the coated conductor design has won the race for a technical conductor architecture in high fields. Note, that BSCCO (Bismuth-strontium-calcium-copper-oxide) tapes and wires are also promising materials for low field and low temperature applications. However, due to their high amount of silver (high neutron activation), their low stress resistance and their high sensitivity of the critical current to high magnetic fields, BSCCO conductors are less viable for fusion magnet applications. In recent years, (RE)BCO coated conductor manufacturing has improved and long length conductors (km range) as well as first HTS-coated conductor magnet systems have become available on the market. Nevertheless, the question of a successful magnet cable design made of coated conductors remains open.

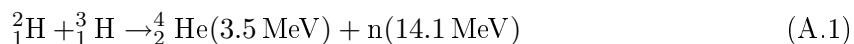
The International Thermonuclear Experimental Reactor (ITER) is currently being constructed in Caderache (France). About 30% of the reactor's overall costs arises from the superconducting magnet system. Fields up to 12 T are anticipated for the conductors of the coils. NbTi and Nb₃Sn at liquid helium temperatures will be used in the ITER coils.

The future availability of helium as a coolant is a major concern. HTS conductors can

A Introduction

use other coolants, such as nitrogen and hydrogen. The question of whether HTS conductors could be used for fusion coils has been under discussion for many years. In conceptual studies from 2006, the power consumption of cooling systems was calculated to be reduced by 21% if the magnets were cooled to 50 K and by 55% if liquid nitrogen temperature (77 K) was used [1]. Furthermore, a complex radiation shield could be avoided in such a system, reducing building costs. Other advantages of using HTS conductors are avoiding the complex Nb₃Sn “wind & react-technique” and much more convenient cold tests when using liquid nitrogen. On the other hand, HTS conductors are currently more expensive than LTS conductors and as yet there exists no suitable solution for the cable design. Nevertheless, there are promising solutions for the cable design and a large part of this work (Chapter B and C) outlines one possible solution, the Roebel cable concept.

During the ultimate research phase of ITER and in future fusion power plants, the deuterium (²H)-tritium (³H) reaction (DT-reaction) will be used as the fusion processes:



Under operating conditions, the α -particle (⁴He) with its kinetic energy of 3.5 MeV will heat the plasma, whereas the fast neutron with a kinetic energy of 14.1 MeV will breed new tritium from lithium in the blanket. Furthermore, the neutron should transfer its kinetic energy to usable heat for the energy production.

By passing the blankets, neutrons will slow down before they reach the magnet coils. The energy spectrum of the neutrons at the superconducting magnets was calculated for the STARFIRE fusion plant [2] and is shown in figure A.7. Although the neutrons are slower than immediately after the DT-reaction in the plasma, they have a strong contribution in the fast region ($E > 0.1$ MeV) and a destructive interaction with the coil material is expected. The durability of HTS conductors due to fast neutron irradiation has been demonstrated for YBCO coated conductors in recent years [3]-[5], but has become again a hot topic with new state-of-the-art conductors, as will be shown in Chapter D.

The next step from ITER towards a working commercial fusion plant is the construction of a demonstration reactor (DEMO). DEMO has four main goals [6]:

- To demonstrate a workable solution for all physics and technology questions.
- To demonstrate large scale net electricity production with a self-sufficient fuel supply.
- To demonstrate high availability and reliable operation over a reasonable time span.
- To access the economic prospects of a power plant.

A Introduction

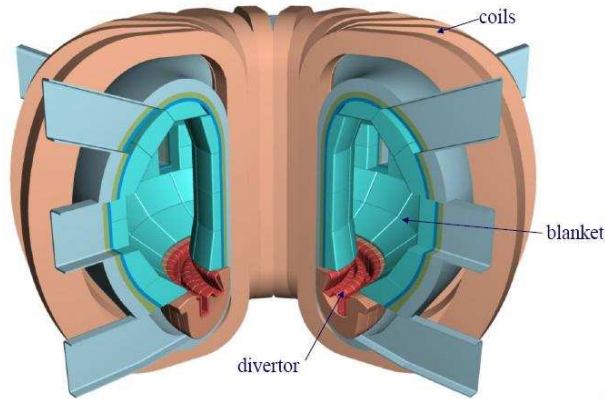


Figure A.1: Basic concept of DEMO.

Therefore, the fusion power of DEMO should be in the range of 2 - 5 GW (compared to 500 MW in ITER). Figure A.1 shows an image of a conceptual study for a DEMO design.

The first steps towards a working HTS solution for the DEMO magnet system have been achieved by many groups world wide. Nevertheless, a challenging path still awaits.

A.1 Expectations on HTS coated conductors for fusion magnets

Requirements on the HTS coated conductor in a fusion magnet are:

- High critical currents in high magnetic fields at high temperatures.
- The conductor has to withstand neutron irradiation without a performance loss.
- Homogeneity over long lengths of conductors and low resistive splicing.
- Current sharing between strands, but low AC losses.
- Mechanical strength and a low stress dependence of I_c .
- Cables with a large heat removal capability.
- Easy to handle cables (preferable round).
- Materials should be inexpensive.

A few of these points can already be realised with coated conductors and some are still to be resolved. In the following analysis, these expectations will be quantified. However, before detailed information can be given, three basic parameters ($J_c, J_E, J_{c,E}$) have to be defined, even if they may be trivial for most readers.

A Introduction

The critical current of a technical superconductor is reached if a critical field E_c (mostly $1 \mu\text{V}/\text{cm}$) is detected on the superconductor. Accordingly, the critical current density:

$$J_c = \frac{I_c}{A_{sc}} \quad (\text{A.2})$$

is the critical current divided by the superconducting cross section A_{sc} . Sometimes the critical current per tape width, also known as sheet current density, is used for coated conductors. Since the thickness of the superconducting layer is about two orders of magnitude lower than the width, it makes sense to assume a two dimensional architecture, where only a sheet current density:

$$J_c^{(2D)} = \frac{I_c}{w_{sc}} \quad (\text{A.3})$$

is needed. Here w_{sc} is the width of the superconductor.

The enhancement of J_c in a superconducting material is a major subject in material science. For an engineer or a coil designer, who wants to achieve a certain field with the winding, the engineering current density:

$$J_E = \frac{I}{A_{cond}} \quad (\text{A.4})$$

is the more important value. Here, A_{cond} is the cross section of the entire conductor or cable. In order to link the critical current to the cross section of the wound conductor we define a critical engineering current density:

$$J_{c,E} = \frac{I_c}{A_{cond}} \quad (\text{A.5})$$

Hence, an enhancement of $J_{c,E}$ is important for future fusion coils.

The highest fields (B_{max}) and currents occur in the toroidal field coils (TF), denoted simply as coils in Figure A.1. Therefore, the following investigations concentrate on these coils. For the magnetic field close to the conductor, the magnetic field in the plasma (B_t), the major radius of the Tokamak (R_p) and the plasma radius (a_p) are important. The maximum field at the conductor can be estimated by [7]:

$$B_{max} = \frac{\kappa B_t}{1 - \frac{a_p}{R_p} - \frac{\Delta_{int}}{R_p}} \quad (\text{A.6})$$

where Δ_{int} is the distance between the internal plasma edge and the superconducting winding and κ is an amplifying factor from the average field to take into account the sides of the casing. Typical values in [7] were $\kappa = 1.03$ and $\Delta_{int} = 1.9 \text{ m}$.

The current in ITER TF coils is 68 kA at 11.8 T and the corresponding engineering cur-

A Introduction

rent density for the CICC¹-conductor is $\approx 0.52 \cdot 10^8 \text{ Am}^{-2}$. Note, that there is already space for the coolant and copper in the underlying cross section. In a DEMO TF-coil, J_E could be a little bit smaller $\approx 0.42 \cdot 10^8 \text{ Am}^{-2}$ at a higher field of $B_{max} \approx 14.4 \text{ T}$ [7]. For a safe operation, J_c of the cable should be about three times higher than the current density during operation. Therefore, one can estimate for the critical engineering current density in a cable with space for the coolant:

$$\boxed{J_{c,E}^{Demo}(15 \text{ T}) \approx 1.2 \cdot 10^8 \text{ Am}^{-2}}$$

The most favourable alternative to cooling with liquid He is to use liquid nitrogen. The temperature range of liquid nitrogen ranges from the boiling point of 77.36 K (1 atm = 101.326 kPa) to the solidification point of 63.15 K (0.124 atm = 12.52 kPa) [8]. Therefore, a minimum operating temperature is defined as:

$$\boxed{T_{min} = 64 \text{ K}}$$

Note, that there also exist scenarios with less challenging requirements for HTS conductors in the community. In these concepts helium gas cooling, liquid hydrogen cooling (20 K) or liquid helium cooling (4.2 K) is used.

At the highest magnetic field, one would always need at least $J_{c,E}^{Demo}$.

As mentioned previously, neutrons from the DT-reaction escape to the magnet coils and arrive at the conductor with a wide energy spectrum. The fast neutron fluence over the whole lifespan t_{ls} of ITER was calculated to be:

$$\boxed{\Phi \cdot t_{ls}(E > 0.1 \text{ MeV}) = 10^{22} \text{ m}^{-2}}$$

where Φ is the neutron flux density. Note that all fluences in this work refer to fast neutrons ($E > 0.1 \text{ MeV}$). A wide spectrum of defects arise due to neutron irradiation. Point defects and point clusters lower T_c and therefore J_c . On the other hand extended defects – so-called collision cascades – are produced by fast neutrons and increase J_c as they are effective pinning centres. At high temperatures, both effects compete with each other and with increasing fluence the T_c reduction becomes more dominant. Starting with $J_{c,0}$ in a pristine conductor, J_c increases with increasing neutron fluence ($\Phi \cdot t$) until a maximum is reached at $\Phi \cdot t_{max}$. Afterwards, J_c decreases with increasing fluence reaching the initial value $J_{c,0}$ at a certain fluence. For higher fluences J_c decreases further.

At all times during operation J_c has to be higher than $J_{c,0}$ in the conductor. Therefore, the highest operating temperature could be used if J_c is equal to the initial value $J_{c,0}$ by the end of the reactor's lifespan.

¹Cable in Conduit Conductor

A Introduction

$$\boxed{J_c(B, T, \Phi \cdot t_{ls}) = J_c(B, T, 0)}$$

Currently two to three manufacturing lines exist worldwide which are able to produce homogeneous conductors of more than one km in one piece. The total conductor length of a DEMO fusion coil was estimated to be in the range of approximately 300 000 km depending on field, radius, etc. Therefore, cable splicings with as low as possible resistive joints are needed. Splicing Roebel-Rutherford or coaxial cables seems to be possible, but has not yet been demonstrated. Low resistive joints of single tapes have been investigated for various samples. Joint resistivities of about $2 \cdot 10^{-12} \Omega \text{m}^2$ have been reached with AMSC coated conductors.

Local inhomogeneities reduce I_c . As a consequence, thermal hotspots occur at the position of the impurities during operation. The smaller the conductor, the higher are the requirements on its homogeneity. Currents cannot bypass defects. If the conductor reaches the size of the defects. Nevertheless, if hotspots occur in a conductor, the current flowing in this conductor should be transferred to another one. Hence, resistive connections between single conductors are needed. But these connections form closed loops in the cable and therefore introduce AC losses. One has to optimise future cables with respect to these two effects and therefore a detailed knowledge of AC loss phenomena is important.

At high magnetic fields and high currents, significant forces act on the magnets. These forces can affect the superconductor in two different ways. Firstly they could damage the conductor irreversibly and, secondly, the critical currents could decrease with increasing tensile stress even if they are in the reversible region. Therefore, the irreversible stress limit σ_{irr} should be as high as possible and the sensitivity of the critical current ($I_c(\sigma_{irr})$) on stress as low as possible. Since the irreversible limit in NbTi and Nb₃Sn would be too low in ITER ($\sigma_{irr} \approx 100 - 200 \text{ MPa}$, $\varepsilon_{irr} \approx 0.4\%$ for a typical Nb₃Sn/Bronze wire), the conductors have to be wound under compressive stress. In other words, some pre-stress/strain is applied under normal conditions. Furthermore, the CICC cables have to be mechanically stabilised by radial plates in order to reduce the stress/strain on the superconductor. In fact, about 55% of the cross-section material of the TF coils is 316LN structural steel. According to [9], the centering force, vertical force and hoop stress maximum values of the TF coils are 403 MN, 205 MN and 470 MPa, respectively. In DEMO, the currents of the TF-coils are lower than in ITER, but the field is higher. The forces acting on the superconductor will approximately be similar in DEMO since $F \propto J \cdot B$. Therefore, we assume a minimum criterion for the tensile stress for coated conductors, without pre-compression of

$$\boxed{\sigma_{irr, min} = 500 \text{ MPa}}$$

A Introduction

in this study. Note that the joints between the cables/strands also have to withstand these stresses without a significant critical current reduction. Hence, tensile stress measurements of different splicing techniques have to be performed in future cables as well.

The superconducting coil has to handle quenches (transitions to the normal conducting phase) during operation. Hence, a certain amount of copper is necessary in order to limit the hotspot temperature to a critical value (e.g. 150 K). If the temperature of the hotspot stays below this critical temperature, the cable should be able to recover without damage. The amount of copper has to be optimised for different cable designs. In the ITER Nb₃Sn strands, the copper/superconductor ratio is 1.3 [10]. In copper-stabilised coated conductors the ratio copper/superconductor is typically 40.

The production costs of (RE)BCO coated conductors mainly depend on the expensive vacuum deposition technique. Therefore, the cost per kAm is high in comparison to Nb₃Sn (15 \$/kAm). Currently, the price for a SuperPower tape is about 175 \$/kAm. In recent presentations SuperPower Inc. predicted to reach a price of 30 \$/kAm within the next 4 years [11]. This rather optimistic price could be reached by increasing the superconducting layer thickness. Other experts suggest a low-end limit of 50 \$/kAm, which cannot be further reduced due to the expensive vacuum deposition technique. Note, as previously mentioned, the easier assembly technique of HTS cables could also lower the overall costs.

A genuine cost cut could be expected with “All chemical deposition techniques” (Chemical Solution Deposition, CSD). Such techniques exist, but do not as yet reach the performance of vacuum deposition techniques. Nevertheless, considerable efforts are being made (e.g. in the EUROTAPES-Project) to improve such low-cost manufacturing techniques.

A.2 Cuprates and coated conductors

Coated Conductors, often referred to as second generation (2G) wires², are based on (RE)Ba₂Cu₃O_{7- δ} (REBCO or RE123) cuprates. RE denotes rare earth materials, such as Y, Gd, Sm, etc. At the beginning of coated conductor development, most of the materials used were Y-based. Figure A.2 shows the structure of the YBCO compound. The Cooper-pairs, which carry the charge, are formed within the copper-oxide (CuO₂) planes. Therefore, one can speak of strong superconducting layers with weak superconducting planes in between. In these weak superconducting planes, the order parameter is reduced. The layered structure causes strong anisotropy effects. Let us consider an applied field parallel to the CuO₂ planes (a,b-planes), as illustrated in Figure A.3(a). Since HTS are type II superconductors,

²first generation (1G) wires refer to BSCCO-2212 (Bi₂Sr₂Ca₁Cu₂O₈) or BSCCO-2223 (Bi₂Sr₂Ca₂Cu₃O₁₀) tapes

A Introduction

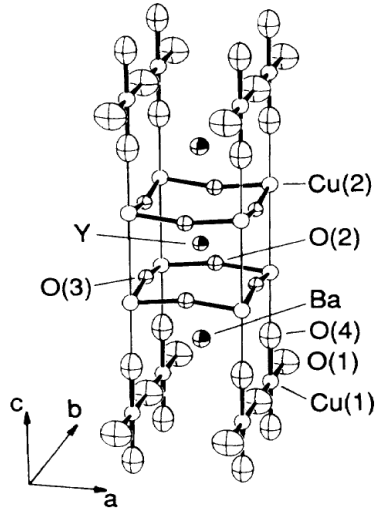


Figure A.2: Crystal structure of YBCO. The a,b-plane is parallel to the CuO_2 planes, whereas the c-axis is perpendicular to the CuO_2 planes. [12]

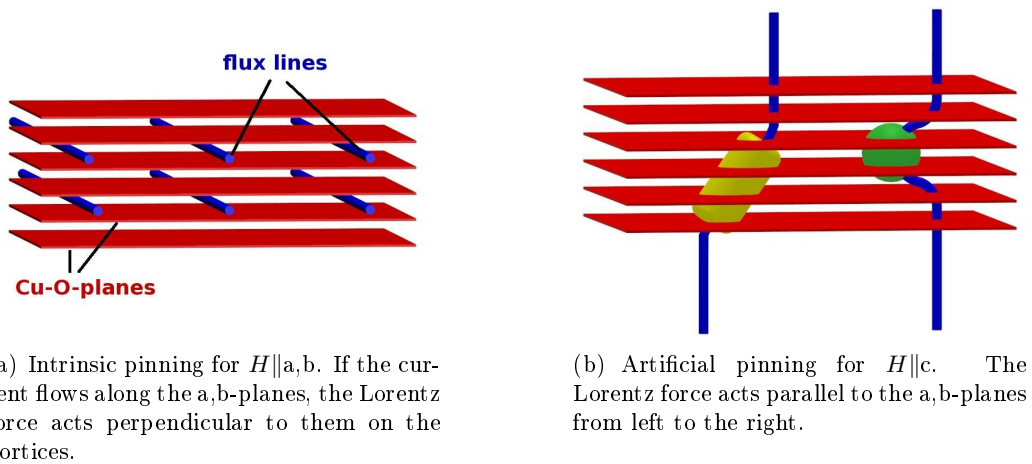


Figure A.3: Schematic illustration of intrinsic and artificial pinning in cuprates.

A Introduction

flux lines – or vortices – penetrate into the material. The magnetic flux inside each vortex is exactly the flux quantum $\Phi_0 = h/(2e)$. Furthermore, the core of these flux lines is in the normal conducting phase. The vortices are pinned in between the superconducting CuO_2 layers since the superconductor does not have to spend the whole condensation energy of the flux line on the core volume, if the order parameter is already suppressed between the CuO_2 layers. This energy gain is caused by a pinning force and the whole effect is called intrinsic pinning. As long as the Lorentz force ($I \times B$) is smaller than the pinning force, currents can flow in the superconductor without losses. When the Lorentz force becomes equivalent to the pinning force, the critical current I_c is reached.

One can imagine that the situation drastically changes if the applied field is parallel to the c-axis of the crystal. The flux lines can only be pinned at grain boundaries or impurities and therefore smaller critical currents can flow. Scientists try to increase the pinning force in such an arrangement by introducing normal conducting impurities – so-called artificial pinning centres (APCs) – with dimensions close to the superconducting coherence length ξ (a few nm). Vortices will be pinned by these normal conducting impurities. Figure A.3(b) illustrates such situations for two different kinds of defects. Neutron irradiation is an effective way to introduce defects, but not applicable for a long-length conductor production. REO_2 particles are often used to create point defects in MOD (Metal-Organic Deposition) conductors [13]. In MOCVD (Metal-Organic Chemical Vapour Deposition) coated conductors BaZrO_3 grows in the form of correlated nano-columns during the vapour deposition process [14]. Note that columnar defects can be oriented in different angles, leading to favourable field directions beside $H \parallel a, b$ at low fields.

Manufacturers try to optimise their tapes not only by introducing different nano-defects, but also by trying different rare earth elements in (RE)BCO, in some cases two or more, but all 2G wires have more or less similar architecture. However, the manufacturing process and the resulting characteristics differ greatly.

In recent years, two main concepts became successful and both need to provide a bi-axially textured basis for the superconductor epitaxial growth. It is incredibly important that the grains are well-aligned in the a,b-plane, as a misalignment between the grain boundaries will lead to a significant reduction of the critical current [15][16].

One manufacturing process uses Ni-W alloys as a substrate and textures the substrate mechanically by cold work. The so called RABiTSTM (Rolling- Assisted Biaxially-Textured Substrates) technology, used by AMSC, is a widely used synonym for this process. The buffer layer between substrate and superconductor acts as a diffusion barrier and adjusts the lattice parameters between the layers.

The second route uses metal alloys, such as Hastelloy ®, or stainless steel, as a substrate.

A Introduction

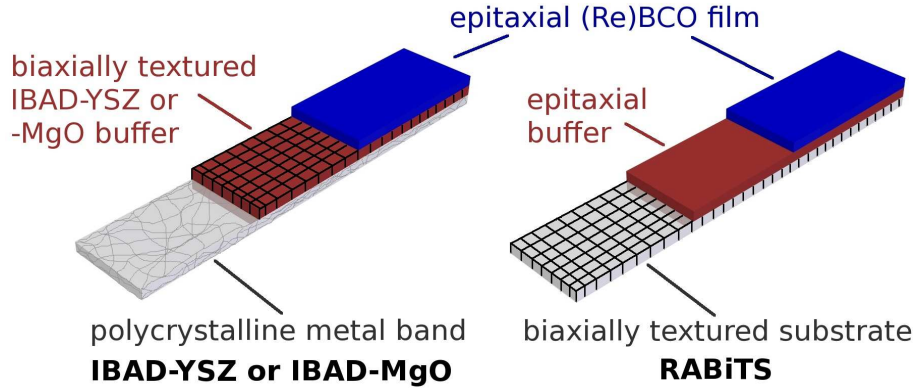


Figure A.4: The two main routes for coated conductor manufacturing.

Contrary to the first process, the surface of the substrate is untextured and therefore the buffer layers deposited on the substrate have to be textured to align the superconductor during the growth process. The IBAD (Ion Beamed Assisted Deposition) technique is, for instance, a method to texture the buffer layer. Figure A.4 shows the two concepts.

The typical thickness of the substrate is between $50\ \mu\text{m}$ and $100\ \mu\text{m}$, of the buffer a few $100\ \text{nm}$ and the superconducting layer is about $1\ \mu\text{m}$ thick. The critical current density decreases in thicker (RE)BCO layers, as J_c drops in the upper regions of the film. However, the engineering current density J_E could be increased with thicker superconducting layers even if the critical current density of the superconductor J_c becomes smaller. Note, that it is currently a major concern of company scientists to increase the superconducting film thickness. Lastly, a thin silver layer ($\approx 2\ \mu\text{m}$) protects the (RE)BCO-film on the top, which allows a better current and heat distribution and stabilises the superconducting layer chemically and thermally. Most of the manufacturers additionally surround or laminate the conductor with copper for electrical stability and better handling.

Usually companies do not provide their customers with detailed information about the superconducting layer. In reality, they change compositions without changing the name of the product which makes scientific work more difficult. In the case of the SuperPower samples (see Chapter D) an YBCO layer was anticipated. Different behaviours were found in these samples, especially after irradiation when compared with older samples. After discussing our results with the company we finally received details of the the correct composition, which was GdBCO and not YBCO.

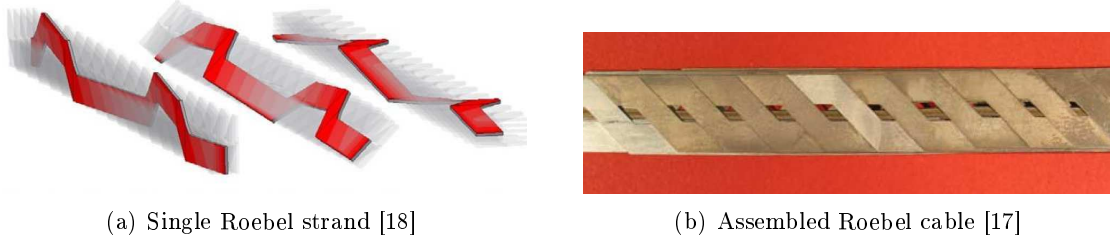


Figure A.5: The Roebel cable concept

A.3 Cable concepts

(RE)BCO-coated conductors are the most promising HTS-wires for future fusion magnet coils. Cables with low AC losses and high current capabilities are needed to wind these coils. Due to the coated conductor geometry, it is not possible to twist the individual filaments, as in the CICC-cables for ITER. One of the most promising solutions to this problem is the Roebel assembled coated conductor concept (RACC or just Roebel cable). The idea of winding Roebel cables from coated conductors was first presented by Wilson 1999 and re-established by the Karlsruhe Institute of Technology in 2006 [17]. A Roebel cable consists of single meander shaped Roebel strands punched out of a coated conductor. These single strands, once wound together produce a fully transposed cable. Figure A.5(a) illustrates one single strand wound into a cable and Figure A.5(b) shows an assembled Roebel cable.

The degradation of the current carrying capabilities due to self-generated magnetic fields is approximately 60 % in the Roebel cable.

Much work has been undertaken with Roebel cables in recent years. The feasibility of producing long length Roebel cables has been demonstrated [19], a further reduction of the AC losses has been obtained by striation of Roebel strands [20] and new concepts of winding Roebel cables to Rutherford cables (Roebel-Rutherford cable) have been presented [21].

The cable with the highest I_c reached 2628A ($5 \mu\text{V}/\text{cm}$ criterion) at liquid nitrogen temperature in self-field. The critical engineering current density of the cable was $9.53 \cdot 10^7 \text{ A}/\text{m}^2$.

By decreasing the strand width, the homogeneity of the coated conductor begins to play a crucial role. The strand width reduction, due to punching or striation, reduces the possibility of currents bypassing defects.

A further promising cabling technique is the coaxial cable. IEE Bratislava demonstrated the ability of a coaxial cable, wound on a brass former, to carry currents up to 900 A [22]. Furthermore, they investigated the losses of different cabling methods [23]. Spiral wound GdBCO-coated conductors on a flexible round cooper wire (Conductor on Round Core Cable CORCC) [24] were recently presented with the round cooper wire acting as a former for mechanical stability. A future coil cable could use the space of the cooper wire as a cool-

A Introduction

ing channel. A two-phase cable with an outer diameter of 10 mm reached an I_c of 7561 A ($J_E = 9.6 \cdot 10^7 \text{ Am}^{-2}$) [25]. Similarly wound cables with an I_c of 1232A were bent down to a bending radius of 12.5 cm without any reduction of I_c , which demonstrates the strong durability of this cable. Stress and strain dependence are crucial for this kind of cable. For instance, cable wound from an YBCO instead of GdBCO-coated conductor would lead to a higher reduction of I_c due to a stronger dependence of I_c on compressive strain [26]. Figure A.6(a) shows the cross section of a spiral wound cable.

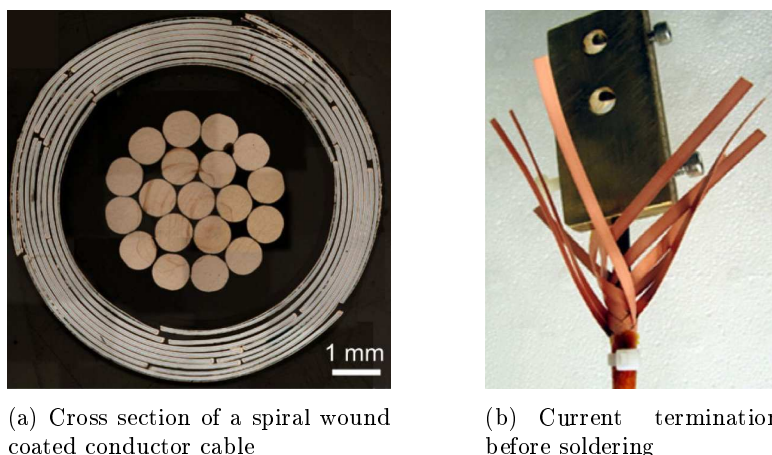


Figure A.6: Images of a four layer CORCC cable taken from [24].

The advantage of such a cable is the good scalability, since there is less degradation of the whole cable I_c compared to the sum of each strand I_c . Furthermore, the assembling technique is less complex than that of a Roebel cable. One disadvantage, however, is the alignment of the conductor surface in the non favourable field direction and, since the cable is arranged in layers, a complete transposition of the tapes is not possible. Early in 2012s CORCC cables became commercially available at Advanced Conductor Technologies LLC [27].

A.4 Neutron irradiation

As previously mentioned, a neutron escapes from the plasma during the DT-fusion reaction. Most of its energy is deposited in the blanket (“first wall”) where the heat is removed by a heat exchanger and used to drive a turbine. Due to the absence of electric charge, some neutrons will pass the blanket as well as the radiation shield and will therefore reach the magnet coils. From geometric considerations, it is obvious that the highest fluence will occur in the central areas of the inner legs of the TF coils. The neutron spectrum at the coils location was calculated for the STARFIRE fusion plant in [2] and is shown in figure A.7. As one can see, the neutron spectrum of the TRIGA MARK II reactor in Vienna is similar to

A Introduction

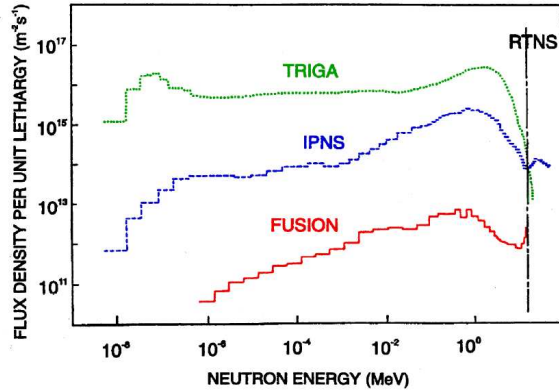


Figure A.7: Neutron spectrum at the magnet location. The red curve refers to the neutron flux density distribution calculated for the STARFIRE fusion reactor design. The other curves labeled TRIGA, IPNS and RTNS refer to irradiation facilities used for irradiation studies of the magnet components. Figure taken from [28].

the fusion spectrum at high energies. Due to the higher flux density in a fission reactor by a factor of $\approx 10^4$, the expected lifetime-fluence can be applied in a rather short time. The TRIGA reactor in Vienna has therefore demonstrated its suitability for simulating neutron radiation effects at the magnet location in a future fusion reactor.

The damage in the material caused by the neutrons depends on the starting material. Fast neutrons ($E > 0.1$ MeV) cause collision cascades by transferring sufficient energy to a primary knock-on atom, which generates further collisions in cuprates [29][30]. This leads to local melting of the lattice and spherical defects with a diameter of ≈ 6 nm. The size of these normal conducting impurities is close to the size of a flux line core ($2\xi_{a,b} \approx 4$ nm at 77 K) and therefore to the dimensions of an optimal pinning centre. These defects are uncorrelated and randomly distributed. Fast-neutron-induced cascades have been shown to be responsible for flux pinning and intrinsic critical current enhancement in (RE)BCO [31][29].

For YBCO, it was shown that thermal and epi-thermal neutrons do not generally lead to extended defects. Epi-thermal neutrons (keV range) may create point defects or clusters, if the recoil energy of the excited atom is only high enough to displace the atom. These point defects disturb the regularity of the CuO_2 planes, which reduces the critical temperature and lowers the intrinsic peak. In YBCO, the reduction in T_c is rather weak (2 K for $\Phi \cdot t = 10^{22} \text{ m}^{-2}$ [5]). Thermal neutrons ($E < 0.5$ eV) will not affect the material, as their transferred energy due to collisions is below the displacement energy of a single atom.

Nuclei with very high neutron capture cross-sections for thermal and epi-thermal neutrons should be avoided in coated conductor materials. Unfortunately, new (RE)BCO coated conductors, containing gadolinium (GdBCO) and samarium (SmBCO), have very high neutron capture cross-sections. After neutron capture, the excited nucleus emits γ -rays and a recoil

A Introduction

energy acts on the nucleus. If this recoil energy is sufficiently high, as in the transmuted ^{156}Gd daughter of the ^{155}Gd nucleus (29 eV [31]), a point defect is created. Hence, in Gd or Sm-compounds the thermal and epi-thermal part of the TRIGA reactor neutron spectrum, which deviates from the fusion spectrum, could play a crucial role.

In Chapter D, results on irradiated GdBCO and Y-GdBCO tapes from SuperPower in the TRIGA reactor are presented. They show a significant performance loss.

As already mentioned, the supplier of the samples did not inform us, about changing their manufacturing process and the substitution of yttrium by gadolinium in their tapes. Therefore, the samples were irradiated with the whole neutron spectrum. However, in future experiments thermal and epi-thermal neutrons could be shielded by a gadolinium-foil around the sample. The energy spectrum of the neutrons would then be closer to a fusion spectrum at the magnet location. Results of such irradiation studies will be compared with the present results and would provide important information about the physics of GdBCO coated conductors after neutron irradiation.

B Coupling losses in different geometries

In order to understand coupling mechanisms in complex Roebel cables, single strands coupled in different geometries have been investigated in this work. Simplified analytical and semi-analytical models were developed for low and high AC fields that describe and predict the time and frequency dependent losses as well as the coupling currents caused by AC fields. AC loss measurements were performed by a calibration free method (CFM) and with AC Hall scans. Both measurements confirm the model calculations. Furthermore, an algorithm for calculating the current distributions and the time dependent losses from AC Hall maps was developed in this work and will be presented in the following.

The losses in the coupled samples showed a strong frequency dependency. Different coupling situations cause this frequency dependence and will therefore be discussed with respect to:

- Modelling
- AC Hall scan measurements (fields, current distributions and losses)
- Calibration free method loss measurements

Furthermore, a striated Roebel single strand was investigated in order to test if the single filaments are coupled to each other.

B.1 Samples

B.1.1 Two strand Roebel loops

The Roebel loops were assembled from two millimetre single Roebel strands. The original conductor of the strands is a SuperPower 2G-HTS-SCS12050 YBCO tape. This tape is coated with 20 μm copper stabilizer on both sides. The detailed architecture of this tape can be found in section D.1.1 on page 79. The Roebel shape of the strand was manufactured by Industrial Research Limited. The process is described elsewhere [19].

Seven samples were prepared. In order to distinguish between coupling and hysteresis losses we always prepared one insulated and at least one coupled sample of nearly the same geometry. Three insulated ($\text{Short}^{(I)}$, $\text{Intermediate}^{(I)}$ and $\text{Long}^{(I)}$) and four coupled samples ($\text{Short}^{(C)}$, $\text{Intermediate}^{(C)}$, $\text{Intermediate}^{(C-HR)}$, $\text{Long}^{(C)}$) were assembled.

Sample $\text{Intermediate}^{(C-HR)}$ was coupled with a higher resistivity than the others. Figure B.1 shows the geometry of the samples.

B Coupling losses in different geometries

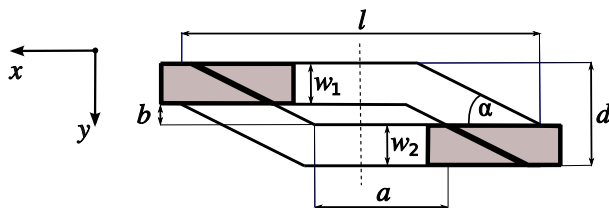


Figure B.1: Geometry of the coupled two-strand Roebel loop. The grey shaded area marks the region of the coupling between the two strands. The resistance of the upper left connection is denoted as R_1 whereas the lower right connection as R_2 . AC Hall scans were performed along the dashed line in y-direction.

The sample consists of two single Roebel strands each with one crossover part, which would generate a conducting loop if connected. The dimensions are crucial for the losses, because they are proportional to the area enclosed by the superconductor and therefore proportional to the induced electric field. The widths of the two single strands were not always equal. Hence, a mean value of $w = (w_1 + w_2)/2$ was used for all calculations. Using geometrical approaches, one finds:

$$l = a + 2w(\cot \alpha + \tan \alpha/2) + b \cot \alpha \quad (\text{B.1})$$

for the characteristic sample length, as indicated in figure B.1. Three different sizes of a were realized. $a \approx 6.5$ mm (short), $a \approx 14$ mm (intermediately long) and $a \approx 35$ mm (long). The angle α of the crossover part was 30° for all samples. Three low resistive coupled samples (short, intermediate and long length) were connected with soldered copper bridges marked by the grey shaded area in figure B.1. The resistance between the single strands $R_{1,2}$ is about $7 \mu\Omega$ in the presence of the copper bridge. Typical dimensions of the copper bridges were $0.1 \text{ mm} \times 2 \text{ mm} \times 8 \text{ mm}$. The high resistive sample (intermediate length) was soldered without a copper bridge, resulting in a resistivity of about $20 \mu\Omega$ between the strands. An InAg-solder was used with a melting point of 143°C to solder the materials. The three insulated samples (short, intermediate and long length) had nearly the same dimensions as the coupled ones, but an insulating Teflon sheet was sandwiched between the two strands.

Tables B.1, B.2 and B.3 show the details of each sample.

B.1.2 Striated tape

A further approach for reducing AC losses in Roebel cables was presented by the Karlsruhe Institute of Technology in 2010 [20]. So called striated Roebel strands were manufactured by pico-second infra-red laser scribing of Roebel strands. Figure B.3 shows a typical sample. The Roebel strands were punched out of a 12 mm stabilizer free SuperPower coated conductor

B Coupling losses in different geometries

Name	a (mm)	b (mm)	w_1 (mm)	w_2 (mm)	l (mm)
Short ^(C)	6.05	1.05	2.05	1.95	17.0
Short ^(I)	6.3	0.95	1.85	2.05	17.2
Intermediate ^(C)	13.85	0.85	2.0	1.80	23.1
Intermediate ^(C-HR)	14.05	1.10	1.95	1.8	24.1
Intermediate ^(I)	14.05	0.90	2.15	1.95	25.1
Long ^(C)	33.2	1.30	2.00	2.20	44.25
Long ^(I)	34.3	0.85	2.00	2.10	45.25

Table B.1: Geometrical details of the samples

Name	R_1 ($\mu\Omega$)	R_2 ($\mu\Omega$)	I_{c1} (A)	I_{c2} (A)	n_1	n_2
Short ^(C)	7.0	7.0	38.9	38.8	26.7	29.6
Short ^(I)	-	-	38.8	38.6	24.5	26.3
Intermediate ^(C)	6.6	7.9	40.2	40.3	28.8	35.2
Intermediate ^(C-HR)	17.4	20.4	38.0	38.5	23.4	22.1
Intermediate ^(I)	-	-	39.8	41.0	25.5	23.2
Long ^(C)	5.9	9.1	38.1	38.3	26.0	26.4
Long ^(I)	-	-	38.5	37.5	23.7	23.7

Table B.2: Electrical characterisation of the samples at liquid nitrogen temperature ($T = 77$ K)

Name	L_{meas} (nH)	L_{lf} (nH)	L_{hf} (nH)	$f_{c,lf}$ (Hz)
Short ^(C)	12.4	6.67	9.08	334
Intermediate ^(C)	14.0	10.9	15.1	212
Intermediate ^(C-HR)	16.0	12.0	16.1	502
Long ^(C)	29.2	25.2	33.6	94.6

Table B.3: Inductances of the coupled samples. L_{meas} was measured with a standard RLC-meter before joining the second bridge. L_{lf} , L_{hf} and $f_{c,lf}$ were calculated from (B.28), (B.38) and (B.36), respectively.

B Coupling losses in different geometries

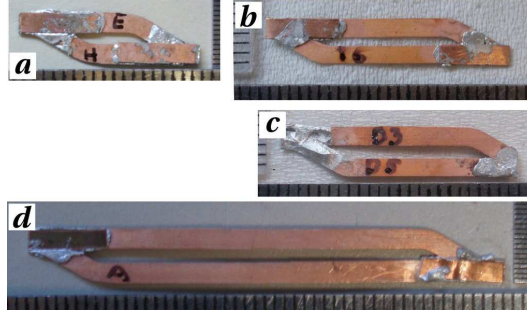


Figure B.2: Photographs of the coupled samples. (a) Short^(C); (b) Intermediate^(C); (c) Intermediate^(C-HR); (d) Long^(C)

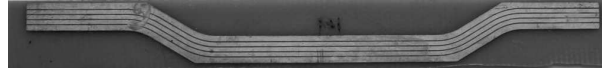


Figure B.3: Striated Roebel strand from KIT

(SF12050). The distance between two filaments was found to be $\approx 25 \mu\text{m}$ and the reduction of I_c due to the grooving was less than 10% [20].

Figure C.9 on page 70 shows the separation of the superconducting layer into single filaments obtained by the magnetoscan technique.

B.2 Experimental details and evaluation

B.2.1 Calibration free method (CFM)

Magnetic AC loss measurements of the Roebel loops were carried out during a research stay at IRL (NZ) using a calibration-free electromagnetic technique. This calibration-free method for measuring magnetic AC losses was originally developed by Šouc from IEE Bratislava [32]. A detailed description of the set-up used at IRL can be found elsewhere [33]. All measurements were taken with the samples immersed in liquid nitrogen at a stable temperature of about 77 K. The applied AC field was always parallel to the c-axis of the superconductor.

The loss measurements always included background measurements without a sample in the sample coil. Especially for the small and uncoupled samples, the background signal was sometimes of the same order of magnitude or even higher than the signal from the sample. Hence, the background signal was measured a few times and a mean value was used.

B.2.2 Hall-scans in AC fields

Set-up

Hall scans in AC fields were performed with an AC Hall scan set-up, originally developed by E. Pardo, at the Atominstitut in Vienna. Figure B.4 shows a sketch of the set-up. A

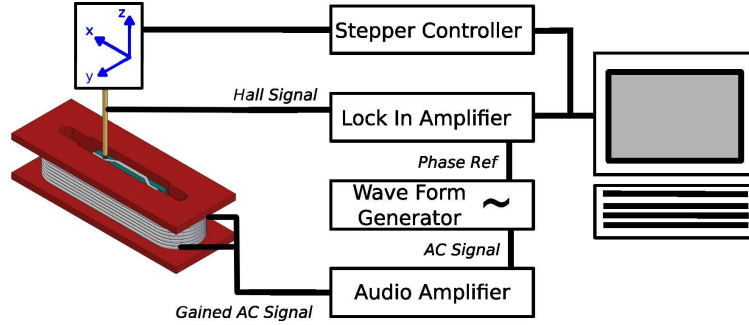


Figure B.4: AC Hall scan set-up

sinusoidal AC signal is generated by a standard wave form generator. The signal amplified by an audio-amplifier drives a normal conducting race track coil with a rectangular inner bore of 15×1 cm. The sample is then placed inside the coil and everything is immersed in liquid nitrogen, ensuring a sample temperature of about 77 K during the measurement.

A cryogenic Hall probe measures the local field ($B_{z,signal}$) perpendicular to the sample. The Hall probe is moved by a stepper motor slightly above ($\approx 100 \mu\text{m}$) the sample. The Hall voltage is detected by a lock-in-amplifier using the wave form generator's TTL output signal as a reference. Fourier components up to the 9th harmonic are measured and allow a time dependent resolution of the field at each position. For all AC Hall scan measurements in this chapter, the Hall probe was only moved in the y-direction (see figure B.4 for the coordinate system) above the sample. The spatial resolution was $100 \mu\text{m}$. The centre of the sample with respect to the x-axis was positioned below the Hall probe. The effective area of the Hall probe was about $100 \mu\text{m}$.

Evaluation of the local applied field

In order to find the accurate self-field of the sample at the positions of the Hall mapping, it was important to determine the local applied field ($\mu_0 H(y, t)$), precisely. The generated field was therefore measured without a sample at different fields. The local field along the x-position was approximated by a fit to the measured data:

$$\mu_0 H(y, t) = \mu_0 H_0 \sin(\omega t) (1 + 474.8 y^2) \quad (\text{B.2})$$

B Coupling losses in different geometries

Using (B.2), the local and time dependent applied field was entirely determined by H_0 .

Under normal conditions, H_0 has to be evaluated from the measured data when the sample is inside the coil. A first approximation of H_0 is achieved by choosing H_0 in a way that subtracting it from the measured field pattern would give zero at the outer edges. In a second step, H_0 is varied as long as the net current calculated by the inversion of Ampere's law is zero. Since no current sources exist in the bore of the magnet, this condition has to be constantly fulfilled and therefore presents a strong constraint.

Thus, at a certain time, the local self-field $B_z(y, t)$ is obtained by subtracting the calculated applied field $\mu_0 H(y, t)$ from the measured field $B_{z,signal}(y)$.

An accurate determination of the applied field is crucial for the inversion and loss evaluation from the raw data.

Evaluation of the current distribution by inversion of Ampere's law

The field above a one dimensional current distribution is obtained by Ampere's Law for infinitely long samples:

$$B_z(y') = \frac{\mu_0}{2\pi} \int \frac{y' - y}{(y' - y)^2 + (z' - z)^2} J^{(2D)}(y) dy \quad (\text{B.3})$$

where $J^{(2D)}(y)$ is the local sheet current density. For discrete currents with $m_{max} = l_{max}$ single wires, where l_{max} is the number of measured fields and l, m are integers $1 \leq l, m \leq l_{max} = m_{max}$, one can rewrite (B.3):

$$B_l = \frac{\mu_0}{2\pi} \sum_{m=1}^{m_{max}} \frac{y_l - y_m}{(y_l - y_m)^2 + (z_l - z_m)^2} \cdot I_m = F_{lm} \cdot I_m \quad (\text{B.4})$$

If one further assumes that the sample is slightly tilted to the scanning plane with an angle φ , one finds for F_{lm} :

$$F_{lm} = \frac{\mu_0}{2\pi} \Delta y \frac{l - (m - \frac{1}{2}) \cos \varphi}{(l - (m - \frac{1}{2}) \cos \varphi)^2 \Delta y^2 + ((m - \frac{1}{2}) \sin \varphi \Delta y + z_0)^2} \quad (\text{B.5})$$

if the grid for the current of the non tilted sample is shifted by $\Delta y/2$ with respect to the measured field points. The distance between the highest point of the sample and the scanning plane is z_0 . Figure B.5 illustrates the geometrical approach.

F_{lm} can be easily calculated by numerical methods for this problem. Using a common linear equation solver, I_m can be calculated within milliseconds on a standard PC. In this work, the standard linear equation solver (scipy.solve) from the scientific python package [34] was used.

A corresponding current density for each wire was calculated by dividing the discrete current I_m with Δy and the thickness of the superconducting layer d_{sc} .

B Coupling losses in different geometries

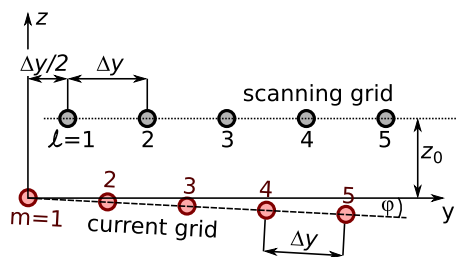


Figure B.5: Geometrical approach of the inversion of Ampere's law

Evaluation of the magnetic moment and the AC loss

The magnetic moment per unit length of an infinitely long structure is given by:

$$M^{1D} = \int_{-a}^a y J^{(2D)}(y) dy = \sum_m^m y_m I_m \quad (\text{B.6})$$

Once the magnetic moment per unit length is determined, the loss per cycle and unit length can be calculated from the hysteresis loop:

$$Q = \mu_0 \oint M^{1D} dH = \mu_0 \int M \frac{dH}{dt} dt = \mu_0 \sum_m^m y_m I_m \frac{dH_m}{dt} dt \quad (\text{B.7})$$

where the integral over the applied field dH is replaced by an integral over the time t . The applied field at each position m , as well as the derivative, at a certain time can be calculated from (B.2), since m is identical with a certain y -value.

B.3 Calculation of the current distribution and the AC coupling losses

The magnetic losses in a superconducting cable consist of:

$$Q = Q_{hyst} + Q_{coupl} + Q_{eddy} \quad (\text{B.8})$$

where Q_{hyst} is the hysteresis loss according to Brandt [35], Q_{coupl} is the coupling loss, if one has a closed loop, and Q_{eddy} is the eddy current loss mainly from the copper.

Hysteresis losses occur in all uncoupled superconductors due to the intrinsic shielding currents if a field is applied. If one connects superconducting tapes to a loop by resistive connections, additional coupling currents flow in AC fields over these connections resulting in the coupling losses. Coated conductors consist of many resistive components as substrates, silver layers or copper surroundings. In AC fields, eddy currents will also be induced in these

B Coupling losses in different geometries

non-superconducting materials. The losses corresponding to these currents are denoted as eddy current losses in this work.

In this section, the hysteresis losses will be neglected since they are well described in [35] and [36]. Nevertheless, in the following sections the coupling phenomena and their interplay with the hysteresis phenomena is a major concern. The eddy current losses will be neglected since they are mostly small when compared with the other losses. Only at high fields and high frequencies the eddy currents inside the copper bridges might disturb the currents caused by the hysteresis and coupling effects, as recently found in coupled parallel tapes [37]. However, no influence of eddy currents was found in the samples described in this work.

In the following text, currents that cause the hysteresis loss or in other words currents that flow in an uncoupled situation, are referred to as intrinsic shielding currents. Furthermore, intrinsic shielding currents flowing when no field is applied are referred to as trapped flux currents.

B.3.1 General

The induced voltage V_{ind} in a current loop of an infinitely thin wire is given by Faraday's law

$$V_{ind} = - \iint \dot{B} dA \quad (\text{B.9})$$

where B denotes the field inside the loop. In coated conductors, thin film behaviour has to be considered. Assumptions to describe this behaviour in our samples will be presented in the following sections. Figure B.6 shows the electric equivalent circuit diagram for our samples.

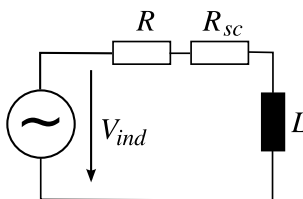


Figure B.6: Electric equivalent circuit diagram for a Roebel loop

R_{sc} and R respectively denote the resistivity of the superconductor due to the power law and the resistivity of the ohmic connections.

Substitution of R_{sc} by the power law $V/V_c = (I/I_c)^n$ gives for the First Kirchhoff Law:

$$I \frac{dL}{dt} + L \frac{dI}{dt} + RI(t) + V_c \frac{I(t)^{n(B)}}{I_c(B)^{n(B)}} - V_{ind} = 0 \quad (\text{B.10})$$

B Coupling losses in different geometries

where V_c is the critical voltage corresponding to a $1 \mu\text{V}/\text{cm}$ criterion, I_c is the critical current, n the exponent of the power law, L is the inductance of the loop and B is the time dependent local field. The inductance depends on the current distribution in the loop and therefore on the history of the local magnetic field, too.

For the two regimes (high field and low field regime) calculated in the following sections we found that the inductance can be assumed to be constant. Therefore, the first term in (B.10) becomes zero in all our calculations.

In order to find an equation for the field dependence of I_c and the n – *value*, the transport properties of a 2 mm wide single strand with $H \parallel c$ up to 8 T were measured. Details of this measurements and the final equations of $I_c(B)$ and $n(B)$ are listed in section B.4.

The field, where a single strand is fully penetrated, B_p , can be calculated from [38] to be $B_p = 1.569 \mu_0 J_c d/2$. The calculated penetration field B_p is about 20 mT for our single strands at 77 K.

For the modelling, the applied field is assumed to be homogeneous and sinusoidal:

$$H_a = H_0 \sin(\omega t) \tag{B.11}$$

B.3.2 Low field regime (coupling current $I_{\text{coupling}} \ll I_c(0 \text{ T})$)

At low fields, the hysteresis losses are very small, because they are proportional to B^4 [35], thus only an equation for coupling losses and the induced coupling currents will be derived in the following model. However, the intrinsic shielding currents that cause the hysteresis losses are considered, as they influence the coupling currents and therefore the losses.

At low applied fields, vortices cannot penetrate into the superconductor and the applied field is perfectly shielded. In uncoupled samples or at low frequencies, the currents flow as indicated in figure B.7a in the sample if a field $\vec{H}_a = H_a \vec{e}_z$ is applied. Note that the currents are distributed over the whole width in a thin film. The arrows in figure B.7 only indicate the maximum of the current distribution.

The currents in the overlapping part, illustrated by dashed lines, has to close the current loops. A detailed study of this part remains open in this work. The field at the cross section of the samples along the dashed line in figure B.1, is illustrated in figure B.8.

The flux inside the gap has to be nearly the same as far above the sample but focused by about half the width of each single strand. Note that this assumption can only be made if the gap is sufficiently wide and therefore the local field of the at the inner edges is small compared to the penetration field B_p .

B Coupling losses in different geometries

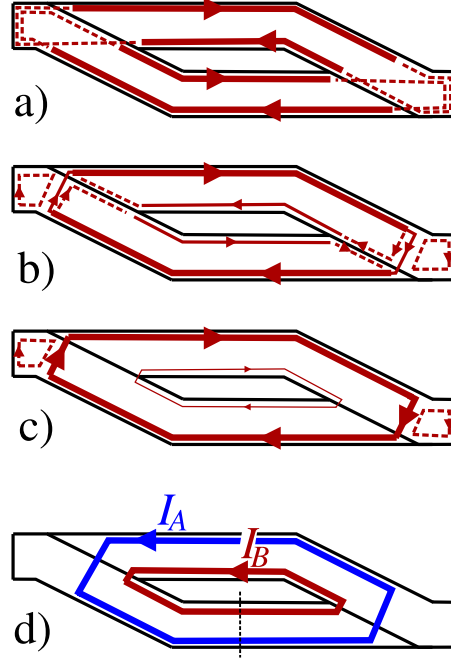


Figure B.7: Current distribution at maximum applied field (H_0 , cf. figure B.11) in (a) the uncoupled, (b) an intermediate- and (c) the fully coupled case. Panel (d) illustrates the formal approach of describing (a),(b) and (c) with two circular flowing currents.

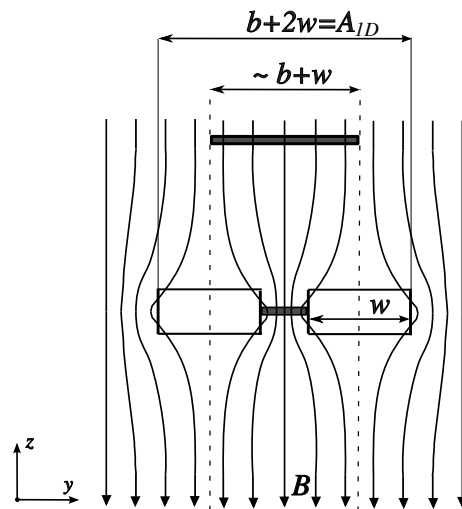


Figure B.8: Flux focusing between two coplanar parallel strips in the uncoupled case.

B Coupling losses in different geometries

This so-called flux focusing effect was calculated and discussed in detail for infinite coplanar parallel bulk pinning free stripes in the Meissner-state [39] and for penetrating fields [40][41].

With increasing frequency, the induced voltages and coupling currents begin to play a role. Hence, currents flow over the resistive connections in the outer loop (see figure B.7b), whereas the inner currents decrease. At the resistive connections, the induced voltage leads to the coupling losses. An intermediately coupled situation takes place. Increasing the frequency further leads to a field-free gap with clockwise flowing currents shielding the whole superconductor. This fully coupled situation is sketched in figure B.7c. Note that the current close to the gap flows now in the same direction as the coupling current holding the gap field-free.

One can formally describe all three situations using two circular flowing currents. These currents are denoted as I^A and I^B in figure B.7d. The indices A and B denote different current distributions with different duties. I^A shields the superconductor from the applied field, whereas I^B generates the field inside the gap.

Note that I^A primarily shields the superconductor and not the gap. Hence, a small amount of flux $\Phi^{A,gap}$ would penetrate through the resistive connections and remain in the gap if I^B is zero.

In order to end up in the uncoupled situation, one can say that a current $I_{uncoupled}^B$ has to generate the flux difference between the focused flux $\Phi_{uncoupled}^{gap}$ and $\Phi^{A,gap}$ or

$$\Phi_{uncoupled}^{gap} = \Phi^{A,gap} + \Phi_{uncoupled}^{B,gap} \quad (\text{B.12})$$

Note that in (B.12) the applied field is already considered in $\Phi^{A,gap}$ and $\Phi_{uncoupled}^{B,gap}$ which are functions of the applied field H_a , as will be shown later. The net current in each strip flowing through the parallel cross-section, indicated by the dashed line in figure B.7d, has to be zero and therefore one finds in the uncoupled case:

$$I_{net} = I^A + I_{uncoupled}^B = 0 \quad (\text{B.13})$$

I^A is flowing with the phase π to the applied field and shields the superconductor, whereas $I_{uncoupled}^B$ is in phase with the applied field in order to produce the focused flux.

In the fully coupled case I^A is still shielding the whole superconductor and the coupling current has to cancel $I_{uncoupled}^B$ (which generates $\Phi_{uncoupled}^{B,gap}$) and further provide a small $I_{fullycoupled}^B$, generating formally equivalent $-\Phi^{A,gap}$ to hold the gap field-free.

These considerations lead to the conclusion that the distribution of the coupling current has to be the same as the current distribution of I^B . Therefore, the inductance for low fields is given by:

$$L_{lf} \approx \frac{\Phi_{uncoupled}^{B,gap}}{I_{uncoupled}^B} \quad (\text{B.14})$$

B Coupling losses in different geometries

In all coupling situations, the net current in one strip follows:

$$I_{strip} = I^A + I_{uncoupled}^B + I_{coupling}^B \quad (\text{B.15})$$

where the phase of $I_{coupling}^B$ to the applied field is $-\pi/2 - \varphi$. The $-\pi/2$ shift follows directly from (B.9) assuming a sinusoidal field. The phase φ depends on the inductance of the sample, the resistivity of the connections and the frequency of the applied field and will be calculated later.

In the uncoupled case or at very low frequencies the coupling current becomes zero and (B.15) reduces to (B.13) and the focused flux from (B.12) $\Phi_{uncoupled}^{gap}$ is inside the gap.

In the fully coupled case, the phase of the coupling current $I_{coupling}^B$ to the applied field is π ($\varphi = \pi/2$), cancelling $I_{uncoupled}^B$ and adding some additional current to hold the gap completely field-free.

Since an analytic examination of the focused flux $\Phi_{uncoupled}^{gap}$ and the inductance problem would go beyond the scope of this work, a few assumptions had to be made for the application of existing equations.

The focused flux, current density distributions of I_A and I_B , and the already discussed inductance were calculated for infinite coplanar bulk pinning free parallel stripes in the Meissner-state by Brojeny et al. [39] in one dimension. If strong pinning centres and low fields are assumed, the flux and current distribution should not change drastically for fields slightly above B_{c1} .

Similar to the uncoupled case of figure B.7a, the focused flux per unit length inside a gap of two coplanar strips, assuming only Meissner currents, was found as Case D in [39]:

$$\Phi_{uncoupled}^{1D,gap} = \mu_0 H_a (b + 2w) \frac{\pi/2}{\mathbf{K}(k')} \quad (\text{B.16})$$

where $(b + 2w) = A_{1D}$ is the distance between the outer edges of the stripes, as marked in figure B.8, \mathbf{K} is the complete elliptic integral of the first kind $k = (b/2)/(b/2 + w)$ and $k' = \sqrt{1 - k^2}$. The flux inside the gap, generated by a current I_B , was found as Case B in [39]:

$$\Phi_B^{1D,gap} = \mu_0 H_{0,c} (b + 2w) \mathbf{K}(k) \quad (\text{B.17})$$

where $H_{0,c}$ is a characteristic field. The net current density distribution in the uncoupled situation is zero in each strip. The current density distribution for I^A is given by Case A in

B Coupling losses in different geometries

[39]:

$$J^A = -\frac{2H_a}{d} \frac{x}{|x|} \frac{(x^2 - (\frac{b}{2})^2)^{1/2}}{((\frac{b}{2} + w)^2 - x^2)^{1/2}} \quad \frac{b}{2} < |x| < \frac{b}{2} + w$$

$$= 0 \quad \textit{otherwise} \quad (\text{B.18})$$

The current density distribution for I^B is given by Case B in [39]:

$$J^B = 2 \frac{H_{0,c}}{d} \frac{x}{|x|} \frac{(\frac{b}{2} + w)^2}{\left((x^2 - (\frac{b}{2})^2) \left((\frac{b}{2} + w)^2 - x^2 \right) \right)^{1/2}} \quad \frac{b}{2} < |x| < \frac{b}{2} + w,$$

$$= 0 \quad \textit{otherwise} \quad (\text{B.19})$$

and the current is calculated with:

$$I^B = 2H_{0,c} \left(\frac{b}{2} + w \right) \mathbf{K}(k') \quad (\text{B.20})$$

The characteristic field $H_{0,c}$ is given in the uncoupled case by Case D in [39]:

$$H_{0,uncoupled} = H_a \left(\frac{\mathbf{E}(k')}{\mathbf{K}(k')} - k^2 \right) \quad (\text{B.21})$$

and for the coupling current by Case B in [39] with:

$$H_{0,coupling} = \frac{I_{coupling}}{2(\frac{b}{2} + w) \mathbf{K}(k')} \quad (\text{B.22})$$

where \mathbf{E} is a complete elliptic integral of the second kind. Combining the equations from Brojny et al. with the considerations from the Roebel loops, the current distribution in the low field regime results from (B.15), (B.18) and (B.21), (B.22) used in (B.19):

$$J_{coupled} = J^A + J_{uncoupled}^B + J_{coupling}^B$$

$$= \frac{2}{d} \frac{x}{|x|} \frac{1}{(x^2 - (\frac{b}{2})^2)^{1/2}} \frac{1}{(\frac{b}{2} + w)^2 - x^2)^{1/2}} \cdot$$

$$\cdot \left[H_a \left(\left(\frac{b}{2} \right)^2 - x^2 + \left(\frac{\mathbf{E}(k')}{\mathbf{K}(k')} - k^2 \right) \left(\frac{b}{2} + w \right)^2 \right) + \frac{I_{coupling} (\frac{b}{2} + w)}{2 \mathbf{K}(k')} \right] \quad (\text{B.23})$$

B Coupling losses in different geometries

which simplifies in the uncoupled case to:

$$\begin{aligned}
 J_{uncoupled} &= J^A + J_{uncoupled}^B \\
 &= \frac{2}{d} \frac{x}{|x|} \frac{1}{(x^2 - (\frac{b}{2})^2)^{1/2}} \frac{1}{(\frac{b}{2} + w)^2 - x^2)^{1/2}} \cdot \\
 &\cdot H_a \left(\left(\frac{b}{2} \right)^2 - x^2 + \left(\frac{\mathbf{E}(k')}{\mathbf{K}(k')} - k^2 \right) \left(\frac{b}{2} + w \right)^2 \right)
 \end{aligned} \tag{B.24}$$

Figure B.9 shows the resulting current distributions in the uncoupled case, $J_{uncoupled}$, from B.9 as well as $J_{uncoupled}^A$ (B.18) and $J_{uncoupled}^B$ (B.19). The calculations in figure B.9 are based on the parameters of the long coupled sample at a field of 2 mT.

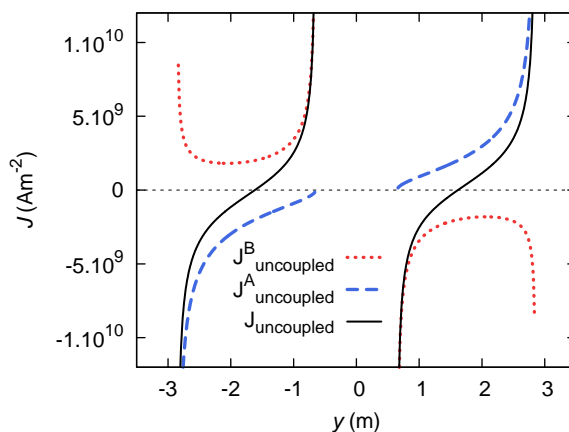


Figure B.9: Calculated current distribution according to (B.24).

The current distributions of the coupled case $J_{coupled}$ (B.23) at maximum applied field ($\mu_0 H = -2$ mT at $t = T/4$) and for various frequencies are shown in figure B.10 using (B.30) for $I_{coupling}^B$. Once again the parameters of the long coupled sample are used.

In the uncoupled case in figure B.10, $J_{coupling}^B$ according to (B.23) is zero and the current distribution is again given by $J_{uncoupled}^A$ and $J_{uncoupled}^B$. With increasing frequency, the coupling current $J_{coupling}^B$ becomes higher until the fully coupled situation is reached. As already discussed in figure B.7c, small currents close to the gap have to flow in order to shield the gap and therefore prevent any further enhancement of the coupling current.

B Coupling losses in different geometries

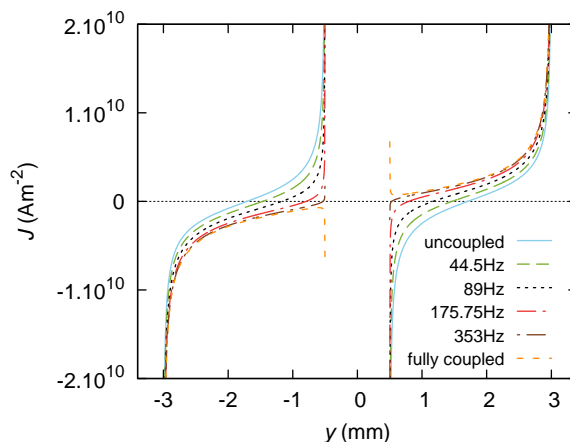


Figure B.10: Calculated current distribution for the long coupled sample according to (B.23) at a maximum applied field of 2 mT ($t=T/4$).

Note that the currents do not behave as in figure B.10 over the whole time period for alternating fields. Due to the frequency dependent phase between induced voltage and coupling current density $J_{coupling}^B$, the maximum of the coupling current occurs between zero and $T/4$. This phenomenon is illustrated in figure B.11 and will be discussed further below.

For Roebel loops, one-dimensional considerations have to be extended to develop the two-dimensional problem. Imagine a rectangular wire loop of length a' and height b' . Multiplying a flux per unit length, which is calculated for the distance b' for an infinitely long loop (denoted with Φ^{1D}), with a length a' , would lead to a flux density inside a rectangular area of $\Phi_{rect} = \Phi^{1D} a' = \Phi^{1D} a' b' / b' = \Phi_{1D} A_{rect} / b'$.

The flux calculated in this way would underestimate the generated flux by neglecting the closing currents at the ends. Nevertheless, in order to take advantage of a simple solution, the calculated flux per unit length from (B.16) can be used for the focused flux in our samples:

$$\Phi_{uncoupled}^{gap} = \Phi_{uncoupled}^{1D,gap} \frac{A_{out}}{A^{1D}} = \mu_0 H_a A_{out} \frac{\pi/2}{\mathbf{K}(k')} = \mu_0 H_a A_{lf} \quad (\text{B.25})$$

where A_{out} is the area, marked in figure B.14 with $V^{outside}$, given by:

$$A_{out} = \left(a + w \left(\frac{1}{\tan \frac{\alpha}{2}} + \tan \frac{\alpha}{2} \right) \right) (b + 2w) - 2w^2 \tan \frac{\alpha}{2} \left(\frac{1}{\sin \frac{\alpha}{2}} - 1 \right)^2 \quad (\text{B.26})$$

and

$$A_{lf} = A_{out} \cdot \pi/2 \cdot 1/\mathbf{K}(k') \quad (\text{B.27})$$

A_{lf} equals an effective area at low fields. Roughly, A_{lf} is given by $a(b+w)$ (see figure B.8 and figure B.1). However, in this work the more accurate effective area according to (B.27) is used.

B Coupling losses in different geometries

In order to find an equation for the inductance, similar considerations can be used for $\Phi_B^{1D,gap}$ in (B.17). Using (B.14),(B.17) and (B.20), one finds finally for the inductance in low fields:

$$L_{lf} = \mu_0 \mathbf{K}(k)/\mathbf{K}(k') \frac{A_{out}}{A_{1D}} \quad (\text{B.28})$$

where $A_{1D} = (b + 2w)$ (see figure B.8). Table B.3 shows the calculated values of L_{lf} for each sample. From Faraday's law (B.9) follows:

$$V_{ind}^{lf} = - \iint \dot{B}_{gap} dA_{gap} = -\dot{\Phi}_{uncoupled}^{gap} = -\mu_0 \dot{H}_a \cdot A_{lf} \quad (\text{B.29})$$

For $I \ll I_c$ the contribution of the superconductor in (B.10) can be neglected. Using the complex Fourier description, one finally obtains:

$$I_{coupling}^{lf} = \frac{1}{R} \frac{V_{ind}^{lf}}{1 + \omega^2 \frac{L_{lf}^2}{R^2}} \left(1 - j\omega \frac{L_{lf}}{R} \right) \quad (\text{B.30})$$

where $j = \sqrt{-1}$. The phase between voltage and current is therefore given by:

$$\varphi = \text{atan} \left(\omega \frac{L_{lf}}{R} \right) \quad (\text{B.31})$$

For large dimensions (i.e. high inductance), high frequencies and/or low resistivity, the phase between current and voltage is close to $\pi/2$, i.e. the field generated by the coupling currents is opposite to the applied field and shields the gap. For small dimensions and low frequencies, the phase between induced voltage and current shifts towards zero and the applied field is in phase with the generated field inside the gap, as $|I_{coupling}|$ becomes zero. Using

$$P = \text{Re} \{ V_{ind} \cdot I_{coupling} \} \quad (\text{B.32})$$

(B.11), (B.29), (B.30) and

$$Q_{coupl} = \frac{1}{l} \int_{-\frac{T}{2}}^{+\frac{T}{2}} P dt \quad (\text{B.33})$$

one finds a final equation for the coupling loss in the low field regime:

$$Q_{coupl}^{lf} = \frac{2}{l} \cdot A_{lf}^2 \cdot \pi^2 \cdot \frac{f \cdot \mu_0 H_0^2}{R} \cdot \frac{1}{\omega^2 \frac{L_{lf}^2}{R^2} + 1} \quad (\text{B.34})$$

where l is the characteristic length of the sample. Comparing (B.34) with equations from Wilson [8]

$$Q_{coupl} \propto \frac{\omega\tau}{(\omega\tau)^2 + 1} \quad (\text{B.35})$$

B Coupling losses in different geometries

the relaxation time τ is L/R and the critical frequency

$$f_c = \frac{1}{2\pi} \frac{R}{L} \quad (\text{B.36})$$

Since the area A_{lf} is squared in (B.34), the dimensions of the gap and especially the width of the tape are crucial for the coupling loss.

Figure B.11 shows the time dependent results of (B.11), (B.29), (B.30) and (B.32) for different frequencies during one time period for the coupled long sample.

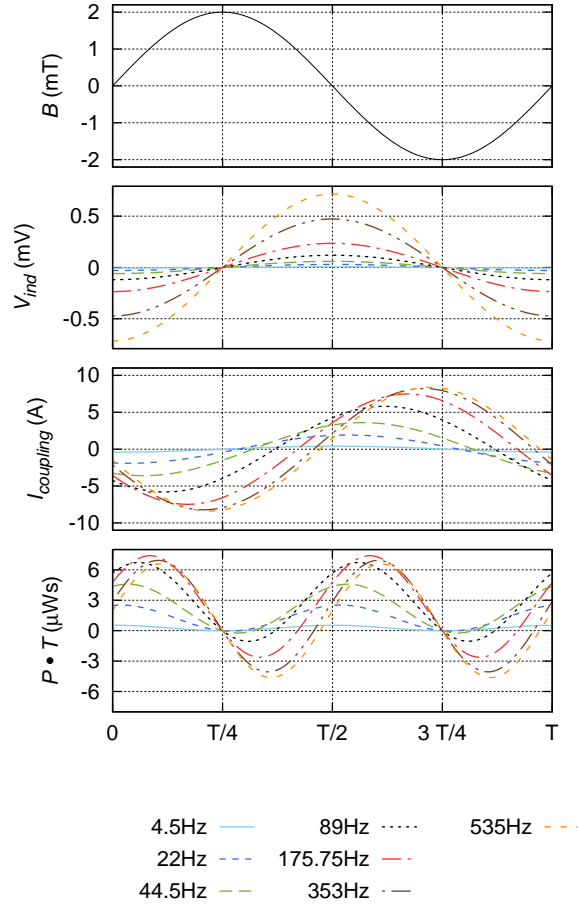


Figure B.11: Calculated behaviour at a low AC field for the long coupled sample ($f_c=95$ Hz) calculated from (B.11), (B.29), (B.30) and (B.32). Note that negative coupling currents $I_{coupling}$ circulate clockwise, i.e. have negative values of I_x for $y < 0$ and positive values for $y > 0$ if $y = 0$ in the centre of the gap (see also dashed line and coordinate system in figure (B.1)).

B Coupling losses in different geometries

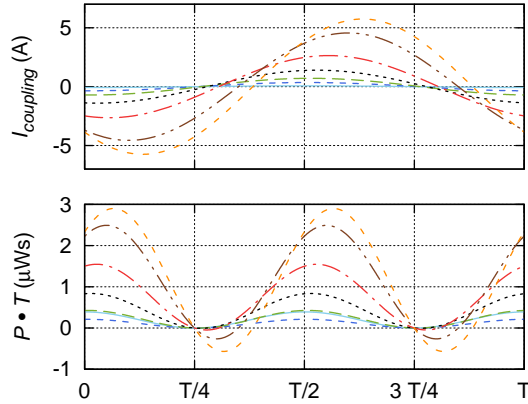


Figure B.12: Calculated coupling current and loss for the intermediately long high resistive sample ($f_c=502$ Hz) for different frequencies. The colour code is identical with figure B.11.

With increasing frequency the induced voltage in figure B.11 increases according to (B.29). The phase shift (B.31) of the coupling current leads to a non trivial current distribution in the strands at different times, as will be demonstrated later. The phase shift also leads to the maximum of the loss per cycle Q at the critical frequency. The frequency dependent maximum of the loss is hard to see in the plot of $P \cdot T$ in figure B.11, but the integral over one period is higher at 89 Hz (close to the critical frequency) than at higher frequencies. With increasing frequency, the losses become reactive losses, as indicated by the negative values of the losses. Hence the integral over time and therefore Q become increasingly smaller at higher frequencies. In other words, at low frequencies the loss is determined by the absolute value of the coupling current (which is low for low frequencies) and at high frequencies the loss is determined by the phase shift of 90° , resulting in high reactive losses and relatively small ohmic losses. In between, at the critical frequency (at $\varphi = 45^\circ$) the ohmic losses have their maximum.

Figure B.12 shows calculations for the intermediately long high resistive sample. Due to the higher critical frequency of 502 Hz, the phase shifts only by up to about 45° at 535 Hz. Note that the time dependent loss per cycle $P(t) \cdot T = P(t)/f$ is illustrated in figure B.11 and figure B.12 for a better comparison of the different frequencies.

B.3.3 High field regime (coupling current $I_{coupling} \geq I_c(0 \text{ T})$)

For high fields, full penetration of the applied field into the sample is assumed. The field generated by the shielding currents is much smaller than the applied field.

B Coupling losses in different geometries

In the uncoupled or DC field-case, currents flow with $I_c(B)$ similar to figure B.7a reducing the field inside the strands. A changing field induces an electric field in the whole superconductor. In the coupled case, the electric field reverses the intrinsic inner shielding currents if the coupling current is $I_{coupling}^{hf} > I_c(B)$. Thus, the shielding current ($I_{coupling}^{hf}$) flows circularly around the whole sample trying to shield the entire geometry. Therefore, the intrinsic shielding currents can be neglected in all further considerations and the shielding generated by the coupling current is considered in the following. Similar to the low field regime, the inductances of the Roebel loops are once again calculated from the magnetic moment per unit length between two coplanar parallel strands. Due to the assumption of $I_{coupling}^{hf} > I_c$ and the power law, the current should be distributed nearly equally over the whole cross-section. The field distribution $B_{z,Brandt}$ caused by a transport critical current in a thin film can be taken from [35]. Superposition of the fields of the oppositely flowing currents gives the resulting field distribution of two parallel conductors. Integration over the inner field leads to the flux per unit length between the two strands. One finds after elementary calculations:

$$\Phi_{hf}^{1D} = \int_{-y_0}^{y_0+w+b} B_{z,Brandt} dy = \mu_0 H_c \left(\frac{w}{2} \ln \left(1 - \frac{w+b}{y_0} \right) - 2(w+b) \operatorname{atanh} \left(\frac{2y_0}{w} \right) \right) \quad (\text{B.37})$$

where $H_c = I_c/(\pi w)$ and y_0 denote the y -position where the field changes sign. Point y_0 is calculated from $y_0^2 - (w+b)y - w^2/4 = 0$. Figure B.13 illustrates the field of two coplanar strips with oppositely flowing currents of I_c .

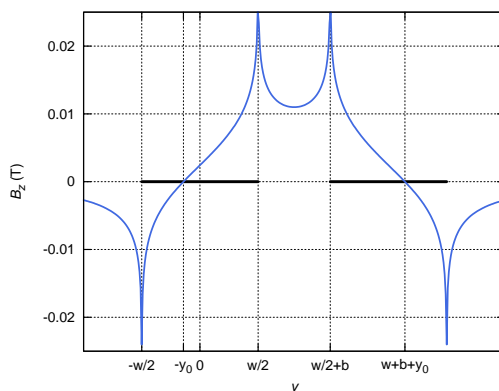


Figure B.13: Magnetic field distribution of two infinite parallel strips of width w and oppositely flowing currents. The distance between the two strips is b .

Almost over the whole period, I_c , and therefore the flux generated by the I_c -current distribution (Φ_{hf}^{1D}), determines the inductance. With the same considerations as in (B.25) and (B.28)

B Coupling losses in different geometries

one finds for the inductance:

$$L_{hf} \approx \frac{\Phi_{hf}}{I_{coupling}} = \frac{\mu_0}{\pi} \left(\frac{1}{2} \ln \left(1 - \frac{w+b}{y_0} \right) - 2 \left(1 + \frac{b}{w} \right) \operatorname{atanh} \left(\frac{2y_0}{w} \right) \right) \frac{A_{out}}{A_{1D}} \quad (\text{B.38})$$

Here the absolute value of $I_{coupling}$ depends on the magnetic and electric field, but the spatial current distribution is given by the I_c -current distribution, as discussed previously. Hence $I_{coupling}$ is used instead of I_c in (B.37) leading to (B.38). The electric field is lowest at the inner edge of the loop and increases with the area of the enclosed magnetic field to its maximum at the outer edge. In the following, we assume that $I_{coupling}^{hf} > I_c(B)$ is reached very rapidly, as we consider high fields. Therefore, we overestimate the hysteresis losses during the short time when the coupling currents are smaller than the inner shielding currents of the superconductor. In order to calculate the loss, the induced voltage V_{ind} has to be calculated using Faraday's law (B.9). The induced voltage on the inner edge of the loop is given by:

$$V_{ind}^{inside} = - \iint \dot{B} \, dA = -\dot{B} \cdot A_{inside} = -\dot{B} \cdot a b \quad (\text{B.39})$$

and the voltage on the outer edge by:

$$V_{ind}^{outside} = - \iint \dot{B} \, dA = -\dot{B} \cdot A_{outside} \quad (\text{B.40})$$

Both voltages are indicated in figure B.14.

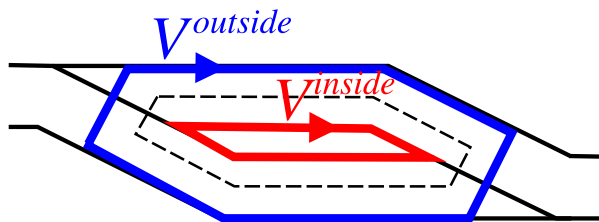


Figure B.14: Voltage applying on the samples edges as defined in (B.39) and (B.40)

The mean value for the induced voltage can be written as:

$$V_{ind}^{hf} = -\dot{B} \cdot \left(A_{inside} + \frac{A_{outside} - A_{inside}}{2} \right) = \dot{B} \cdot A_{hf} \quad (\text{B.41})$$

where again an effective area is introduced:

$$A_{hf} = l(w+b) - b \left(b \cot \alpha + w \cot \frac{\alpha}{2} \right) - 2 \frac{w^2}{\sin \alpha} \left(1 - \sin \frac{\alpha}{2} \right)^2 \quad (\text{B.42})$$

B Coupling losses in different geometries

The induced voltage V_{ind}^{hf} from (B.41) is used as V in (B.10). Thus, the differential equation for I can be solved numerically by the Euler formalism for several time periods and therefore the coupling current $I_{coupling}^{hf}(t) = I(t)$ is found.

The loss can be calculated from:

$$P_{coupl}^{hf}(t) = V_{ind}^{hf}(t) I_{coupling}^{hf}(t) = \mu_0 \dot{H}(t) A_{hf} I_{coupling}^{hf}(t) \quad (\text{B.43})$$

and (B.33).

Figure B.15 shows the calculated properties at different applied fields. The dimensions of the long coupled sample were taken for these calculations.

The field dependences of I_c and the n – value are crucial in these calculations. Both values were calculated with (B.49) and (B.50) from experimental single strand data.

I_c and the n – value reach their maximum values in the absence of an applied field at $t = 0$ and $t = T/2$.

At $t=0$, the induced voltage and $I_c(B)$ have a maximum. Therefore, the coupling current has a maximum and due to the high induced voltage, the coupling current is significantly larger than the self-field $I_c(0)$. With increasing field (0 to $T/4$) the critical current of the strand and the induced voltage decrease. At $T/4$, the coupling current is reduced compared to $I_c(0)$ by approximately the same amount as it was enhanced compared to $I_c(0)$ at $t=0$. At $t=0$ the induced voltage dominates the coupling current (enhancement compared to $I_c(0)$) whereas close to $T/4$, the field dependence of I_c dominates (reduction compared to $I_c(0)$). Both effects lead to a slightly changing coupling current (between 0 and $T/4$) with a mean value, which is approximately the self-field I_c . We will see later, that the assumption of a field independent constant I_c will give a good approximation for the losses in our sample (see also figure B.34 on page 59) although it does not describe the entire physics. The short time span when the coupling current changes sign is the time when the coupling current is smaller than $I_c(B)$. During this time, the assumption $I_{coupling}^{hf} > I_c(B)$ is not fulfilled. At higher applied fields, this time span becomes shorter. Note that the phase between coupling current and induced voltage shifts towards zero with higher fields due to the increasing resistivity of the superconductor compared to the constant inductance.

Due to the nearly constant coupling current, the magnitude of the loss mainly depends on the induced voltage. Note that the loss has distinct maxima at 0 and $T/2$.

Finally the loss per unit length can be calculated using (B.33):

$$Q_{coupl}^{hf} = \omega \mu_0 H_0 \frac{A_{hf}}{l} w \int_{-\frac{T}{2}}^{+\frac{T}{2}} J_{coupling}^{hf}(H, t) \cos(\omega t) dt \quad (\text{B.44})$$

B Coupling losses in different geometries

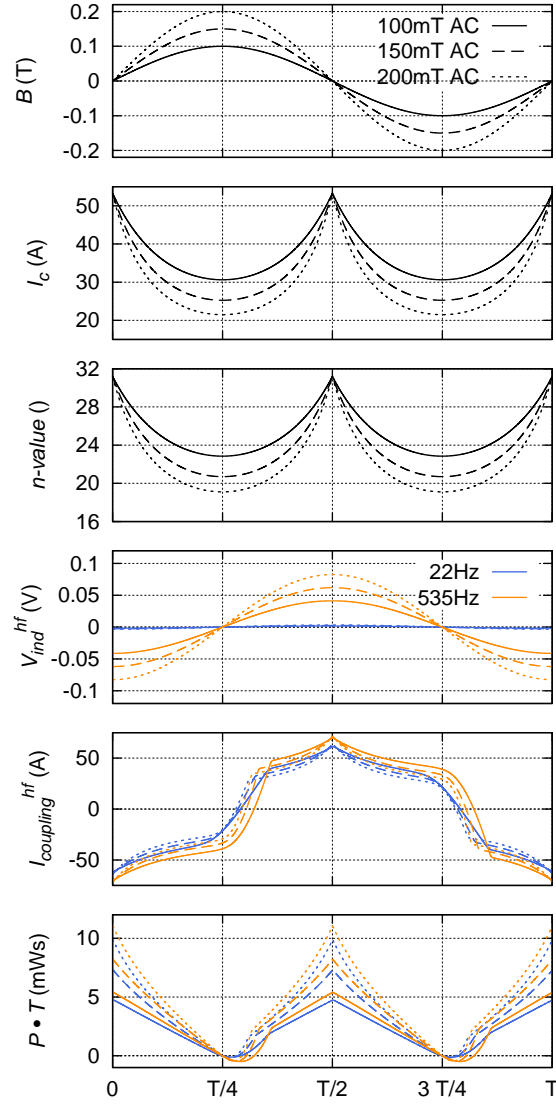


Figure B.15: Calculated behaviour at different applied AC fields for the long coupled sample. Solid lines refer to 100 mT, dashed lines to 150 mT and dotted lines to 200 mT. The frequency is 22 Hz (blue) and 535 Hz (orange) in the lower three panels.

B Coupling losses in different geometries

where $J_{coupling}^{hf} = w d_{sc} I_{coupling}^{hf}$ is the current density and d_{sc} is the thickness of the superconducting layer.

If J_c was independent of the magnetic field and the coupling current density was limited by J_c , (B.44) could be solved easily by $J_{coupling}^{hf} = \cos(\omega t) / |\cos(\omega t)| J_c$ for sufficiently high fields ($\varphi \rightarrow 0$), leading to:

$$Q_{coupl}^{J_c=const} = 4 \mu_0 H_0 \frac{A_{hf}}{l} w d J_c \quad (\text{B.45})$$

for the loss per unit length. Note that the frequency dependence disappears in (B.45). As discussed previously, (B.45) is a good assumption in our samples, as the coupling current varies nearly symmetrically around the self-field J_c during a time period.

For two coupled parallel tapes, A_{hf} is given by $a(b+w)$ and therefore (B.45) becomes:

$$Q_{coupl,parallel}^{J_c=const} = 4 \mu_0 H_0 (b+w) w d J_c \quad (\text{B.46})$$

with $l = a$ in a rectangular geometry. For $b = 0$, (B.46) is exactly the hysteresis loss at high fields for a strip with width $2 \cdot w$ calculated by Brandt [35]:

$$Q_{Brandt}^{J_c=const} = 4 \mu_0 (H_0 - 1.386 H_c) w^2 d J_c \quad (\text{B.47})$$

without the reduction of H_0 by $1.386 H_c$. H_c is defined in [35] as $J_c^{(2D)} / \pi$. The discrepancy with (B.46) vanishes for fields $H_0 \gg H_p \gg H_c$, which was assumed in our high field model. Due to the w^2 dependence in (B.47), the hysteresis losses are two times higher if two tapes of the width w were connected to one tape of the width $2 \cdot w$ with superconducting joints. This “superconducting coupling” is often referred to as single block limit and describes an upper loss limit for a fully coupled sample. In other words, if one couples two insulated coplanar parallel strips without a gap, one doubles the losses. Note that this is the main argument for striating tapes.

The situation is different if there is a gap between the strips. In this case, the loss of the fully coupled situation is proportional to $(b+w)w$ as found in (B.46), whereas the loss of each insulated strip is still proportional to $(w/2)^2$. Thus, the upper limit for a fully coupled situation is given by:

$$Q_{upperlimit}^{J_c=const} = \frac{w(b+w)}{\left(\frac{w}{2}\right)^2 + \left(\frac{w}{2}\right)^2} Q_{uncoupled}^{J_c=const}\left(\frac{w}{2}\right) \quad (\text{B.48})$$

where $Q_{uncoupled}^{J_c=const}$ is given by (B.47) without the reduction of H_0 . Thus, in a sample with $w=2$ and $b=1$, the upper loss limit is three times that of the hysteresis losses of the insulated tapes.

Lastly, another effect should be mentioned. The dominant and increasing resistivity of the superconductor in high fields compared to more or less constant inductance L_{hf} leads to a

B Coupling losses in different geometries

phase shift and a corresponding shift of the critical frequency f_c of the loop to higher values. The phase shift was also calculated numerically and can be found in measurements of the long coupled sample in the following section. Note that the existence of a critical frequency similar to the low field case with a decreasing loss above this frequency was not measured in this work and is not expected at high fields. In the numerical calculation, a decrease of loss was only found for very high frequencies (MHz) where the model is no longer valid.

The high field method developed can also be used to calculate the losses of AC ripples at high DC fields. Figure B.16 shows the result of different AC fields in a 1 T background field.

At 1 T, I_c and n – value respectively change more or less sinusoidal around 7.25 A and 11.2, due to the DC background field. Hence, the critical current is more or less constant. The coupling current appears rectangular, as expected from a field independent critical current. Note that the more or less constant coupling current (between T/4 to 3T/4 and 3T/4 to T/4) is higher than $I_c(B)$ due to the high induced voltage. The loss follows the absolute value of the induced voltage since there exists nearly no phase shift between induced voltage and current. The losses are much smaller with an applied DC field, due to the smaller coupling current (smaller I_c), whereas the induced voltage remains the same.

One has to be aware that at high fields and frequencies the surrounding copper acts as a parallel loop and has to be considered. At 1 T DC, 200 mT AC and 22 Hz, the resistivity of the superconductor using the power law would be two orders of magnitude lower than that of the copper surrounding for the long coupled sample. Hence one can neglect the eddy currents in the copper. At a higher frequency of 535 Hz, the resistivity of the superconductor is already half that of the surrounding copper and therefore currents (which are not considered in these calculations) will flow parallel to the superconductor in the samples. Furthermore, induced eddy currents in the copper bridges will disturb the current flow of the coupling currents, leading to an “enhancement” of the bridge resistivity. This effect was found for two 90 mm long parallel tapes connected with 5 mm x 5 mm copper bridges in [37].

B.4 Single Roebel strand characterisation

The transport properties of a single Roebel strand are shown in figure B.17. A 26 mm long piece was cut out of the insulated long sample. Since our model does not consider the parallel copper loops, which become important at high fields, the data were fitted only up to 2 T with the Kim-model:

$$J_c(B) = \frac{J_0}{1 + \frac{B}{B_k}} \quad (\text{B.49})$$

B Coupling losses in different geometries

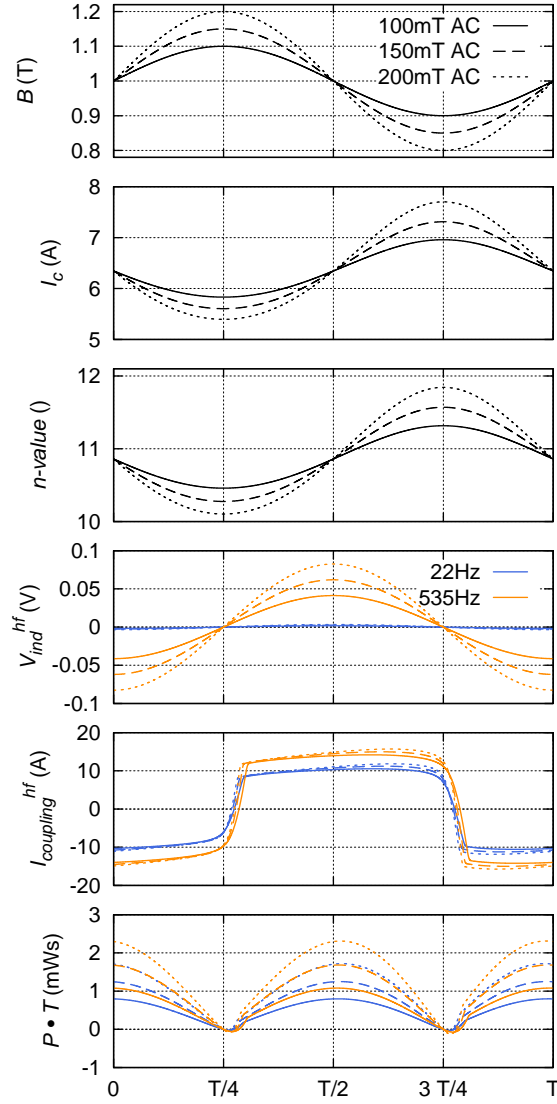


Figure B.16: Calculated behaviour in a constant field of 1 T with an applied ac field for the long coupled sample. Solid lines refer to 100 mT, dashed lines to 150 mT and dotted lines to 200 mT. The frequency is 22 Hz (blue) and 535 Hz (orange).

B Coupling losses in different geometries

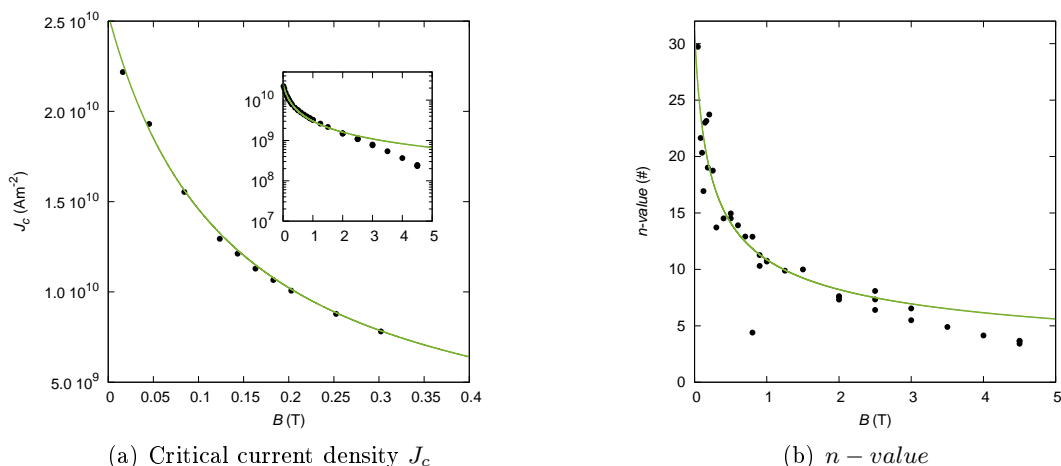


Figure B.17: Field dependence of a 2 mm Roebel single strand at 77 K. Solid lines represents the fit functions (B.49) and (B.50). Note that the fit range was limited by 2 T as no fields higher than 1 T were calculated.

where J_0 and B_k were fitted and resulted in $2.54 \cdot 10^{10} \text{ Am}^{-2}$ and 0.135, respectively. The average self-field was added to the applied field ($\mu_0 H$) resulting in the local field dependence of the critical current $J_c(B)$. The measured self-field J_c^{self} of the strand was about $2.2 \cdot 10^{10} \text{ Am}^{-2}$.

The n - value was fitted by:

$$n(B) = \frac{n_0}{\left(1 + \frac{B}{B_n}\right)^\alpha} \quad (\text{B.50})$$

with $n_0=31.2$, $B_n=0.094$ and $\alpha=0.43$.

B.5 Results of the scanning measurements

B.5.1 Two-strand Roebel loop

In order to investigate field and current distributions in weaker and stronger coupled samples, the intermediately long high resistive sample and the long low resistive sample were chosen for scanning measurements. Line scans perpendicular to the tape direction (y -direction) were performed at the centre of each sample, as indicated by the dashed line in figure B.1 on page 16. Three different AC fields ($\mu_0 H_{max}=2 \text{ mT}$, 26 mT and 50 mT) were applied during the scans. The field of 2 mT was chosen to investigate low field effects. 26 mT corresponds to the penetration field observed in the AC loss measurements in section B.6 and the highest possible field within the frequency range of our set-up was 50 mT.

The applied field was sinusoidal, hence the maximum field occurred at $T/4$ and becoming zero again at $T/2$. Only the first half of the time period ($0-T/2$) is displayed in the following

B Coupling losses in different geometries

figures (B.18 - B.24). The field and current distributions from zero to $T/4$ and from $T/4$ to $T/2$ are illustrated on the left and the right side of the figures, respectively. Since the samples do not have a perfect two-dimensional structure, the distance between Hall probe and strand was not always the same for each strip. Nevertheless, a constant distance was assumed for the inversion of the field of the long sample. For the intermediately long high resistive sample, an angle of 1° according to figure B.5 was assumed. At the two higher fields, the influence of a small defect in the long sample on the left strip is seen as well. Note that the grey shaded areas in the following figures mark the approximate positions of the superconducting strips.

AC scans at 2 mT (low field regime)

In order to show three different coupling situations, the long coupled sample with a calculated critical frequency of about 95 Hz was chosen for the low field limit.

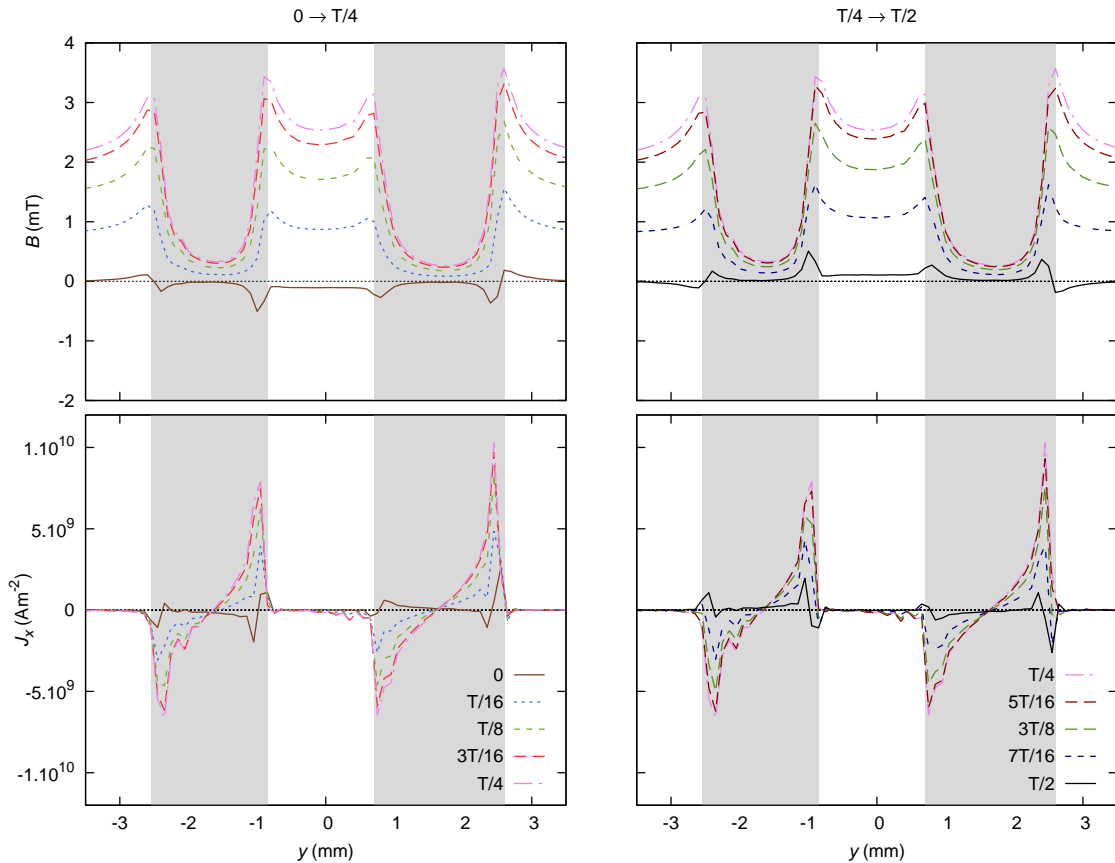


Figure B.18: Low field behaviour of the long coupled sample at 4.5 Hz. Nearly uncoupled case.

B Coupling losses in different geometries

Weak coupling

Figure B.18 shows the (nearly) uncoupled limit at the lowest measured frequency of $f=4.5$ Hz. At the beginning ($t = 0$), trapped fields and the corresponding currents are seen very clearly at the edges of the superconducting strips. In the weakly coupled case, the coupling current has a maximum close to zero and $T/2$ (see figure B.11: 4.5 Hz), but is small due to the low frequency. Nevertheless, the field inside the gap is slightly enlarged at zero field, hence a very small coupling current flows. With increasing field, the shielding currents I^A and the 180° shifted $I_{uncoupled}^B$ increase, whereas the coupling current stays small. Therefore, the coupling current can always be neglected. In other words, the intrinsic shielding currents¹ flow in closed loops at all times in each strip of this sample.

At the maximum field of 2 mT ($t = T/4$), the flux is focused in the gap and therefore the field inside the gap is higher than the applied field. With decreasing field, the field inside the gap follows the applied field in phase, indicating that the coupling current is too small to produce an out of phase field. Remember that the coupling current is at least -90° shifted to the applied field (from (B.9)) and would therefore influence the time dependent field.

Strong coupling

Figure B.19 shows a nearly fully coupled case at $f=535$ Hz. At $t = 0$, a small trapped field and a small field caused by the coupling current are present. At the outer edges, the influence of the trapped flux currents² results in a local current density maximum ($y \approx -2.2$ mm) in the left strip and a local current density minimum ($y \approx 2.5$ mm) in the right strip. The small coupling current (see. figure B.11: 535 Hz) prevents an oppositely flowing trapped flux current, as in the weak coupled situation. At the inner edges, the coupling current and the corresponding field dominate, as the current distribution of the coupling current $I_{coupling}^B$ has a maximum at the inner edge. Although the coupling current becomes nearly zero close to 0 and $T/2$ (see figure B.11: 535 Hz), its influence is still visible. Due to the remaining non-zero field inside the gap, one concludes that the phase φ between induced voltage and current has not reached the fully coupled regime ($\varphi = 90^\circ$). From (B.25) one finds $\varphi=80^\circ$ (according to a phase shift of -10° to I^A or the applied field). Therefore, the induced field “shields” the gap before the field is applied. In other words, $I_{coupling}^B$ flows slightly ahead of the intrinsic shielding current I^A . Nevertheless, the situation is very close to a fully coupled scenario, where the coupling current always cancels $I_{uncoupled}^B$ and, is therefore, in phase with I^A . With increasing field (0 to $T/4$), the coupling current increases and cancels with a slight phase shift $I_{uncoupled}^B$. Thus, at all times mainly I^A flows in the sample corresponding to a current

¹The intrinsic shielding currents were defined at the beginning of section B.3 as the currents shielding each strip in the uncoupled case and causing the hysteresis losses.

²The trapped flux currents were defined at the beginning of section B.3 as the intrinsic shielding currents at $t=0$ or $t=T/2$ (if no field is applied).

B Coupling losses in different geometries

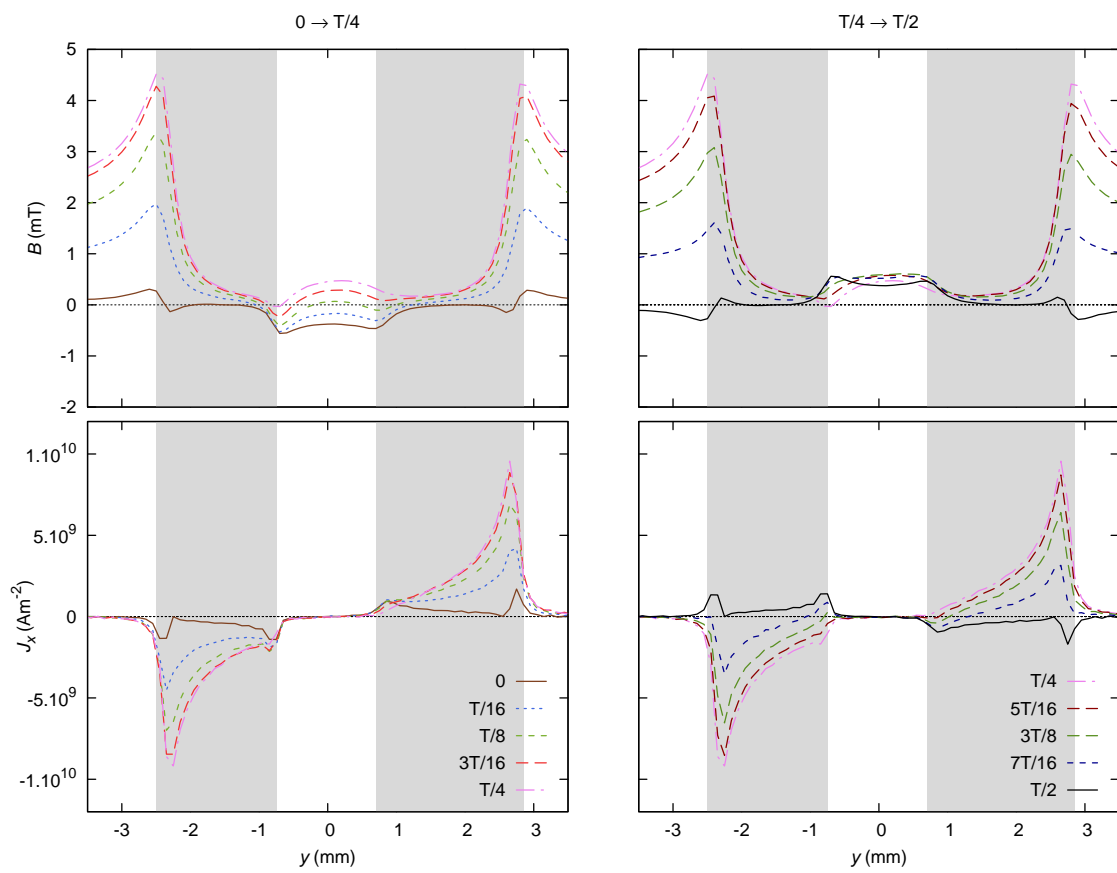


Figure B.19: Low field behaviour of the long coupled sample at 535 Hz. Nearly fully coupled case.

B Coupling losses in different geometries

distribution shielding the whole superconductor. Most of the flux is expelled from the gap and the superconductor, resulting in enhanced local fields at the outer edges.

At the maximum applied field ($T/2$), the current distributions are similar to the calculated distributions for the fully coupled case in figure B.10. Due to the slight phase shift, the current density at the inner edges, where the coupling currents have a local maximum, already decreases between $3T/16$ and $T/4$. With decreasing fields ($T/4$ to $T/2$), the influence of the phase shift at the inner edges is observed again, where the whole current distribution changes the sign after $3T/8$. This is again a result of the ahead flowing $I_{coupling}^B$.

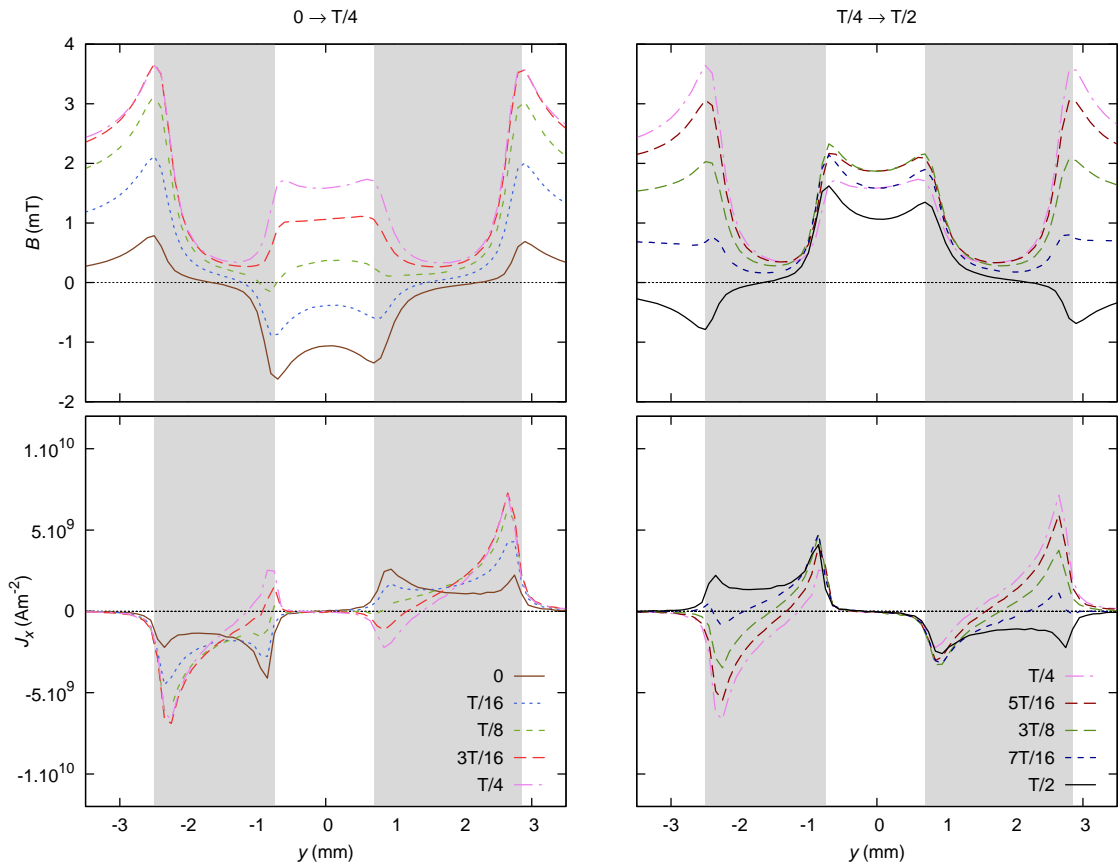


Figure B.20: Low field behaviour of the long coupled sample at 89 Hz. The frequency is close to the critical frequency, hence an intermediate coupling situation occurs.

Intermediate coupling

For all frequencies between the uncoupled and the fully coupled situation, intermediate coupling situations occur. The situation for the sample close to the critical frequency ($f=89$ Hz) is illustrated in figure B.20.

B Coupling losses in different geometries

From figure B.11, one deduces that the coupling current has a maximum at $t \approx T/8$ and becomes zero at $t \approx 3T/8$ (corresponding to $\varphi \approx 45^\circ$ at the critical frequency). At $t = 0$, the field is generated mainly by the coupling current. Since the trapped flux currents are very small compared to the coupling current, the shape of the current density is similar to J^B in figure B.9. This fact justifies the approximation of section B.3.2 to calculate the inductance with the current distribution found by Brojeny et al. [39].

With increasing field, the (absolute) coupling current increases more strongly than the intrinsic shielding currents, reaching its maximum at $T/8$ (see figure B.11: 89 Hz). Hence, a “fully coupled” situation occurs at $T/8$. Increasing the field further allows the intrinsic shielding currents to increase and the (absolute) coupling current decreases. At $T/4$, when the maximum field is applied, a mixed situation arises.

With decreasing field, the shielding currents as well as the absolute coupling current decrease. Since the shielding currents decrease more slowly than the (absolute) coupling current, the focused flux inside the gap increases further. Close to $3T/8$, the coupling current becomes zero and therefore an “uncoupled” situation is found. By decreasing the field further, the coupling current increases, whereas the shielding currents tends to zero at $T/2$. The distribution of the coupling current at $T/2$ mirrors the currents at $t=0$. Due to the non negligible magnitude and the phase of the coupling currents, no trapped flux currents are seen at this frequency.

Such “uncoupled” and “fully coupled” snap-shots within a time period are observed for every frequency but at different times. The “fully coupled” situation occurs at $t = \varphi/360 \cdot T$ when the coupling current reaches its maximum and the “uncoupled” situation occurs at $t = \varphi/360 \cdot T + T/4$. For $\varphi \approx 0^\circ$ or $\varphi \approx 90^\circ$, the uncoupled or the fully coupled situation, respectively, dominate over the whole time period, as discussed previously.

AC scans at 26 mT (penetration field regime)

From the AC loss measurements, a peak in the Γ -plots was found around 26 mT (see section B.6) for all samples. At this peak, the field should be able to penetrate the whole sample, leading to the highest loss factor Γ . The low field assumptions are not valid, as the intrinsic shielding currents are close to I_c . Furthermore, the coupling current is close to I_c for the strongly coupled sample. Therefore, the power law begins to play an important role and the assumption of a constant resistivity R of the loop is invalid either. As the coupling currents are not higher than I_c most of the time, the high field regime is unobtainable.

Weak coupling

In order to show a nearly uncoupled case, the data obtained from the intermediately long

B Coupling losses in different geometries

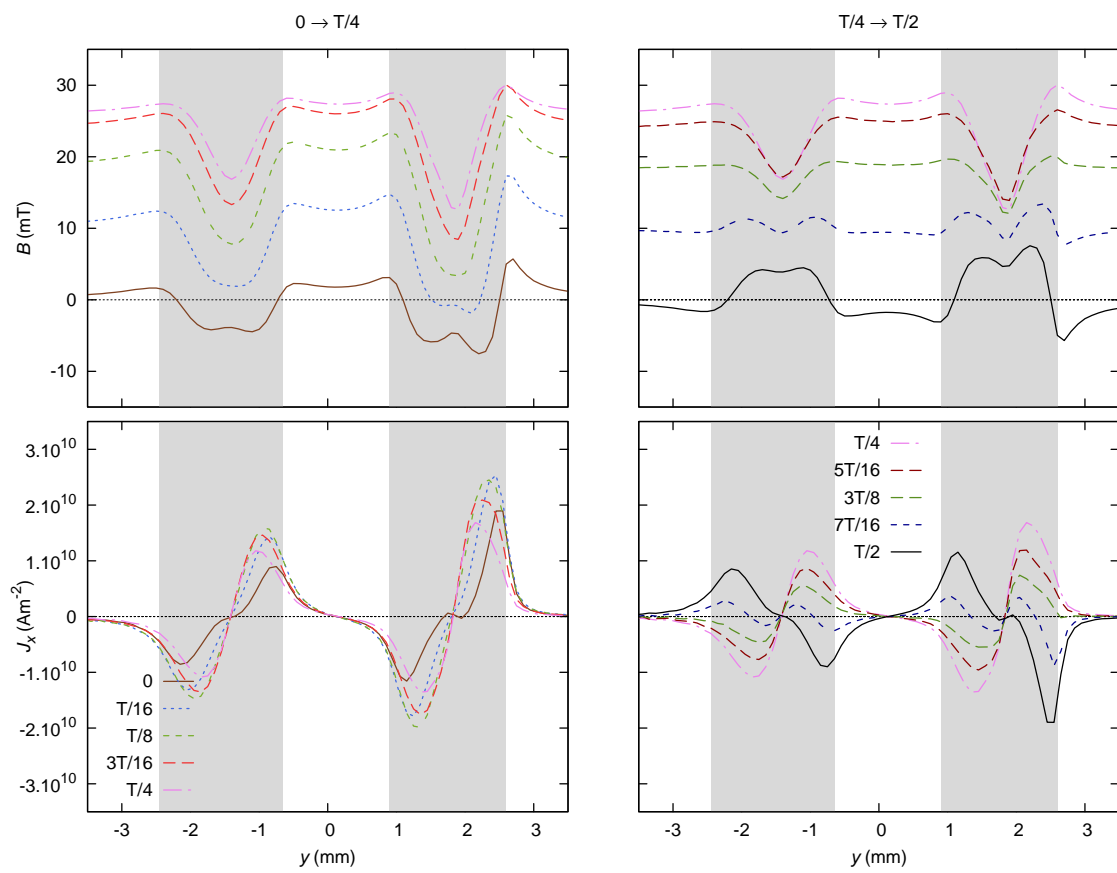


Figure B.21: Intermediate field behaviour of the intermediately long high resistive sample at 22 Hz.

B Coupling losses in different geometries

high resistive sample at 22 Hz is discussed. Note that the left strip of the sample was slightly below the right one and therefore an angle of 1° according to figure B.5 was assumed. Figure B.21 shows the nearly uncoupled situation.

At $t=0$, the remanent field of uncoupled strips is trapped in each strand. The minimum of each field profile is a result of incomplete flux penetration. The field at the centre of each strip should still be nearly zero at maximum applied field if the penetration field equals the maximum applied field. In the present situation, the applied field seems to be slightly above B_p , resulting in small oppositely flowing currents in the centre of each strip at $t=0$ (see J_x of the right tape).

The shielding currents increase further with increasing field, reversing the trapped flux currents at the centre. For fields above 20 mT ($t > T/8$), the field dependence of I_c is already important. The gradient of the field becomes smaller and indicates that the current density decreases. The current maximum moves towards the centre of the strip. Due to the field dependence of I_c , the superconductor is unable to shield as much flux at $T/4$ as at $T/16$ inside each superconducting strip. Note that the gradients of the currents decrease at the inner and outer edges of the superconducting strips up to $T/4$.

The currents at the edges reverse at decreasing field, reducing the net current and generating two field domes in each strip. This effect is observed from $3T/8$ to $T/2$, but should have already started once the maximum field had been reached at $T/4$. The minimum field inside the superconductor at $3T/8$ is about twice the minimum at $T/8$. The shielding capability is reduced by about a factor of two due to the trapped flux behaviour (i.e. the backwards flowing currents at the outer edges of each strip). At $7T/16$ the oppositely flowing currents can be seen clearly.

Strong coupling

Figure B.22 shows the local fields and currents of the long coupled sample at 353 Hz.

At $t=0$, the current flowing inside the strips has a flat local maximum at the outer edges and would be able to shield almost the entire sample if a positive field were applied. Note that this current distribution is completely different from the current distribution at low frequencies for the coupled sample. The trapped flux currents, as previously shown, are much stronger and influence the shape of the distribution. Furthermore, the field is now able to penetrate the strip-centre and therefore the coupling current has to shield more than the gap. Here, the coupling current reverses the oppositely flowing trapped flux currents at the inner edges and therefore the currents flow only in one direction in each strip. Due to the current distribution of the intrinsic shielding currents (see $t=0$ in figure B.21), the current is lower at the inner edges than at the outer edge at $t=0$.

B Coupling losses in different geometries

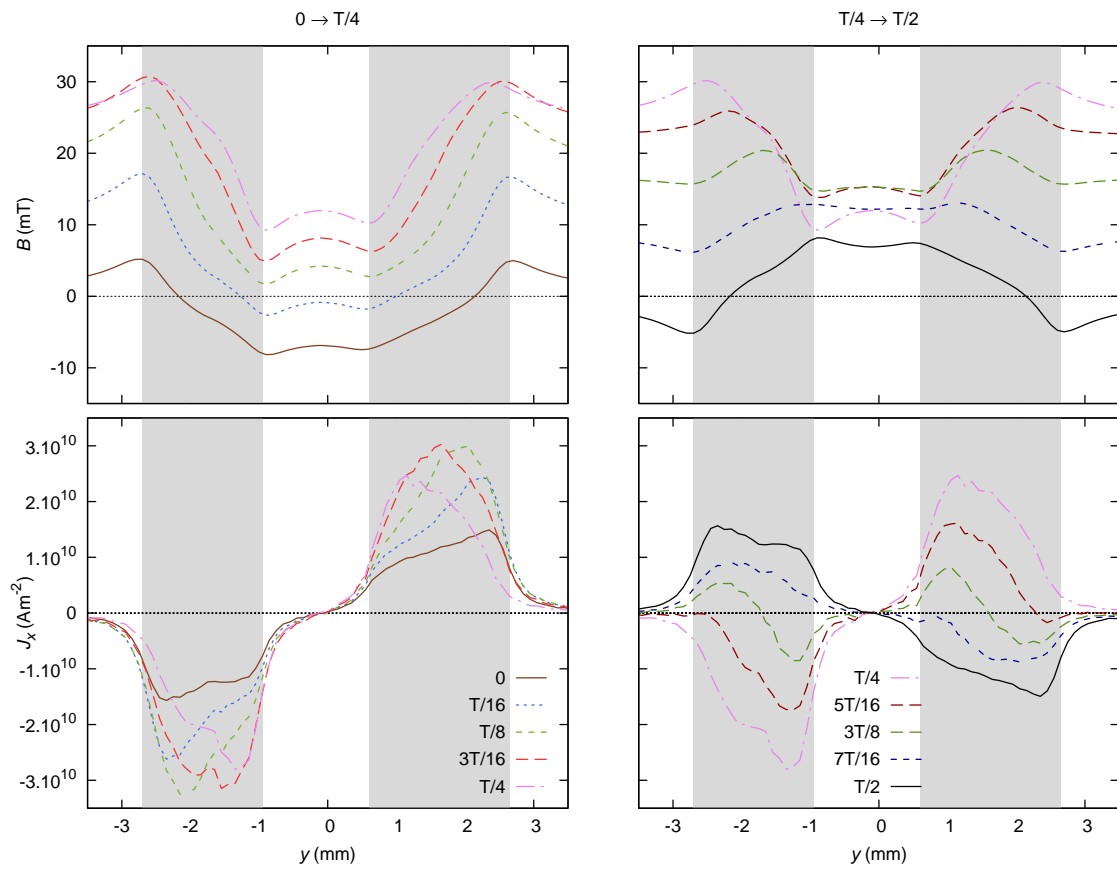


Figure B.22: Intermediate field behaviour of the long coupled sample at 353 Hz.

B Coupling losses in different geometries

Up to $T/8$, the currents increase trying to shield the entire sample. After $T/8$, I_c decreases because of the magnetic field, but on the other hand the coupling current is still increasing. This is indicated by the slight increase of the maxima at the inner edges of the current distribution. In the weakly coupled case, they are already reduced at this time. Note that the maximum of the current distribution shifts towards the centre due to these effects. After $3T/16$, the coupling current reaches its maximum and the field dependence wins, resulting in a reduction of the current maximum at $T/4$.

With decreasing field, the currents should change their direction at the inner and outer edges. This effect was clearly seen at lower frequencies (not depicted) if the coupling currents were already lower. At 353 Hz, the backwards flowing currents are only observed at the outer edges. If a transport current flows in one direction similar to the current distribution at $T/4$, a reduction of the net current would take place by symmetric reverse flowing currents. As the backwards flowing currents are only visible at the outer edges at 353 Hz, one can conclude that the coupling currents close to the inner edge are still higher than the backwards flowing intrinsic shielding currents. At $7T/16$, the currents have already changed their sign, cancelling the previously flowing currents and once more the current flows only in one direction in each strip.

During the second quarter of the time period ($T/4$ to $T/2$), the shielding capability in the uncoupled and the coupled case is strongly reduced due to the backwards flowing intrinsic shielding currents.

AC scans at 50 mT

Again the intermediately long high resistive sample measured at 22 Hz is used to illustrate the weakly coupled case (figure B.23). The long coupled sample at 175.75 Hz represents the strongly coupled case (figure B.24).

Weak coupling

At $t = 0$, each strip has a field dome generated by trapped flux currents (figure B.23). Since the maximum applied field was about twice the penetration field, no minimum appears this time at the centre of each strip. Between $t = 0$ and $t=T/16$, the intrinsic shielding currents slightly increase, indicating that the maximum applied field was slightly below twice the penetration field ($2B_p=52$ mT from the Γ -plots). The maximum shielding is reached somewhere around $T/16$. For higher fields, the field dependence of I_c and the n - value reduce the currents in each strip. Similar to the intermediate field case (26 mT), the gradient of the current decreases from the inner and outer edges of the superconducting strips up to $T/4$.

After $T/4$, the currents at the edges are reversed. Due to the low I_c , the gradient of the field is much smaller than at 26 mT. Therefore, the backwards flowing currents are not visible

B Coupling losses in different geometries

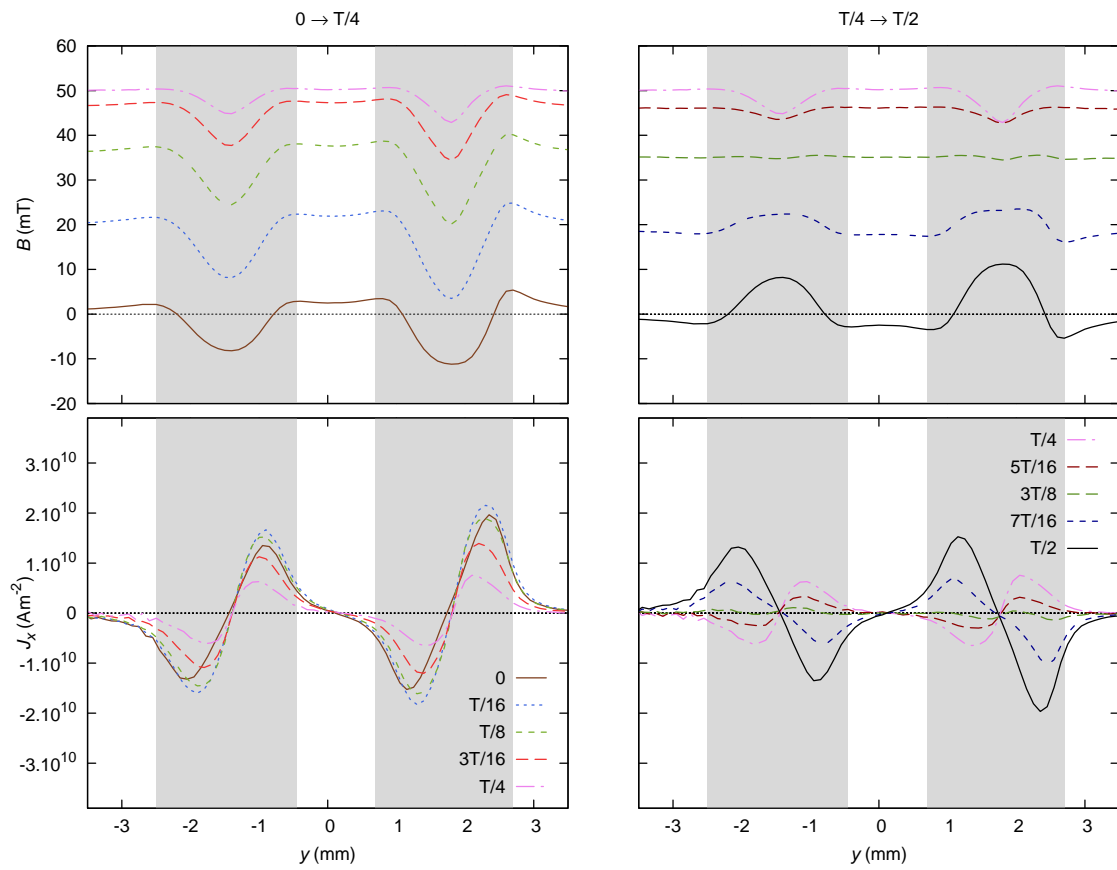


Figure B.23: High field behaviour of the intermediately long high resistive sample at 22 Hz.

B Coupling losses in different geometries

until $3T/8$. At $3T/8$, the backwards flowing currents are generating two small field domes inside each superconductor. After $3T/8$, I_c reaches higher values and the backwards flowing currents start to dominate and shield the superconducting strips. At $T/2$, only two oppositely flowing currents flow in each strip, leading to a maximum trapped flux in the superconductor at $T/2$.

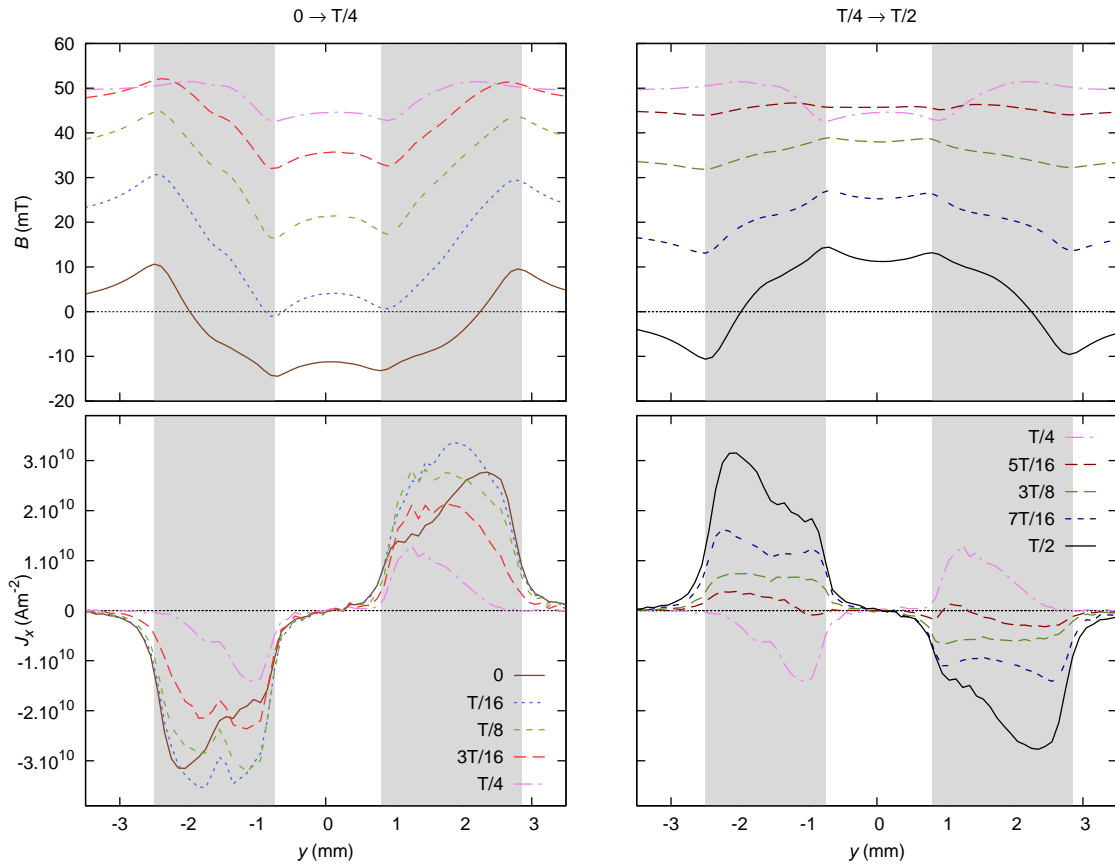


Figure B.24: High field behaviour of the long coupled sample at 175.75 Hz.

Strong coupling

Similar to the intermediate field case (26 mT), the currents flowing at $t = 0$ would be able to shield the whole sample, if a positive field would be applied (figure B.24). The coupling current is so strong that it reverses the oppositely flowing trapped flux currents (which generate the in phase field inside the gap in the uncoupled case). Thus, the resulting current flows only in one direction in each strip. Until $T/16$ the current increases and shields the whole sample. After $T/16$ the magnetic field dependence of I_c becomes important. Hence, the maximum of the current decreases and shifts towards the gap.

B Coupling losses in different geometries

After $T/4$ the backwards flowing currents become visible at $5T/16$. Compared with the weakly coupled case at $3T/8$, one can see that the coupling current has already changed the direction indicated by a phase $\varphi < 45^\circ$. Furthermore, the coupling current is strong enough to drive the currents in one direction most of the time. At $T/2$, the coupling current supports the trapped flux current by generating a dome over the entire sample again.

Similar to the intermediate field case (26 mT), the shielding is strongly reduced in the second quarter of the time period. The effect is stronger at higher fields.

Frequency dependence

In order to evaluate the frequency dependence of the losses, at least half of the time period must be evaluated. Nevertheless, an initial estimate can be made by looking at the field distribution at $t = 0$ (or $t = T/2$). The induced voltage has a maximum and the trapped flux currents, which are largely independent of frequency, generate the same field at all frequencies. The frequency dependent coupling currents on the other hand will cause a difference in the frequency dependent field and current distributions. The higher the flux inside the gap (and therefore the coupling current), the higher the loss will be. This prediction will become inaccurate, when the coupling current does not behave sinusoidally, as at sufficiently high fields.

The frequency dependent fields for the long coupled sample at $T/2$ are shown in figure B.25 for a low (a) and a high field (b).

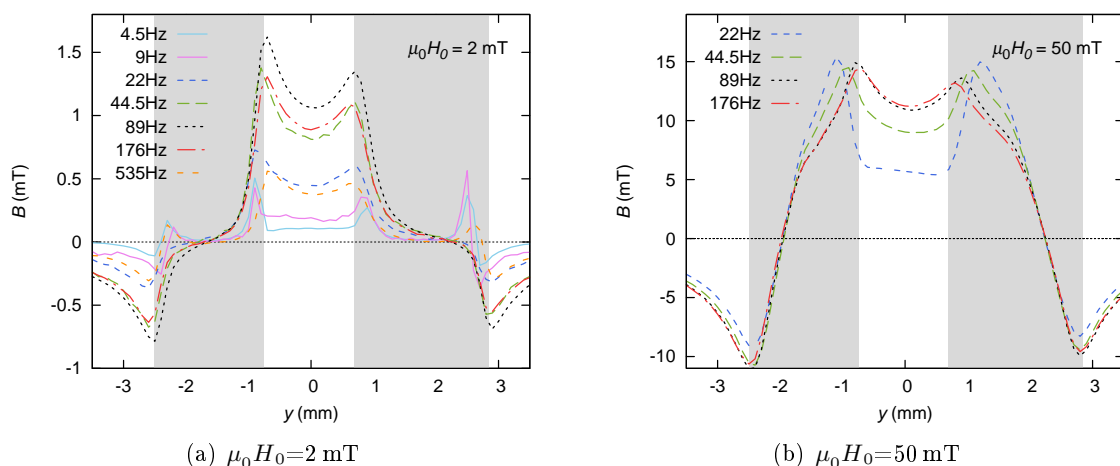


Figure B.25: Frequency dependence of the local field of the long coupled sample at $T/2$.

At 2 mT, the highest flux inside the gap occurs at 89 Hz, corresponding to the larger coupling current at $T/2$ (cf. figure B.11: 89 Hz and figure B.25(a)). The loss is also highest at this frequency (as will be confirmed in the section B.6).

B Coupling losses in different geometries

The frequency dependence is different at 50 mT. The maximum flux inside the gap is generated between 89 Hz and 175.75 Hz or even higher. In the low field regime, the critical frequency is shifted to higher frequencies due to the additional resistivity of the superconductor (the coupling currents are already higher than I_c).

In reality, the situation is much more complicated, due to the previously mentioned field dependence of I_c and the n – value in (B.10) at higher fields. Nevertheless, looking at the coupling current at higher fields, one also observes a frequency dependent phase shift and a frequency dependent loss. Handling this frequency dependence with a critical frequency (or time constant) is therefore practical, but one must be aware that the simplified picture from the low field regime is no longer valid. Note that this point has already been discussed within the high field model calculations.

Within the field range of the AC Hall scans, we were unable to entirely enter the previously discussed high field regime. Nevertheless, the decreasing frequency sensitivity shown in figure B.25(b) and the approximately rectangular current distribution at high fields (see figure B.24) indicate that such a regime exists.

In section B.6, the term “critical frequency” is used to explain frequency dependent losses even at higher fields, knowing that this will not describe all mechanisms.

B.5.2 Striated single Roebel strand

Magnetoscan measurements performed on the striated tape (see section C.9 on page 70) and TEM images [20] show a good separation between the filaments of the striated single Roebel strand. Hence, no frequency dependent changes of the local field and currents are expected. Figure B.26 shows the results of the scanning measurements at $t=T/2$. At first glance, the

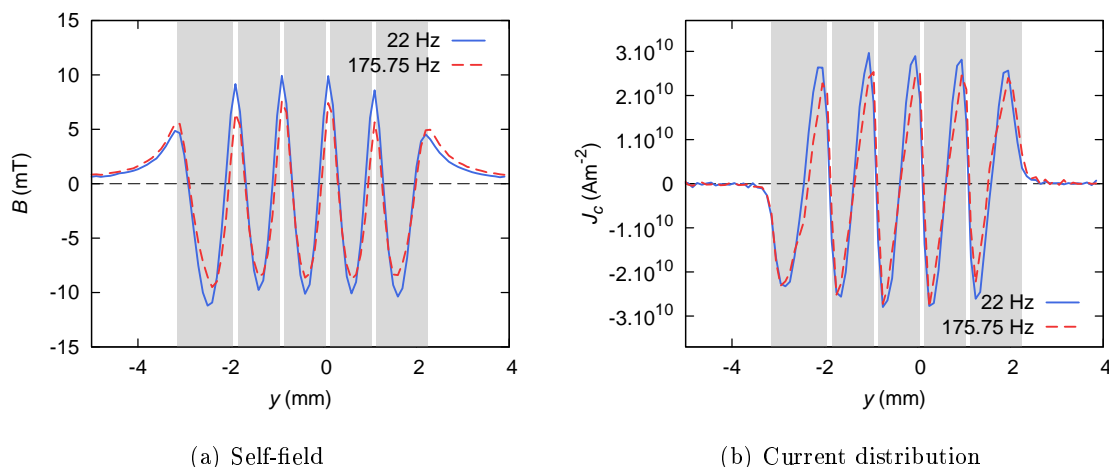


Figure B.26: Remanent field and current for $\mu_0 H_0 = 50$ mT.

maximum field is slightly lower at the inner filaments at 175.75 Hz. The evaluation of the net

B Coupling losses in different geometries

currents of each filament showed that a negative net current flows in the far left filament and a positive net current flows in the far right filament. Thus, four point measurements with low currents (100 mA) were performed between each filament in [37]. The measured resistivities were the smallest between the outer filaments, higher between one outer and one inner filament and highest between different inner filaments. The values did not change significantly within these three situations. Hence, coupling through the substrate, as illustrated in figure B.27, is suggested.

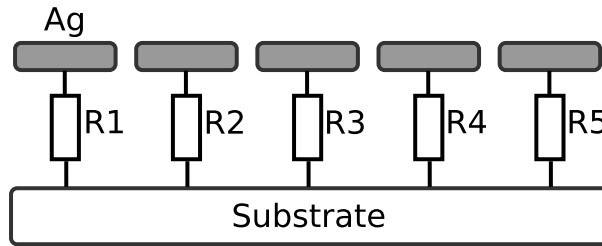


Figure B.27: Electric equivalent of the striated tape.

The outer filaments were found to be connected to the substrate with $R_1 = R_5 \approx 0.4 \text{ m}\Omega$ and the inner filaments with $R_2 = R_3 = R_4 \approx 4 \text{ m}\Omega$.

B.6 Results of the AC loss measurements by calibration free method (CFM)

In this section, the frequency dependent losses at the different coupled Roebel loops are discussed. Insulated and coupled samples of the same geometry are compared in order to investigate the influence of the coupling. In order to compare the loss for different sizes, the loss per unit length and cycle Q as defined in (B.33) was evaluated. In the following, Q will be denoted as the loss. The characteristic length l , as shown in figure B.1, was used as the length of the samples. Furthermore, the loss factor $\Gamma = Q/B^2$, gives a more intuitive picture of the coupling mechanisms.

The hysteresis losses of the insulated samples are almost the same at all fields and for all geometries. Only the short sample has a slightly higher loss due to the higher influence of the transverse part if one divides it by the length l . A slight increase of the hysteresis loss with frequency for all uncoupled samples was observed. This effect is described by [36] and is a result of the power law. At low fields, the coupling losses are dominant compared to the hysteresis losses. In general, the hysteresis losses are one order of magnitude lower than the coupling losses in our samples at very low fields (1-2 mT). The different loss mechanisms are clearly seen in the Γ -plots where the loss is normalised by the squared field. As expected [35],

B Coupling losses in different geometries

the hysteresis losses increase with B^4 below the penetration field B_p , whereas the coupling losses increase only proportional to B^2 (see (B.34)). Therefore, the loss factor Γ of the coupled sample remains constant ($\Gamma = Q/B^2$) until the hysteresis losses (indicated by the data of the insulated samples) reaches a magnitude comparable to the coupling losses. Between 26 mT and 28 mT, the field fully penetrates all samples. B_p can be identified by the peak in Γ -plots of the uncoupled samples. For higher fields, the hysteresis loss becomes proportional to B as expected from [35]. The coupling losses also become nearly proportional to B as expected from (B.44). The applied AC field was sinusoidal and B_0 refers to the amplitude of the applied field in this section.

Each sample will be discussed in detail below.

B.6.1 Short sample

Figure B.28 shows the frequency dependence at 2 mT. The critical frequency (f_c) at low fields is 334 Hz (cf. (B.36)). Since the critical frequency is higher than the maximum measured frequency, the loss increases with frequency. The solid line in figure B.28 represents the loss calculated from (B.34).

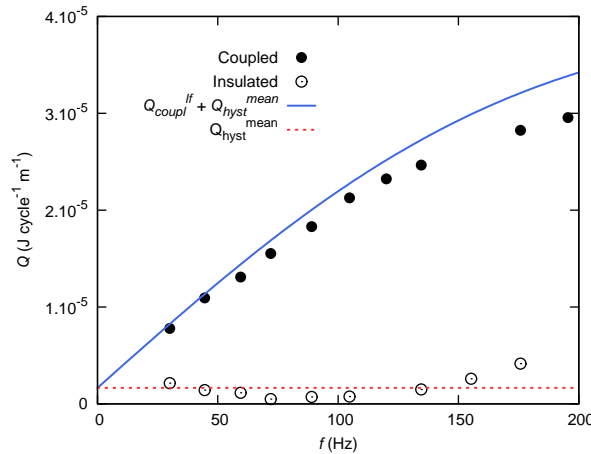


Figure B.28: Frequency dependent loss of the short samples at $B_0=2$ mT. The solid blue line represents (B.34) after addition of the fitted hysteresis loss Q_{hyst}^{mean} (dotted red line).

Figure B.29 shows the loss and the loss factor for all measured fields and various frequencies.

The initial slope of the coupled sample losses at low fields (1-3 mT) is similar at all frequencies, as the low hysteresis losses do not contribute (see figure B.29). Furthermore, the loss increases with frequency similar to the frequency dependence at 2 mT (see figure B.28).

B Coupling losses in different geometries

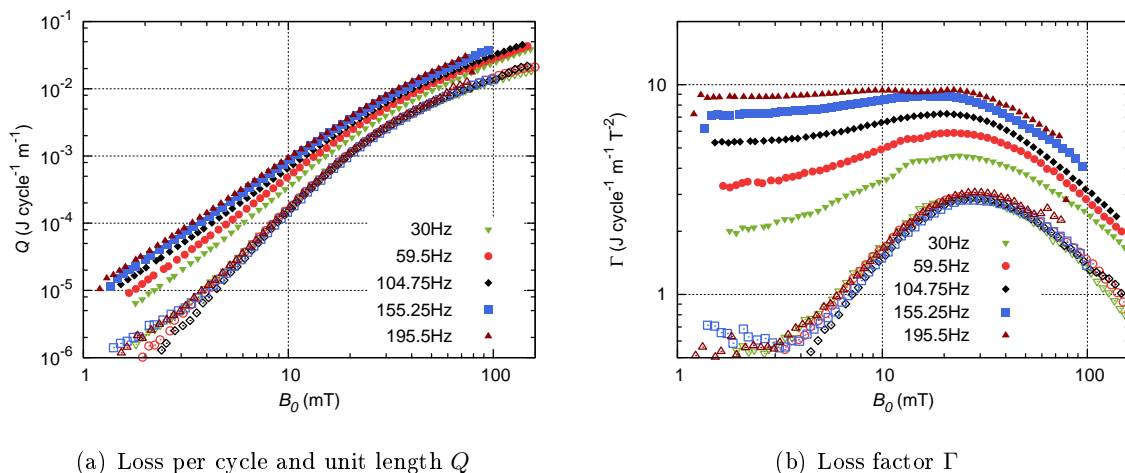


Figure B.29: Loss/length and loss-factor CFM-measurement of the short samples. Solid symbols refer to the coupled sample and open symbols refer to the insulated sample.

With increasing field, the hysteresis losses increase more than the coupling losses and increasingly influence the frequency dependence of the loss. The strands are fully penetrated by an applied field of ≈ 26 mT. For higher fields, the coupling current is still smaller than I_c in the small sample. Therefore, the inductance remains a crucial value in (B.10), leading to a strong frequency dependence even at higher fields. Nevertheless, the loss of the coupled sample becomes proportional to B for fields above B_p , as found in the high field model. Note that the intrinsic shielding currents already flow with I_c for $B_0 > B_p$.

B.6.2 Intermediately long samples

In the low field regime, the loss further increases monotonously with the frequency in the measured range (figure B.30). The critical frequencies of the samples are calculated to be 212 Hz and 502 Hz for the low resistive and the high resistive sample, respectively. Once again, the solid and the dashed line represent the calculated loss. The high resistive sample was also characterized by AC Hall-scans. Thus, the calculated losses from the scans according to (B.7) are indicated in figure B.30 by red triangles as well. The higher resistive connections lead to a higher critical frequency and therefore to a different frequency dependence of the loss.

Figure B.31 shows the loss in the low resistive sample in the entire field range. The strands are again fully penetrated at about 26 mT. At higher fields, the frequency dependence becomes less pronounced once the coupling currents reach I_c and therefore the resistivity of the superconductor becomes more important for the coupling losses. At the highest fields, the loss in the coupled sample is ≈ 2.5 times higher than the loss in the uncoupled samples. This

B Coupling losses in different geometries

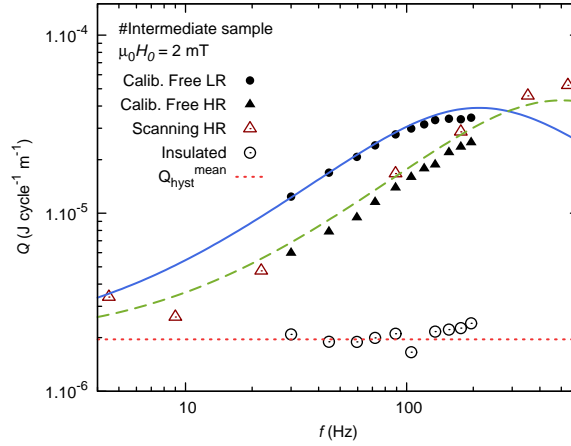
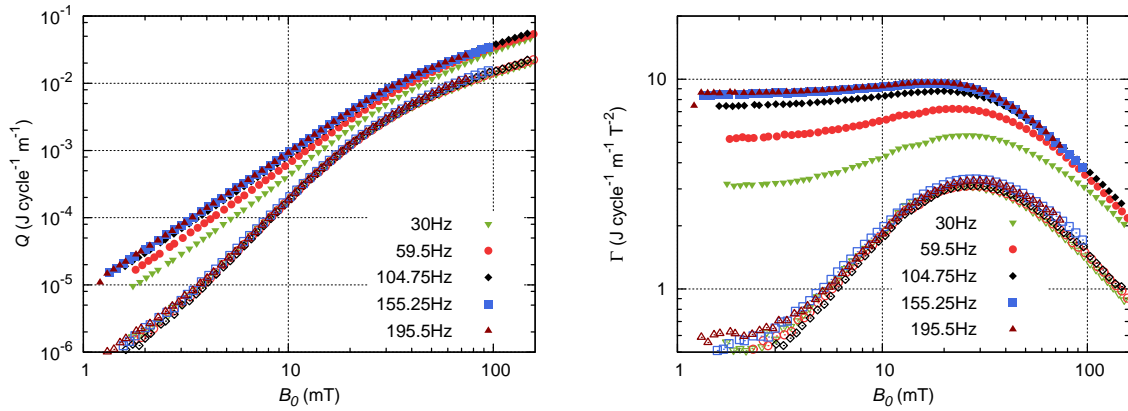


Figure B.30: Frequency dependent loss at 2mT. The blue solid and the green dashed line represent (B.34) for the low resistive and the high resistive sample, with Q_{hyst}^{mean} added. The full circles and triangles correspond to the CFM measurements whereas the red open triangles to the loss measurements with the AC Hall-scan.

is beyond the upper loss limit of 2.89 calculated from (B.48). The loss of the high resistive



(a) Loss per cycle and unit length Q

(b) Loss factor Γ

Figure B.31: Loss/length and loss-factor CFM-measurement of the intermediately long low resistive samples. Solid symbols refer to the coupled sample and open symbols to the insulated sample.

sample, shown in figure B.32, never enters the high field regime, as the coupling current is restricted by the higher connection resistivity. For higher fields, the frequency dependence is therefore the same as in low fields, because of the negligible influence of the power law on the coupling currents. The loss in the coupled sample at the highest frequency is ≈ 3 times higher than the hysteresis loss. Once again, this value is slightly below the calculated upper loss limit of 3.17.

B Coupling losses in different geometries

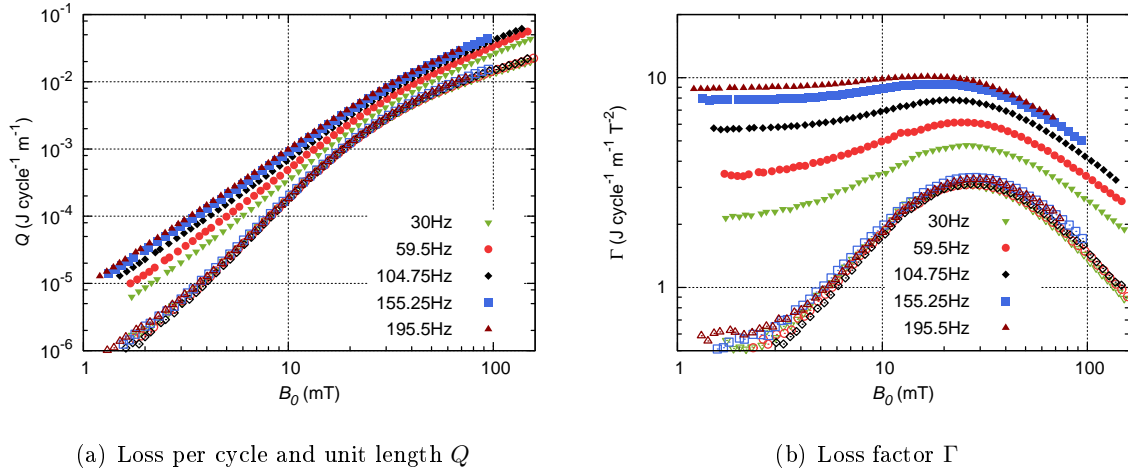


Figure B.32: Loss/length and loss-factor CFM-measurement of the intermediately long high resistive samples. Solid symbols refer to the coupled sample and open symbols to the insulated sample.

B.6.3 Long sample

At 2 mT, the loss peak appears at the critical frequency (figure B.33(a)). The loss first increases with frequency up to about 90 Hz before the loss decreases again. The calculated critical frequency is 95 Hz. Once more, the loss evaluated from the AC Hall scan is in close agreement with results obtained from the calibration-free method.

Contrary to low fields, the loss increases with frequency and no maximum is observed at the higher field of 50 mT. The high field assumption ($B \gg B_p$) is not fulfilled at this field. Nevertheless, the magnitude of the calculated loss (blue line) is in close agreement with the measurements, whereas the frequency dependence is not as pronounced as in the measurement. The results from the AC Hall scan underestimate the loss. Since the eddy currents of the copper bridges are not considered in the AC Hall scan evaluation, this could explain the slightly smaller losses. Furthermore, the calculated loss assuming a constant J_c according to (B.45) is illustrated.

Figure B.34 shows the frequency and field dependent losses obtained from the CFM. Due to the large area, the induced voltage is the highest in this sample. Therefore, the long sample shows the best indication of reaching the high field regime. For fields slightly above B_p , the “resistivity” of the superconductor becomes dominant. At about 20 mT, the frequency dependence changes (see B.34(b)). Because of the shift of the critical frequency to higher values, the loss increases monotonously with increasing frequency at higher fields, as previously shown in figure B.33(b). The loss of the coupled sample at the highest measured fields is about 3.4 times higher than the hysteresis losses. This value is slightly above the calculated upper limit of 3.29. The slight excess of the real loss compared to the calculated upper limit could

B Coupling losses in different geometries

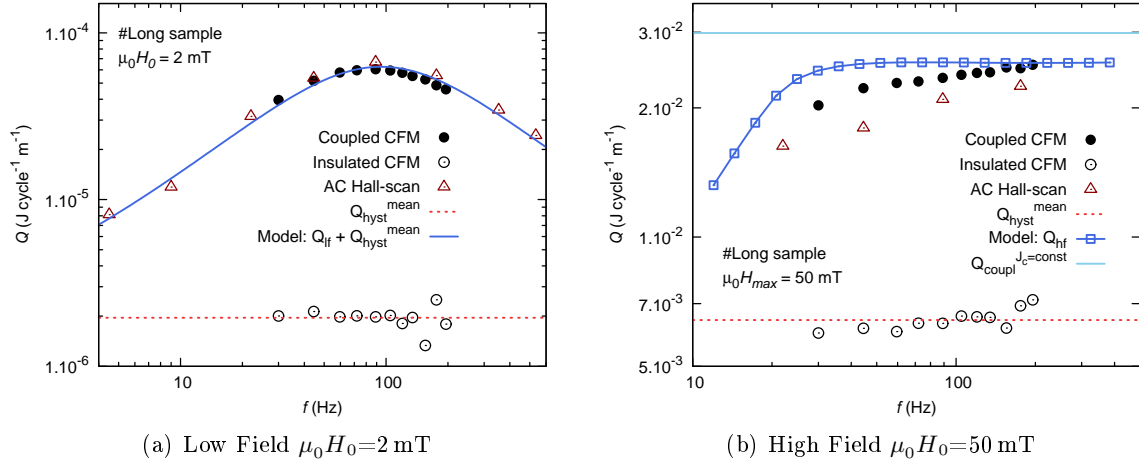


Figure B.33: Frequency dependant loss of the long coupled sample. The solid lines refer to the calculations from the (a) low field model and the (b) high field model, whereas the cyan solid line represents the coupling loss calculation with a constant J_c according to (B.45). The blue line with rectangular points represents the numerical calculation according to (B.44). J_c in (B.45) was taken from J_0 in (B.49).

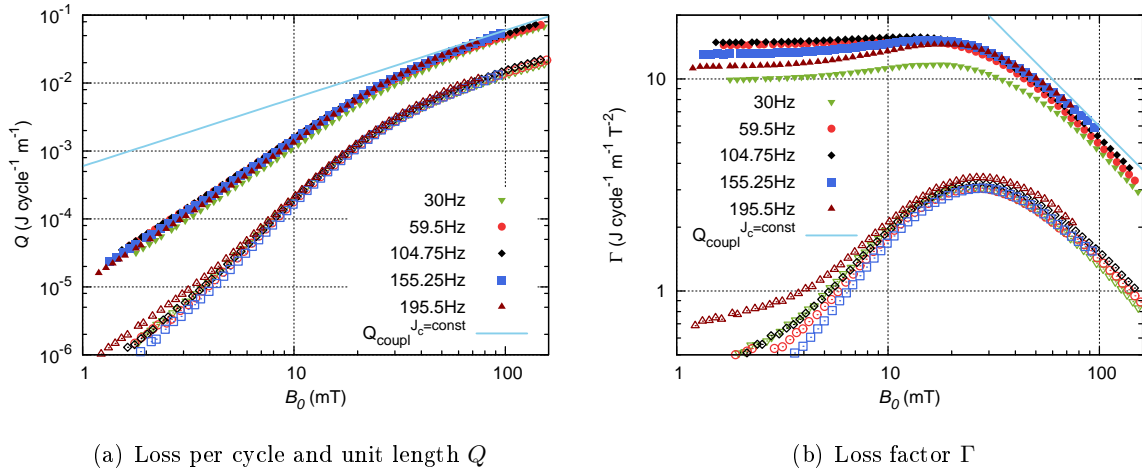


Figure B.34: Loss/length and loss-factor CFM-measurement of the long samples. Solid symbols refer to the coupled sample and open symbols to the insulated sample. The cyan solid line represents the coupling loss calculation with a constant J_c according to (B.45), where J_c was taken from J_0 in (B.49).

B Coupling losses in different geometries

be caused by the slightly larger width of the strand of the coupled sample (2.1 mm) compared to the insulated sample (2.05 mm).

The hysteresis loops for a maximum applied field of $\mu_0 H_0 = 2$ mT and $\mu_0 H_0 = 50$ mT are shown in figure B.35. The maximum magnetic moment per unit length increases with fre-

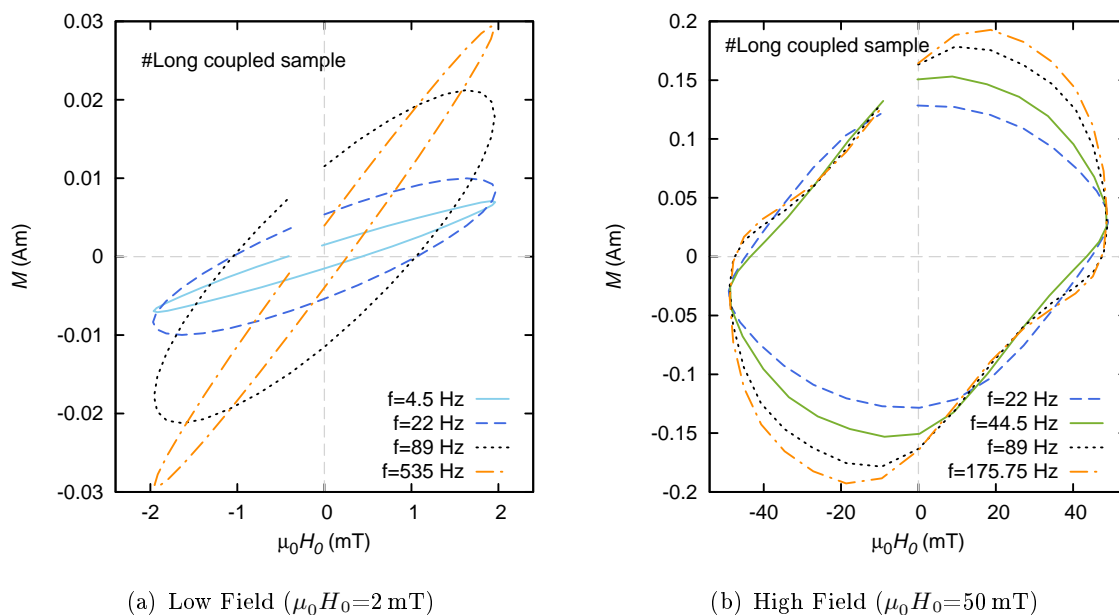


Figure B.35: Hysteresis loop of the long coupled sample obtained from AC Hall scans.

quency for $\mu_0 H_0 = 2$ mT. Nevertheless, the area of the hysteresis loop, and therefore the loss, is the highest at 89 Hz, due to the phase shift of 45° of the coupling current. Since the applied field is smaller than the penetration field, the magnetic moment does not saturate.

For $\mu_0 H_0 = 50$ mT, the magnetic moment and the loss increase with frequency. A saturation of the magnetic moment is expected at the penetration field (≈ 20 mT), if the critical current were independent of the applied field. In fact, the magnetic moment per unit length decreases significantly due to the field dependence of I_c above the penetration field. Note that the coupling current causing the magnetic moment per unit length is higher than the critical current $I_c(B)$.

Figure B.36 shows the time dependence of the loss evaluated from the AC Hall scans. Contrary to the calculated coupling losses for low fields in figure B.11, the AC Hall scan measurements represent the entire losses (coupling and hysteresis losses). Nevertheless, as the hysteresis losses are at least by one order of magnitude smaller at frequencies between 20 Hz and 550 Hz (see figure B.33(a)), the measurements for $\mu_0 H_0 = 2$ mT represent especially the coupling losses. One also finds close agreement between the time dependent measurements and the calculations (see figure B.11). The magnitude is only higher at 4.5 Hz. On the other hand,

B Coupling losses in different geometries

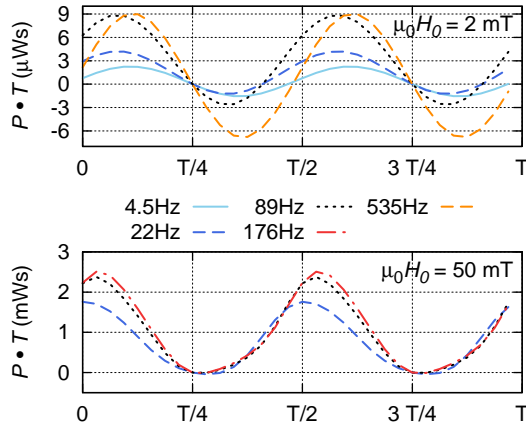


Figure B.36: Time dependent power of the long coupled sample obtained from AC Hall scans. $\mu_0 H_0 = 2$ mT (top) and $\mu_0 H_0 = 50$ mT (bottom).

the integral over the time period and therefore the loss Q is in very close agreement with the calculation, as shown in figure B.33(a). With increasing frequency, the reactive loss also increases, as indicated by the negative values. At 535 Hz, the reactive loss dominates.

At high fields the power law of the superconductor already plays a dominant role in the measured frequency range up to 176 Hz. The time dependent loss is in most cases of an “ohmic” nature. The coupling losses are about three times higher than the hysteresis losses of the insulated strands (see figure B.33(b)) at these frequencies.

B.7 Prospects for coupled Roebel cables and conclusion

The problems discussed in this chapter will not occur “one to one” in an assembled Roebel cable. Nevertheless, they help to explain cable coupling mechanisms. The following section will describe the coupling losses in an assembled cable based on our knowledge from the previous sections. Coupling is only considered between neighbouring strands. Figure B.37 shows the stepwise assembly of a five strand Roebel cable. In a two strand Roebel cable (figure B.37(a)), the coupling losses of a twist pitch are identified by two Roebel loops. Due to the twisted structure of the Roebel cable, the coupling currents in one strand flow oppositely in neighbouring loops. In strand 1 (red current), the current flows to the left in the left loop and to the right in the right loop. Hence, no net coupling currents flow over the entire length of the cable.

Using a third strand (figure B.37(b)) does not change much. Strand 2 (green) and strand 3 (blue) are able to form coupled loops as well as strand 1 (red) and strand 2 (green). Since strand 2 is in between the two other strands, it does not form additional loops even with more assembled strands. Yet again, neighbouring currents flow oppositely and therefore the net

B Coupling losses in different geometries

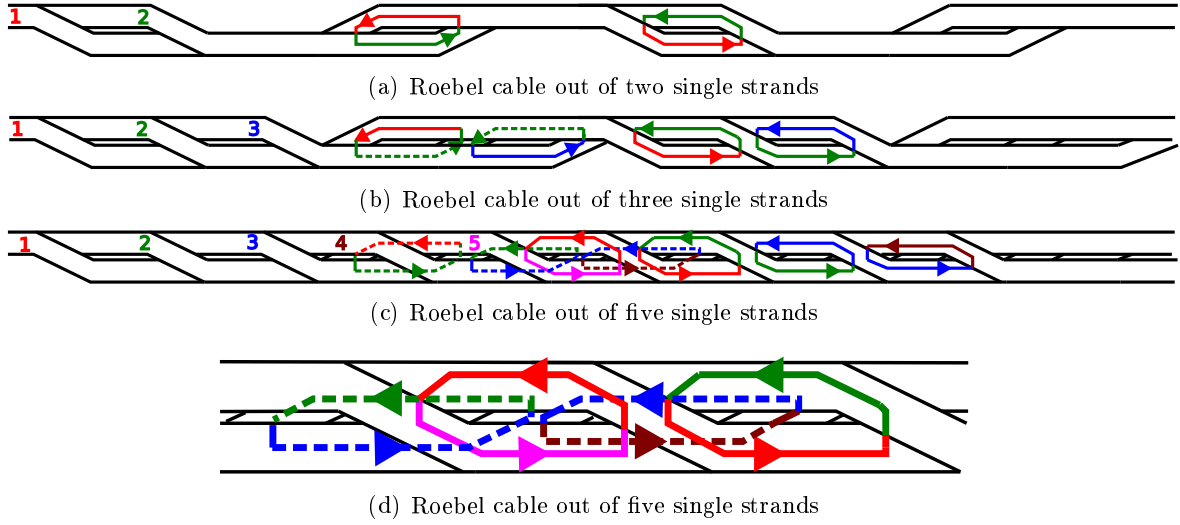


Figure B.37: Coupling currents in a five strand Roebel cable. Dashed lines indicates currents flowing not on the top strand. The colour code of the currents denotes the strand in which the current is flowing. (red) strand 1, (green) strand 2, (blue) strand 3, (brown) strand 4, (violet) strand 5

current from left to the right is zero. In low fields, the strands without local coupling currents (i.e. strand 3 above strand 2 (green dashed line) in the outer most left coloured loop in figure B.37(b)) will shield the strip with intrinsic shielding currents and therefore a slight influence of such sections is expected. Nevertheless, the influence of the small intrinsic currents should be small when compared with the coupling currents at low fields. Hence, the loss is about four times the loss of the single loops in one twist pitch.

At high fields, where full penetration of the field is expected, the closed loops dominate and therefore the loss per twist pitch should be deduced again from the four single coupled loops.

The situation changes drastically if a fourth and a fifth strand are assembled. Here, the transverse parts are below the gap enclosed by the coupling currents. Figure B.37(d) shows the most dense situation. For low fields, the transverse parts will partially shield the field inside the gap and therefore will interact with the flux focusing effect. If the field is low compared to the penetration field, the flux might be expelled from the gap, if the transverse part covers the whole area. Hence, no coupling currents can be induced and therefore no coupling losses will occur.

The situation is different if the transverse part does not entirely fill the space of the closed loop (see figure C.1 on page 65). Here, the flux shielded by the transverse part shifts inside a Roebel loop and the situation is similar to the two-strand Roebel loop. Therefore, a frequency dependent loss occurs. Furthermore, due to the combination of different loops which shield the same area, the interplay between the single Roebel loops has to be considered.

B Coupling losses in different geometries

In the high field regime, the intrinsic shielding would have no effect. As two current loops shield the same area, they have to interact somehow. In the five strand Roebel cable, there are always top loops and bottom loops, as indicated by the dashed and the solid lines in figure B.37(d).

Note also that the penetration field depends mainly on I_c . Therefore, the low field case would allow much higher fields at lower temperatures. At 4.2 K the critical current density of a coated conductor is about $2 \cdot 10^{11} \text{ Am}^{-2}$. Hence, the penetration field of the Roebel loops would be about 200 mT.

However, the situation in a fully assembled Roebel cable is somehow related to the single Roebel loops, due to the complete transposition of the strands and the oppositely flowing coupling currents in a single strand.

In the low field regime, the width of the tapes play a crucial role, since the effective area in A_{lf} in (B.27) depends on them and A_{lf} is squared in (B.34).

The situation is similar at high fields. Again the width of the tape appears squared in the loss calculations in (B.44) ($A_{hf} w$).

The use of small filaments and the reduction of the gap width and length should decrease the coupling losses in the Roebel cable. These conditions are in good agreement with the methods used in the CICC cables to reduce the AC losses. However, in thin film loops the local field at the inner edge will be significantly enhanced due to the flux focusing effect in a narrow gap. Therefore, the field penetrates from the inner edges and a kind of effective gap width will occur. This gap width depends mainly on the applied field and I_c of the strands. In other words, the reduction of the geometrical gap width, is limited by this effective gap width.

C Homogeneity, current- and field-distribution in single Roebel strands

The main aim of this chapter is to take a closer look at the homogeneity of different Roebel strands (see also [42]). Assembly and preparation techniques as well as defects in the underlying coated conductor material influence the quality of the Roebel strands.

Two different techniques were used to characterise the homogeneity of the samples: the contact free magnetoscan technique [43] and a method to measure the local self-field of the tape under current flow. With an inversion algorithm [44], the local current flow was visualised. From the latter method, the field and current penetration in single Roebel strands could be evaluated and will be discussed in sections C.3.2 and C.3.3.

C.1 Samples

Two different Roebel strands ($w=2$ mm and $w=5.5$ mm) were used. Two 5.5 mm wide samples were provided by the Karlsruhe Institute of Technology (KIT). One of these tapes was striated and already discussed in the previous chapter. A detailed description of the striated tape can be found in section B.1.2 and in [20]. Both KIT strands were punched from SuperPower 2G-HTS-SP12050 YBCO coated conductors. This tape does not have a copper stabiliser on the silver layer. Due to the absence of a stabilisation layer, the IV-curve of the sample was only measured up to a $0.4 \mu\text{V}/\text{cm}$ criterion. Extrapolating the data by the power law $E = E_c (I/I_c)^n$ with $E_c = 1 \mu\text{V}/\text{cm}$ results in a critical current of 134.1 A. The n – value was 31 and the distance between the voltage contacts was 110 mm. The width of the tape varies from 5.35 mm to 5.5 mm between the voltage contacts.

The 2 mm wide sample, provided by Industrial Research Limited (IRL), is a single strand taken out of a 5/2 (5 strands, 2 mm width) Roebel cable. It was made of a SuperPower 2G-HTS-SCS12050 YBCO coated conductor. This tape is coated with a $20 \mu\text{m}$ copper stabiliser on both sides. The cable manufacturing process is described elsewhere [19]. The end-to-end critical current of the single strand evaluated at a $1 \mu\text{V}/\text{cm}$ criterion is 35.9 A and the n – value is 22. The width of the tape varies between 1.68 mm and 1.93 mm. The distance between the outer voltage contacts was 72 mm. The distances of the voltage contacts on the crossover part, the left straight and the right straight part were 4.2 mm, 4.0 mm and 4.6 mm, respectively.

C Homogeneity of Roebel single strands

Figure C.1 shows an assembled cable made from the 2 mm sample.



Figure C.1: IRL 5/2 Roebel cable

C.2 Experimental details and evaluation

C.2.1 Magnetoscan measurements

With the magnetoscan technique developed at the Atominstitut [43], a very fast and accurate characterisation of long-length coated conductors is possible. Figure C.2 shows a schematic view of the set-up. The whole part is immersed in liquid nitrogen and has therefore a temper-

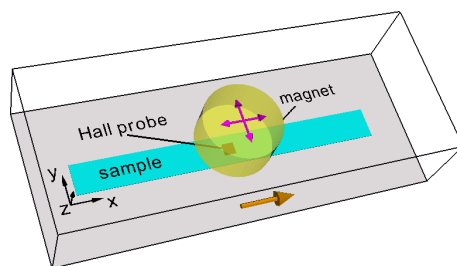


Figure C.2: Sketch of the magnetoscan set-up taken from [45]

ature of 77K. A cylindrical magnet with a height and diameter of 5 mm is mounted 7.5 mm above a coated conductor corresponding to an applied field of about 50 mT at the sample surface (yellow cylinder in figure C.2). A Hall probe is assembled in a stainless steel scaffold below the magnet ≈ 0.2 mm above the sample. The Hall probe measures the local magnetic field in z -direction caused by the induced super-currents and the applied field. As shown in [45], the detected local field $B_z(x, y)$ is closely related to the local critical current density $J_{xy}(x, y)$ and therefore provides evidence for the local quality of the coated conductor. Scanning the whole sample in x - and y -directions at a fixed z -position gives a descriptive picture of the homogeneity of the tape. The spatial resolution of the Hall map is typically 0.2 mm in x - and y -directions. Figure C.3 shows the whole set-up with further details. The Hall probe is fed by a standard current source with 10 mA and the Hall voltage is measured with a Keithley 2700 multimeter. The multimeter and the xyz -table are controlled by a PC using a home-written software.

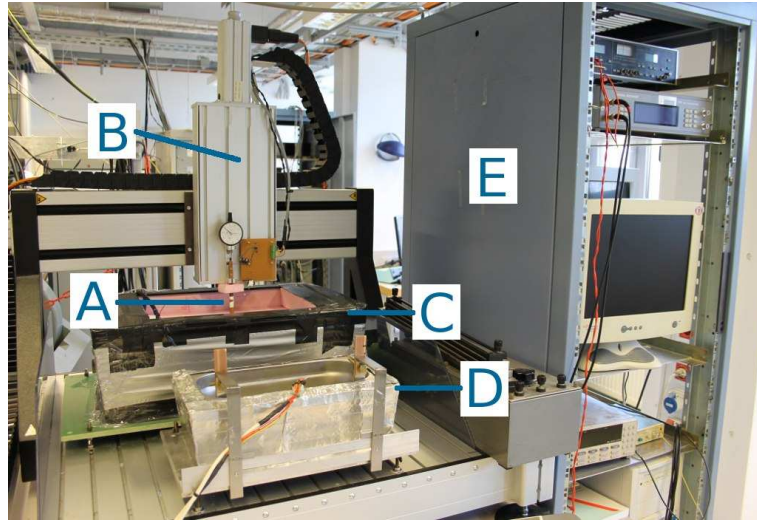


Figure C.3: Scanning set-up. (A) Rod with the Hall probe at lower end, (B) xyz-table, (C) large dewar with an AC coil inside, (D) small dewar for magnetoscan and Hall scan measurements under current flow, (E) measuring equipment and PC.

C.2.2 Hall-scan measurements under current flow

Figure C.4 shows the self-field scan set-up and the coordinate system used.

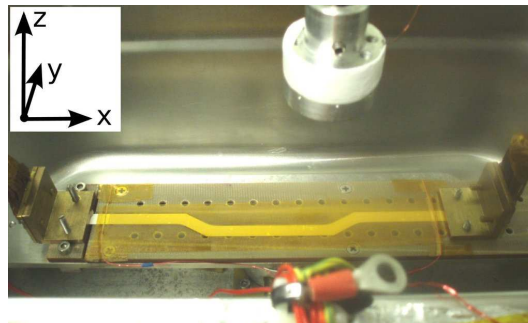


Figure C.4: Set-up for measuring the self-field of a coated conductor and coordinate system. The single strand was fixed on the left and right side with the current connectors as well as with Kapton tape. The left current connector can move in x -direction to provide stress free cooling. After cool down, the connector was fixed by two screws.

The Hall-scan set-up is similar to the magnetoscan set-up without a permanent magnet. The Hall-sensor again detects the field component perpendicular to the sample surface (B_z). In order to measure the self-field of coated conductors under current flow, the conductor is connected to cables of a 300 A current source via pressed indium contacts. Voltage contacts

C Homogeneity of Roebel single strands

were made with silver paste. The PC shuts down the current source, when the detected voltage on the sample exceeds a critical value. Critical transport currents were also measured with these voltage contacts. The sample was always immersed in liquid nitrogen during the measurements. Therefore, the temperature was stable at around 77 K. The 5 mm wide sample was fixed with Kapton tape and the Hall-probe holder was moved in the x - y plane in contact with the Kapton tape. Hence, the distance between Hall-sensor and superconductor was constant at about 150 μm . The 2 mm sample was scanned with the Hall-probe holder at about 50 to 80 μm above the conductor.

The calculations of the local current density distribution in two dimensions (J_x, J_y) from the Hall-map were done by a computer algorithm for the inversion of the Biot-Savart law [44]. This algorithm was programmed for samples in the remanent state with no currents flowing outside the scan area and does not allow current sinks or sources at the boundaries. The currents flowing into and out of the scan area lead to artefacts, i.e. currents flowing near the boundaries of the map (not shown in figure C.12), closing the postulated current loops. However, these artificial currents rapidly decay towards the centre of the matrix. Nevertheless, this problem will have to be solved in the future.

C.3 Results and discussion

Unlike a few years ago, state-of-the-art long-length coated conductors show very smooth magnetoscan images in accordance with homogeneous conductors. Therefore, the homogeneity of pristine coated conductors will not be discussed in this chapter. Nevertheless, a magnetoscan image of a 4 mm SuperPower SCS4050 tape similar to the 12 mm SuperPower SCS12050 tape used for the Roebel strand samples in this chapter is shown in Figure D.31(a) on page 116. Due to punching processes or mechanical treatment during the fabrication of Roebel strands, the superconducting layer can be locally destroyed. Local inhomogeneities were detected by short-length four-point measurements, magnetoscans and Hall scans under current flow. As the last method gives additional information about the physics in the Roebel strand, it is discussed in more detail in C.3.2 and C.3.3.

C.3.1 Homogeneity

IRL - 2 mm strand

A Roebel single strand from the 5/2 (5 strands, 2 mm width) Roebel cable was used for the characterisation. The width of the conductor varied from 1.77 mm to 2.17 mm, as shown in figure C.5. Note that the regions labeled A-E in figure C.5 also mark the regions where transport measurements were performed.

From the different geometrical cross-sections (different widths), one expects that the critical

C Homogeneity of Roebel single strands

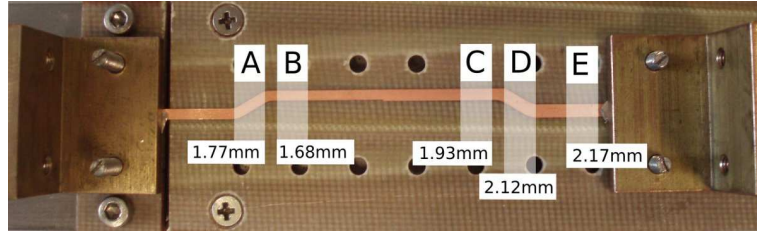


Figure C.5: Variation of the width of the single strand

current in the left parallel section should be significantly lower than that of the right parallel section of the single strand. This was confirmed by the magnetoscan and the transport measurements. The magnetoscan images (figure C.6 and C.7(a)) indicate the lower I_c by the lower field signal on the left side.

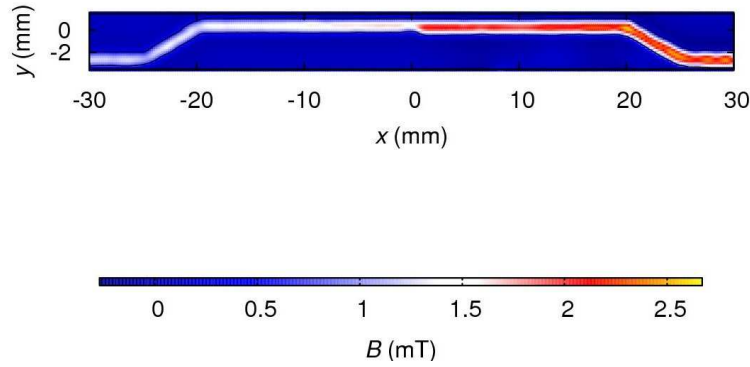


Figure C.6: Magnetoscan of the entire sample

The results of the critical currents obtained by transport measurements in the regions B and C show a degradation of I_c by 15%, whereas the critical current density remains unchanged (see also figure C.8). On the left and the right side of the geometrical reduction, the tape looks homogeneous, as shown in figure C.7(a). No larger defects were located in this region. The current calculations from the Hall-scan (figure C.15(b)) show the bottleneck in the parallel section in more detail. The current density is significantly larger on the left side, due to the reduction of the geometrical cross section.

Comparisons between the magnetoscan profiles of the left transverse and the parallel section (figure C.7(b)) indicate a defect in the left corner. The local current calculations from the self-field confirm the magnetoscan measurements (figure C.15(a)). Furthermore, they show that the defect is located at the upper edge of the left corner. The current has to bypass the defect on the lower side and therefore the current density increases close to the outer left corner of the tape. This defect is also the limit for the overall critical current.

C Homogeneity of Roebel single strands

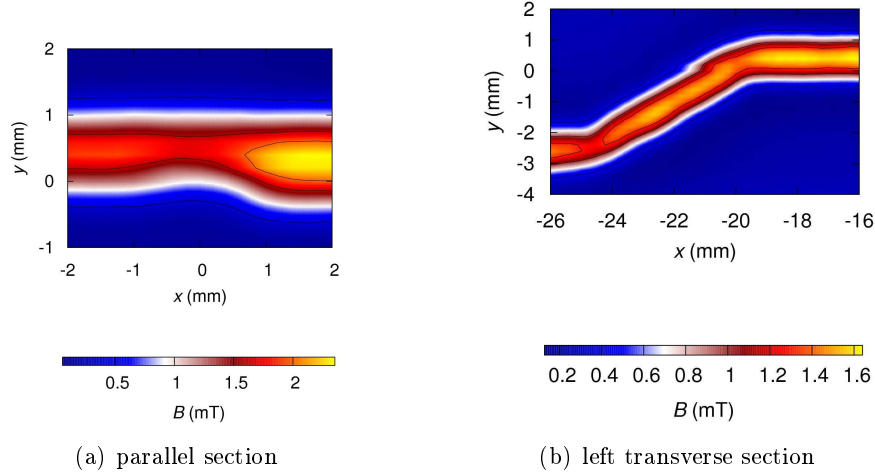


Figure C.7: Magnetoscan of the IRL 2 mm tape

Magnetoscan and local current calculations indicate that the critical current or the current density do not depend on the direction. Four-point measurements in region A and B confirm these results.

The overall critical current was found to be 35.9 A. This is equivalent to 82% of the maximum critical current in region C (43.7 A).

Geometrical effects based on the manufacturing process are the major reason for the change of the critical current along the length of the sample. The difference in the cross-section leads to a degradation of the critical current by 15%, while the defect at the inner-left corner influences I_c only by additional 3%. The degradation over the entire sample is therefore 18%. A variation between the current density in the parallel and the transverse section was not observed. Striation of this particular strand would lead to a further decrease of I_c . The currents would not be able to bypass the defects within the superconductor, especially in the transverse section. Striation requires an overall improvement of the homogeneity. In this particular strand, the defects are more pronounced in the transverse section.

KIT - striated 5.5 mm strand

Magnetoscan images of the striated Roebel strand show a clear separation of the superconducting layers between each filament. Nevertheless, an defect in the pristine tape seems to be responsible for a reduction of the local J_c at $x=40$ mm and $y=3$ mm in figure C.9. Currents are unable to flow around this defect, due to the striation. Hence, this local inhomogeneity is a weak spot in the strand.

C Homogeneity of Roebel single strands

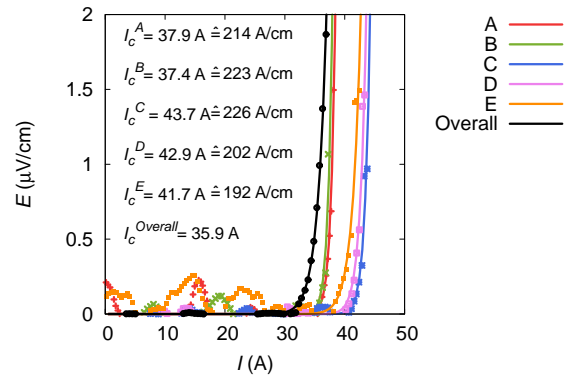


Figure C.8: Transport measurements on a single strand. Regions A-E refer to the positions shown in figure C.5

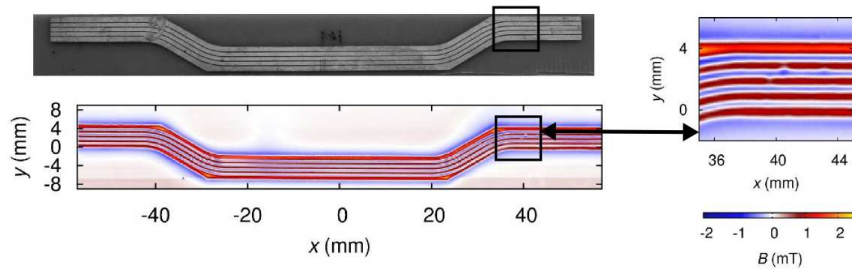
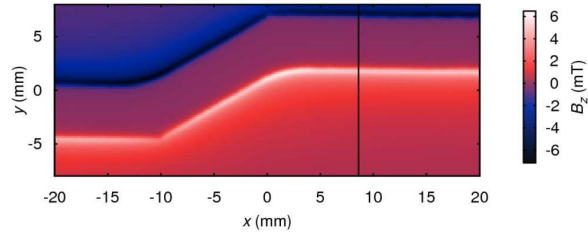


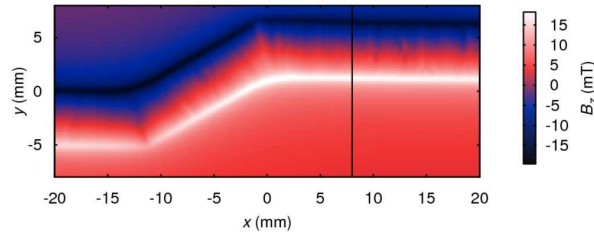
Figure C.9: Striated Roebel strand from KIT

C.3.2 Field distribution

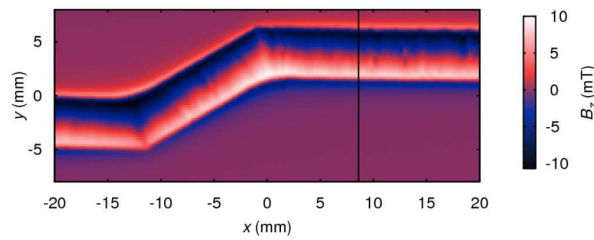
The 5 mm wide sample was scanned under currents of 30 A, 60 A, 90 A and 120 A (0.22, 0.45, 0.67 and 0.89 times I_c) as well as in the remanent state after shutting down the current source. Figures C.10(a)-C.10(c) show the field maps at 30 A, 120 A and in the remanent state. The



(a) 30A



(b) 120A



(c) 0A (remanent)

Figure C.10: Field penetration for different currents. The vertical lines mark the position of the field profile at $x=8.6$ mm shown in figure C.11

field profiles of the straight part are plotted for all measured currents in Figure C.11.

The field penetrates with increasing current from the edges to the middle of the sample. Note that the field in y - direction $|B_y|$ is not detected in our measurements. With decreasing current, the field changes at the edges, whereas the pinned field in the centre remains constant. This behaviour is well described by the critical state theory for thin films [35][46]. The same

C Homogeneity of Roebel single strands

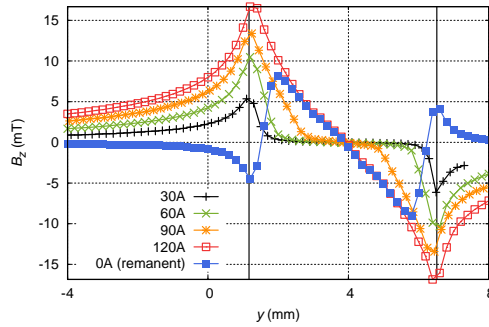


Figure C.11: Field distribution at $x=8.6$ mm. The solid vertical lines mark the edges of the sample.

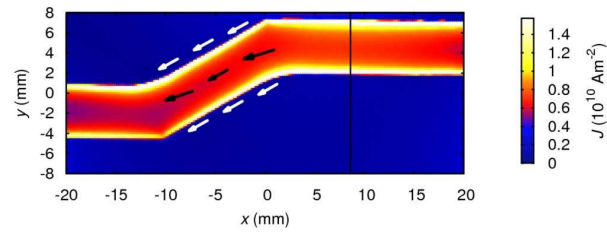
effects take place in the crossover section, but also an enhancement of the field at the inner corners and a corresponding reduction at the outer corners. This geometrical effect was confirmed by simulating a homogeneous current distribution flowing along the Roebel strand.

C.3.3 Current distribution calculated from the field distribution

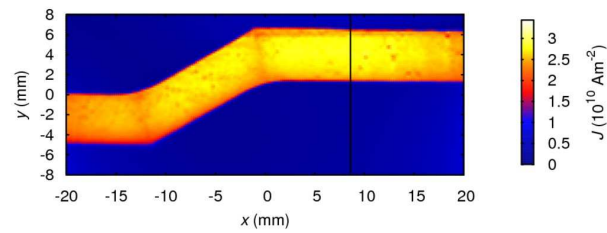
Figures C.12(a)-C.12(c) show the calculated current distributions for different applied currents. The current starts to penetrate from the edges and surfaces. In the following, currents penetrating from the edge are denoted as edge currents, and currents penetrating from the top and bottom surfaces are denoted as surface-currents. In infinitely thin films, the self-field produces a discontinuity of B_y between by top and bottom surface. Therefore, a (sub-critical) current is also flowing in the middle of the sample close to the surfaces from the beginning [35][46]. At 30 A (Figure C.12(a)) the main part of the current is flowing along the edges of the sample. The edge-currents flow parallel to the edges in the straight part. In the crossover section the surface-currents change their direction later than the edge currents leading to a non parallel configuration between edge- and surface-currents as indicated by the arrows in Figure C.12(a). Close to I_c (Figure C.12(b)) the current is nearly homogeneously distributed over the cross-section and therefore flows parallel to the edges. The actual width of the tape is 5.5 mm on the left straight section, 5.4 mm on the crossover section and 5.35 mm on the right straight section. The current density in the crossover and the straight right section is nearly the same. On the left straight part, the current density is slightly lower than on the right straight part due to the larger geometrical cross section. Between the inner and outer corners at the ends of the crossover section, a minimum of the current density occurs, which is caused by the larger cross-section along the line connecting the inner and outer corner.

With decreasing current, the change of the self-field starts at the edges and at the surfaces of the sample (see also figure C.11 - remanent field curve). The derivative of the field changes sign and internal currents flow backwards at the edges and close to the surface, decreasing

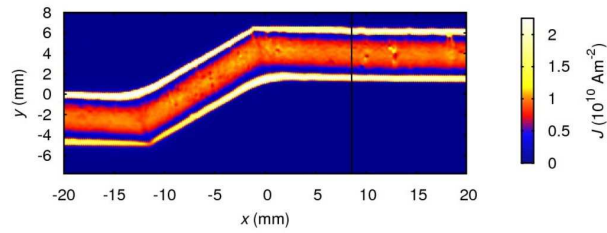
C Homogeneity of Roebel single strands



(a) 30 A



(b) 120 A



(c) 0 A (remanent)

Figure C.12: Current penetration into the two dimensional structure at different applied transport currents. The plots show the absolute local current density. The white arrows in panel (a) are parallel to the direction of the current close to the edges, whereas the black arrows show the current direction of the currents in the middle of the tape. Note that the size of the arrows does not have any physical meaning.

C Homogeneity of Roebel single strands

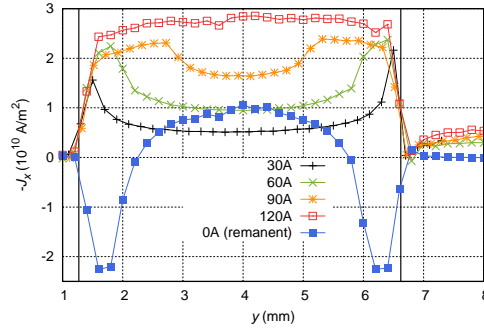


Figure C.13: Cross section of the two dimensional current distribution at $x=8.6$ mm. The solid vertical lines mark the edges of the sample.

the net current through the sample. In the following we define the remaining forward flowing current in the core as core-current. The backwards flowing surface-currents change their direction in the crossover section again later than the currents in the core. Our algorithm evaluates the current flow in a two dimensional structure and does not distinguish between currents flowing close to the surface and those in the core. Therefore, the backwards surface-currents cannot be seen directly in the plots, but they have two effects on our calculations for the remanent state. Firstly, the backwards flowing surface-currents decrease J over the whole cross-section. In the remanent case, the current is made up by the core-current compensated by the backwards flowing surface-current. Figure C.13 shows the distribution of the current component in forward-direction ($-J_x$) in the straight part. Secondly, a forward-current, which is not parallel to the edges anymore and originates from the difference in the directions of the surface- and core-currents mentioned before. Figure C.14 shows the remanent current at the right end of the crossover section. The non-parallel configuration can be seen very clearly.

In order to support our scenario, we subtracted the matrix of the current distribution at 60 A two times from the current distribution at 120 A, which formally leads to the remanent state. The resulting current distribution is indistinguishable from that calculated by the Biot-Savart inversion.

The current distribution of the whole conductor in the remanent state is shown in Figure C.12(c).

C.3.4 Local defects

Self-field measurements and the Biot-Savart inversion are suitable for showing defects in coated conductors. Small defects in the 5 mm wide sample occur between $x = 10$ and 15 mm, leading to a smaller current density (see figure C.12(b)). For demonstration purposes, we investigated a faulty 2 mm Roebel strand. The measurements were performed at 33 A (equivalent to $0.92 I_c$). The current distribution around a defect located in the inner-left corner is illustrated

C Homogeneity of Roebel single strands

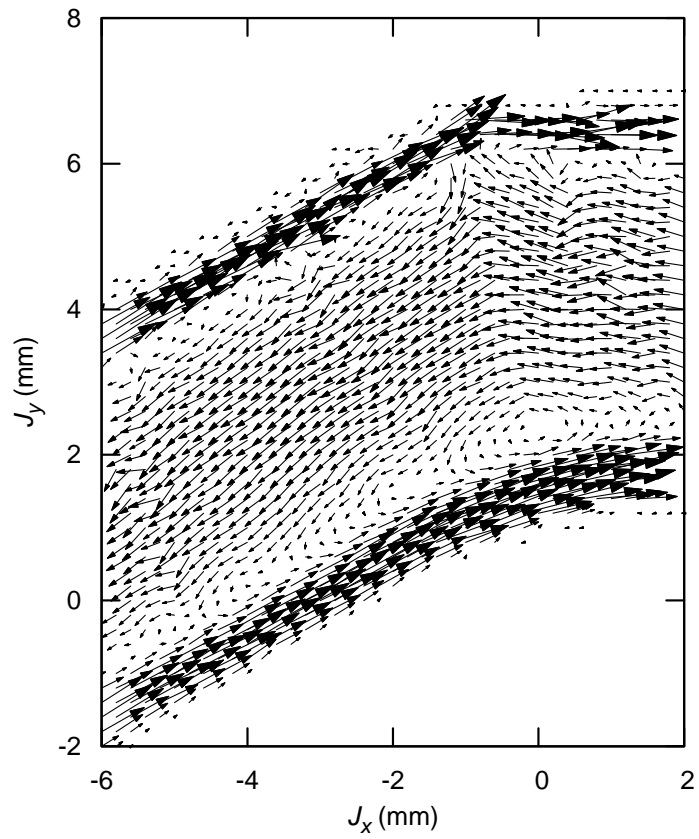
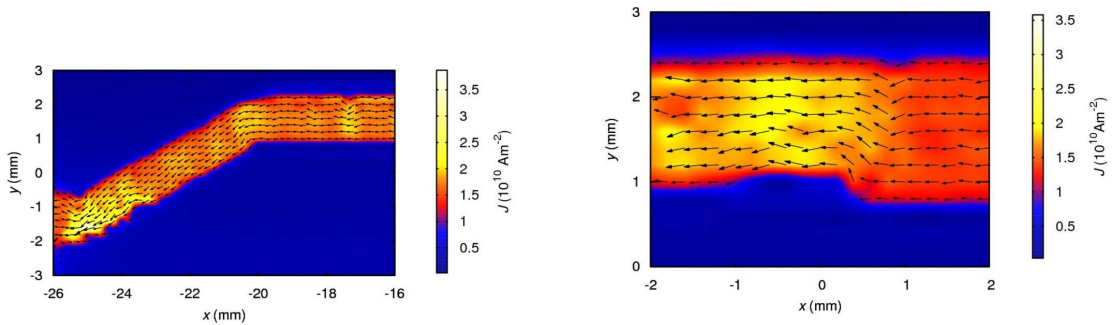


Figure C.14: Current flow at 0 A (remanent) in the crossover section. The initial current was flowing from right to left. Due to the different angles of the surface-current and the core-current the forward-current does not seem to flow parallel to the edges anymore.

C Homogeneity of Roebel single strands

in figure C.15(a). No damage in this region was visible by optical inspection of the strand surface. This defect was either present in the unpunched coated conductor, or caused by the strand manufacture. FEM calculations show that the peak Von-Mises strain occurs in the region of the inner radius [47] if axial strain is applied to the strand. Since the defect is in this region, it is likely that the defect was caused by overstraining the strand. The current has to bypass the defect on the lower side and, therefore, the current density increases close to the opposite corner of the tape. Figure C.15(b) shows the current-flow near the reduction of the



(a) A defect at the inner left corner leads to an enhancement of the current density close to the opposite edge.

(b) Due to a reduction of the cross-section the current density is increased in the left section.

Figure C.15: Current flow close to local defects.

tape width due to a misalignment of the punching machine. The current density on the left part is significantly higher due to the reduction of the geometrical cross-section.

Comparing C.15 and C.7 shows good agreement between the contact free magnetoscan technique and the Hall scans under current flow.

We determined a reduction of the overall I_c by 18% due to these defects with conventional four-point measurements.

C.4 Conclusion

Two major bottlenecks were identified in the 2 mm single Roebel strand from both magnetoscan and Hall-scan measurements. One was caused by a punching misalignment resulting in different strand widths in the straight part. The other was likely to be caused by the applied tensile stress during the production process (defect at the inner left corner).

The single filaments of the 5 mm striated strand were well separated, but one local inhomogeneity was found. It is suspected that this defect was already present in the coated conductor before laser scribing.

C Homogeneity of Roebel single strands

Self-field measurements under current flow were performed successfully on single Roebel strands. Field and current distributions in the straight part agree with the critical state theory of thin films. A slightly different behaviour for currents penetrating from the edges and currents penetrating from the top and bottom surfaces was found in the transverse section of the strand. This results in a non-parallel current flow in the crossover part of a single Roebel strand. The local properties of the conductor can be detected with high-resolution Hall-scan measurements under current flow. Therefore, this technique is very promising for finding problems in the production process of Roebel assembled coated conductors.

D Influence of neutron irradiation on coated conductors

As discussed in Chapter A, fast neutrons will reach the superconducting coils of fusion devices. The influence of neutron irradiation on various properties of a coated conductor are the main topic in this chapter.

Characterisation of fast neutron irradiated coated conductors has a long history at the Atominstitut in Vienna. The results in section D.3 continue previous studies by René Fuger [3] and Michal Chudy [4]. Section D.4 presents the world's first tensile stress measurements on irradiated coated conductors. The set-up for these measurement was developed in this work. Therefore, the set-up is described in more detail in D.2.4.

D.1 Samples

In 2009, the largest manufacturers of commercially available coated conductor were:

SuperPower Inc., a subsidiary of Furukawa Electric Co., Ltd. (Japan) located in Schenectady, NY, USA [48]. Note that SuperPower was a subsidiary of Philips Holding USA until February 2012.

American Superconductor (AMSC) located in Devens, MA, USA. [49]

Bruker EST (formerly European High Temperature Superconductors GmbH EHTS), located in Alzenau, Germany. [50]

State-of-the-art coated conductors characterised in this work were manufactured either by SuperPower or AMSC. Unfortunately, Bruker EST did not provide us with their newest samples in 2009. Nevertheless, irradiation studies of older Bruker (EHTS) tapes are available and were presented in [3] and [4]. Other companies, such as Theva (Germany), Fujikura Ltd. (Japan) [51] and SuNAM (Korea) have demonstrated their ability to produce high-performance coated conductors as well. Laboratories such as LANL (U.S.), KERI (Korea) and ISTEK (Japan) manufacture high-performance coated conductors for R&D, but do not sell them commercially.

The highest critical current per conductor width of the samples from 2009 used in this work, was reached in the GdBCO-SuperPower tape. It was about 360 A/cm at 77 K in self-

D Neutron irradiation

field with a superconducting layer of $1\ \mu\text{m}$ thickness. In 2011, the KERI-laboratory in Korea presented a short length SmBCO tape with $1530\ \text{A}/\text{cm}$ and a superconducting layer of $5\ \mu\text{m}$ at the EUCAS conference 2011. SuperPower presented a Zr:GdYBCO tape with $961\ \text{A}/\text{cm}$ [11]. The superconducting layer is $2.8\ \mu\text{m}$ in this sample.

The two most prominent manufacturers of Roebel cables are:

- Karlsruhe Institute of Technology (KIT) in Germany (formerly Forschungszentrum Karlsruhe)
- Industrial Research Limited (IRL) located in Wellington, New Zealand

The Karlsruhe group originally introduced the Roebel technique to HTS coated conductor [17] and use automated punching and laser scribing methods for cutting and striating single Roebel strands. The assembly of the final Roebel cable is done by hand. In 2010, IRL showed the feasible production of long-length Roebel cables with an automated punching and assembly manufacturing process [19].

D.1.1 SuperPower SCS4050

The SuperPower product code SCS4050 means:

- Superconductor with Copper Stabilisation
- 4 mm width
- $50\ \mu\text{m}$ thick Hastelloy® substrate

The Hastelloy substrate forms the basis of the whole tape. In order to achieve a smooth and clean surface, the substrate is prepared by electro-polishing. An IBAD (Ion Beamed Assisted Deposition)-MgO template generates the bi-axial texture for the superconductor material. The GdBCO layer is deposited by MOCVD (Metal Organic Chemical Vapour Deposition). Lastly, the superconductor is electrically stabilised by a sputtered silver layer and surrounded by electro-plated copper. Figure D.1 shows the architecture and dimensions of the tape.

In our sample of the SCS4050, the use of the rare earth element gadolinium (Gd) results in a superconducting layer made of $\text{GdBa}_2\text{Cu}_3\text{O}_{7-\delta}$. SuperPower often over-dope their RE-content (Gd-content) in order to form RE_2O_3 nano precipitates. These precipitates align more or less parallel to the a,b-plane [14] and form pinning centres. Furthermore, the higher RE-content suppresses the formation of undesired CuO and BaCu_3O_4 phases. In anisotropy measurements, this results in an unsymmetrical behaviour with respect to the c-peak.

Seven stable isotopes of Gd exist. The neutron absorption cross-sections of the five isotopes with the highest natural abundance are shown in Figure D.2.

At thermal energies, the neutron absorption cross-sections of ^{155}Gd and ^{157}Gd are approximately five orders of magnitude higher than that of yttrium (black line). In the epi-thermal

D Neutron irradiation

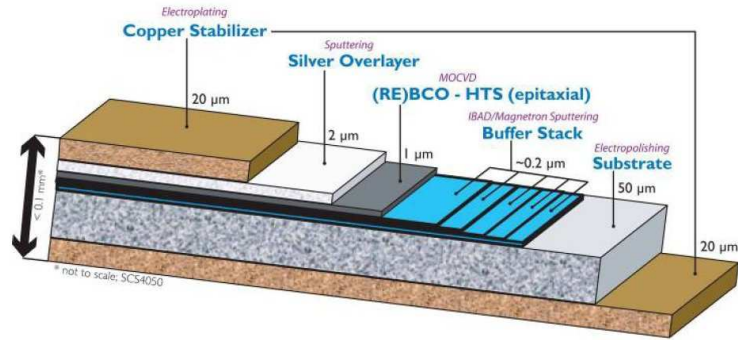


Figure D.1: Architecture of the SuperPower SCS4050 tape. The picture is taken from [48]-

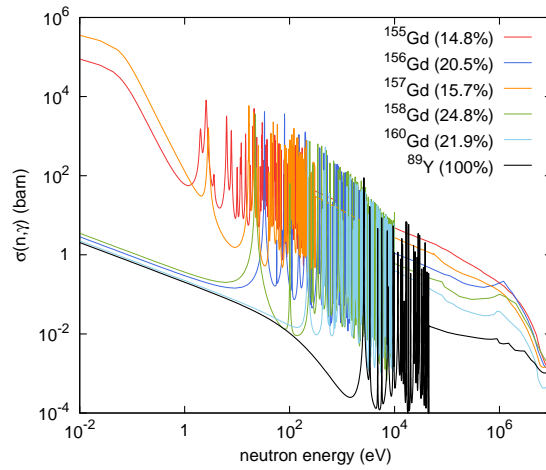


Figure D.2: Neutron absorption cross section $\sigma(n,\gamma)$ of various stable gadolinium isotopes and yttrium. The abundance is written in brackets next to the isotope. The data is taken from [52].

D Neutron irradiation

region ($E < 0.1 \text{ MeV}$), resonances occur over a wide energy range, including lower energies than for yttrium. Furthermore, resonances have at least one order of magnitude higher amplitudes in gadolinium at $\approx 10 \text{ keV}$. From the neutron absorption cross-sections, it is clear that high fluences could influence a GdBCO conductor in a different manner than an YBCO conductor. Results presented in the following will confirm this expectation.

D.1.2 SuperPower SCS 4050AP

The architecture of the SCS4050AP (Advanced Pinning) tape is similar to that of the SCS4050. Additional artificial pinning centres containing RE and Zr have been introduced in order to increase the pinning efficiency of the tapes. The superconducting layer partially contains Gd and Y. The detailed content of Y and Gd is unknown for our sample. In earlier publications SuperPower used a $\text{Zr}_{0.065}\text{Gd}_{0.65}\text{Y}_{0.65}\text{Ba}_2\text{Cu}_3\text{O}_7$ composition [14]. As previously mentioned, the RE:Ba:Cu ratio of 1.3:2:3 (instead of 1:2:3) results in abundant nanometre-sized precipitates of RE_2O_3 . The additional Zr content forms BaZrO_3 nano-columns during the MOCVD process. TEM images of such samples [14] show BZO nano-columns oriented primarily along (but with a certain splay) the c-axis. RE_2O_3 nano-precipitates have an average size of $\approx 9 \text{ nm}$. The RE_2O_3 nano-particles self-align in planes nearly parallel to the a,b-planes of the superconducting matrix.

D.1.3 AMSC 344C

American Superconductor uses the low cost RABiTSTM/MOD (Rolling Assisted Bi-axially Textured Substrate/Metal-Organic Deposition) process to manufacture HTS coated conductors. The samples used consist of a $75 \mu\text{m}$ Ni 5 at.%W alloy as a substrate coated with 75 nm epitaxial buffer layers made of Y_2O_3 , YSZ and CeO_2 . The NiW substrate is textured and the buffer layers are deposited by sputtering. The approximately $0.8 \mu\text{m}$ thick $\text{YBa}_2\text{Cu}_3\text{O}_{7-\delta}$ layer is grown by MOD on the buffer. Finally a silver layer is deposited on the top. Depending on the application, different stabilisers (copper, stainless steel or brass) are soldered onto the HTS-strip. Figure D.3 shows the architecture and figure D.4 the cross-section of the final tape.

Similar to SuperPower, AMSC introduces nano-particles during the the MOD process. The detailed composition of the superconducting layer is unknown to author. A composition of $\text{Dy}_{0.5}\text{Y}_1\text{Ba}_2\text{Cu}_3\text{O}_7$ for AMSC tapes is reported in [54]. The additional content of a RE(Dy) forms nano-dots (size 10-100 nm) of RE_2O_3 and $\text{RE}_2\text{Cu}_2\text{O}_5$ during the MOD process [13]. Furthermore, it has been shown that increasing the Er content x in $\text{Er}_x\text{Y}_1\text{Ba}_2\text{Cu}_3\text{O}_7$ from zero to 0.5 decreases the ratio $J_c(H||a,b)/J_c(H||c)$ from 4.5 to 1.2 at 3 T and 65 K. The ratio in our AMSC samples was about 1.4 at 3 T and 64 K. Therefore, a higher RE content can also be expected in this samples.

D Neutron irradiation

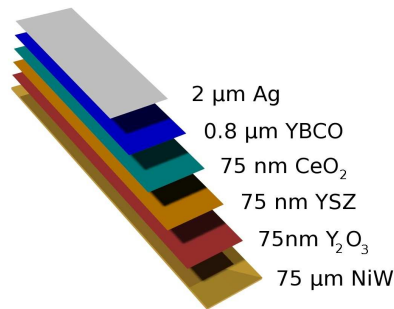


Figure D.3: Architecture of the AMSC 344 tape according to [49].

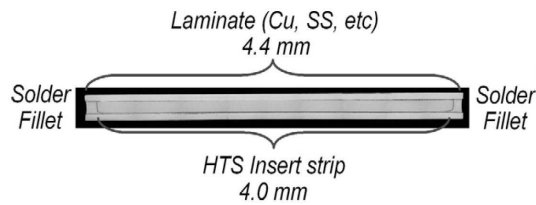


Figure D.4: Cross section of the AMSC 344 tapes. The picture is taken from [53].

The product code 344C means:

- 4.4 mm width
- Copper stabilised tape

Note that in 2011 AMSC changed the name of the 344 wire to AmperiumTM-wire. Further details of the manufacturing process of AMSC can be found in [53].

D.1.4 AMSC 344S

The 344S tape is manufactured as the 344C except for its stabiliser. Stainless steel is used in the 344S conductor in order to enhance its mechanical properties.

Table D.1 shows information provided by the manufacturers of the coated conductors. Table D.2 gives details of the dimensions and introduces our internal sample labelling.

D Neutron irradiation

Type	I_c at LN (A)	Maximum rated tensile stress(MPa)	Maximum rated tensile strain(%)	Manufactured
SP SCS4050AP	94	<550	0.45	2010
SCS4050	140	<550	0.45	2009
AMSC 344C	81	150 (at \approx 300 K)	0.21	2009
AMSC 344S	115	300 (at \approx 300 K)	0.3	2009

Table D.1: Sample data provided by the manufacturers

#Sample code	Type	Purpose	Thickness (mm)	Width (mm)	Length (mm)
SP12	SP SCS4050	TR	0.1	4	26
AC3	AMSC 344C	TR	0.21	4.4	26
AS3	AMSC 344S	TR	0.29	4.4	26
SP15	SP SCS4050	AN	0.1	4	26
SPAP1	SP SCS4050AP	AN	0.1	4	26
AC4	AMSC 344C	AN	0.21	4.4	26
SPZ16	SP SCS4050	TS	0.1	4	50
SPZ5	SP SCS4050	TS	0.1	4	50
ACZ1	AMSC 344C	TS	0.21	4.4	50
ACZ4	AMSC 344C	TS	0.21	4.4	50

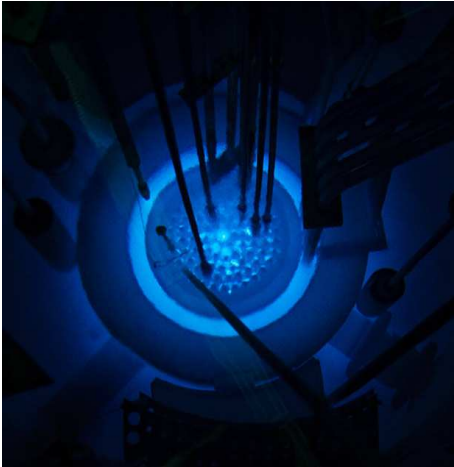
Table D.2: Dimensions of the sample. (Purpose code: TR TRansport measurements; AN ANisotropy measurements; TS Tensile Stress measurements)

D.2 Experimental details and evaluation

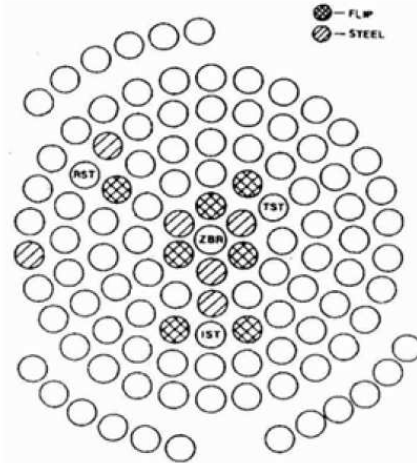
D.2.1 Irradiation facility

All samples were irradiated in the TRIGA Mark II reactor of the Atominstitut / TU Wien. The TRIGA-reactor is a research reactor of the swimming-pool type that is used for training, research and isotope production (Training, Research, Isotope Production, General Atomic = TRIGA). The reactor has a maximum continuous thermal output power of 250 kW. The fuel is in the form of a uniform mixture of 8 wt% uranium, 1 wt% hydrogen and 91 wt% zirconium, where zirconium-hydride is the main moderator. A detailed description of the reactor type can be found in [55].

As already mentioned in chapter A.4, this reactor type provides a “simulation” of the expected neutron spectrum at the position of fusion magnets. Figure D.5 shows the reactor and the core configuration. The flux densities for different neutron energies at the central



(a) Photograph of the reactor core during operation. Picture taken from [55]



(b) Core configuration according to [28]. ZBR marks the central irradiation facility. Note that the FLIP (Fuel Lifetime Improvement Program) and STEEL rods are rearranged, meanwhile.

Figure D.5: TRIGA Mark-II reactor core at the Atominstitut TU Wien

irradiation facility were determined in [28] and are shown in table D.3.

The fluence $\Phi \cdot t$ for different energies is calculated by multiplying the flux density Φ with the irradiation time t and, vice-versa, the irradiation time can be calculated for a desired fluence. As in [3]-[5], $\Phi = 7.6 \cdot 10^{16} \text{ m}^{-2} \text{ s}^{-1}$ was used for the fast neutron flux density in the central irradiation facility. The samples in this work were irradiated for 36h 35min and 62h 22 min to obtain the desired fast neutron fluences of $1.0 \cdot 10^{22} \text{ m}^{-2}$ and $1.7 \cdot 10^{22} \text{ m}^{-2}$, respectively.

For irradiation purposes, coated conductor samples were sealed in a quartz tube slightly

D Neutron irradiation

Energy range	Flux density Φ ($\text{m}^{-2}\text{s}^{-1}$)	Standard deviation (%)
Total	$2.1 \cdot 10^{17}$	± 5.7
Thermal ($E < 0.55$ eV)	$6.1 \cdot 10^{16}$	± 5.1
Fast ($E > 0.1$ MeV)	$7.6 \cdot 10^{16}$	± 11.6
($E > 1$ MeV)	$4.0 \cdot 10^{16}$	± 11.8

Table D.3: Flux densities in the TRIGA reactor at a power level of 250 kW [28].

larger than the sample. Afterwards the quartz tube was embedded in an aluminium container and mounted in the central irradiation thimble (marked as ZBR in figure D.5(b)). After the calculated irradiation time, the aluminium container was stored inside the reactor pool at half height between core and water surface. Due to the high activity of the samples, approximately six months had to pass until the container and the quartz tube could be opened. Typical measured dose rates of the short samples after opening were ≈ 0.1 mSv/h and 0.3 mSv/h at a distance of 5 cm for $\Phi \cdot t = 1.0 \cdot 10^{22} \text{ m}^{-2}$ and $1.7 \cdot 10^{22} \text{ m}^{-2}$, respectively. Note that the time between irradiation and opening of the quartz tube was longer for the less irradiated samples, due to organisational reasons. The samples were stored in lead containers when not used for measurements.

D.2.2 Transport and irreversibility line measurements in the 17 T-magnet

Transport and irreversibility line measurements for fields $H||c$ and $H||a,b$ were performed in the 17 T-magnet set-up. In this set-up, a superconducting NbTi-Nb₃Sn composite coil is mounted vertically in a helium bath. Samples with their surface orientated parallel or perpendicular to the field are inserted with a sample rod from the top into the VTI (Variable Temperature Insert). A pump connected to the VTI lowers the pressure inside the VTI and therefore helium gas flows from the liquid helium reservoir passing a heater, the sample and the bus bars to the external gas reservoir. By controlling the heater power, the sample temperature can be varied. Fields between zero and 15 T were used in this work. A four-point technique was used in order to detect the voltage at a given current. The current contacts were realised with pressed indium contacts and the voltage contacts with spring probes. The temperature was measured with a cernox sensor fixed close to the coated conductor.

D.2.3 Anisotropy measurements in the 6 T-magnet

Anisotropy measurements at intermediate fields (0-6 T) were performed in the 6 T-magnet set-up. Figure D.6(b) shows the whole set-up. The set-up is equipped with a superconducting split-coil magnet, which is mounted in the liquid helium bath generating a horizontal field. A sample holder with a vertically mounted coated conductor can be inserted into the cold part (VTI) of the set-up. Hence, the field is always perpendicular to the current and therefore

D Neutron irradiation

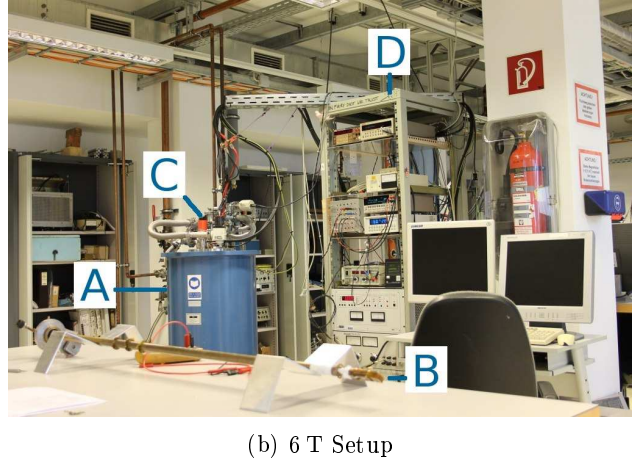
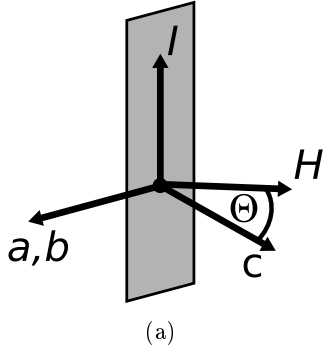


Figure D.6: (A) Split coil cryostat with horizontal magnetic field, (B) extracted rotatable sample rod, (C) cold part inlet, (D) control- and measurement-equipment

maximum Lorentz force acts on the vortices. The angle Θ between the c -axis of the tape and the applied field H can be varied by rotating the sample rod between zero and 360° . Figure D.6(a) shows this configuration. The temperature is varied similar by the 17 T set-up. Four-point measurements were again performed in order to measure the resistivity. The current contacts were implemented by pressed indium contacts and the voltage contacts were glued with silver paste. A Cernox temperature resistor was used to detect the temperature close to the sample.

D.2.4 Tensile stress measurements

Set-up

A tensile stress set-up was developed in this work and drawn with the CAD software Solid Edge. Afterwards, it was manufactured by the workshop of the Atominstitut. Finally the entire set-up was assembled and operated in the laboratory.

Tensile stress measurements on irradiated insulating materials at liquid nitrogen temperatures for fusion coils have a long tradition at the Atominstitut, but characterisations of critical currents under tensile stress were not performed at our laboratory so far. The existing set-up, equipped with a 100 kN load cell, is not suitable for four-point measurements.

From the start, the idea of extending the available set-up was considered not viable. The main reason for disregarding a potential extension was based on the expectation of the maximum force applied to coated conductors being in the range of 1 kN rather than 100 kN.

Therefore, a new set-up was designed with the further advantage of being positioned in-between an existing split-coil rotating 1.4 T-electromagnet in order to measure anisotropy under tensile stress. By the end of the first year of this PhD, the majority of the tensile stress

D Neutron irradiation

set-up as illustrated in D.7(b), was ready for operation.

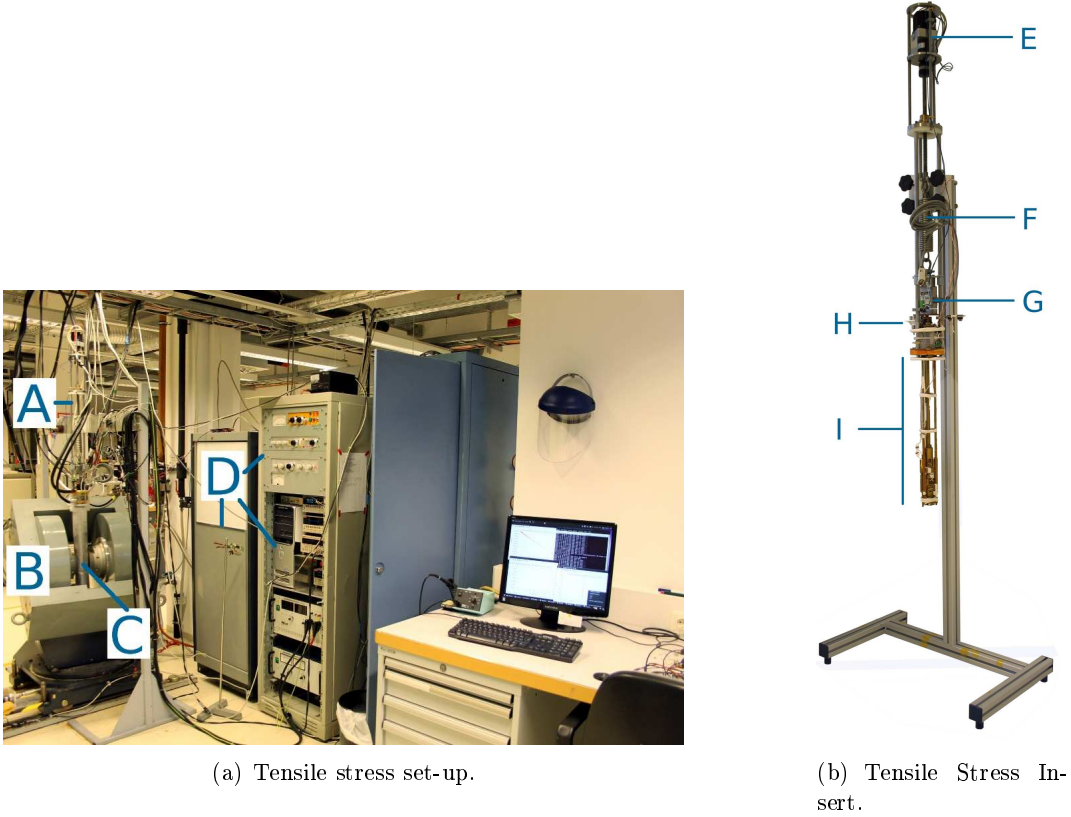


Figure D.7: Photos of the tensile stress set-up. (A) Tensile stress insert assembled in between the electromagnet, (B) electromagnet, (C) dewar with cold part of the tensile stress insert inside, (D) control and measurement equipment, (E) stepper motor, (F) removable spring, (G) load cell, (H) connections, heating resistor, thermal switch, safety spring, etc., (I) cold part

Many parameters had to be considered in the design process and will be described in the following.

- One limiting factor of the set-up was the space between the two poles of the electromagnet. The cold part, marked I in figure D.7(b), had to fit into this space and therefore the maximum diameter of the scaffold was limited to 5 cm. The maximum applied force had to be 1 kN. In order to reach this value, minimum diameters of the push and pull rods were given as well, which also reduced the space.
- Currents of up to 300 A have to flow through the bus bars to the superconductor.
- Varying liquid nitrogen levels in the dewar would lead to periodic thermal expansion and compression of the scaffold, and therefore on the sample, if push and pull rods behave differently.

D Neutron irradiation

- Setting a certain force with a stepper motor was considered as difficult, as the maximum applied force is expected to be at an elongation of typically $\approx 0.6\%$ i.e. ≈ 0.3 mm in a typical sample.

Several designs were visualised with Solid Edge and finally a set-up with the following key properties was realised:

- The scaffold is used as bus bar. Therefore brass was considered the material of choice for the cold part. The current flows over the pull rod (B in D.8(a)) to the upper part of the removable carriage (C in D.8(a)). The sample is connected with pressed indium contacts (E in D.8(b)) to the upper and lower part of the carriage, whereas the guide rods (O in D.8(c)) are insulated from the upper part. Hence, the current flows through the sample and back to the current source through the push rods (A in D.8(a)).
- The applied force is measured by a 2 kN load cell (Tedeia-Huntleigh 615MG) at room temperature.
- The stepper motor is mounted on top with its rotation axis parallel to the pull and push rods. With a trapezoidal thread the rotation is transformed to a translation along the pull rod axis. A ball bearing between load cell and thread rod prevents the lower parts from rotating. A spring is used to transduce the force between the stepper motor and the pull rod.¹ Differences in the thermal expansion of pull and push rod could be disregarded with this solution as well. The force is set with a stepper motor (Nanotec ST5709M1808A) controlled by a stepper motor controller (RN-Schrittmotor).
- The sample is fixed in a removable carriage. This has the advantage, that an irradiated samples could be mounted first in a laboratory equipped for radioactive sample manipulation and finally assembled with the whole set-up in the low temperature laboratory.
- A Hall sensor detects the magnetic field parallel to the tape surface (L in figure D.8(c)). The signal measured by this sensor is a sine function of the angle between the active area of the sensor and the applied magnetic field. This data is used during the evaluation process to calculate the correct angle (Θ) of the applied field. During the measurements, the angular information is obtained from the stepper motor, which controls the rotation of the electromagnet.
- The voltage contacts are glued with silver paste to the conductor (G in D.8(b)), allowing small position rearrangements due to elongation.

After initial tests the following key features were added:

¹Thanks again to Florian Hengstberger for this brilliant and simple solution.

D Neutron irradiation

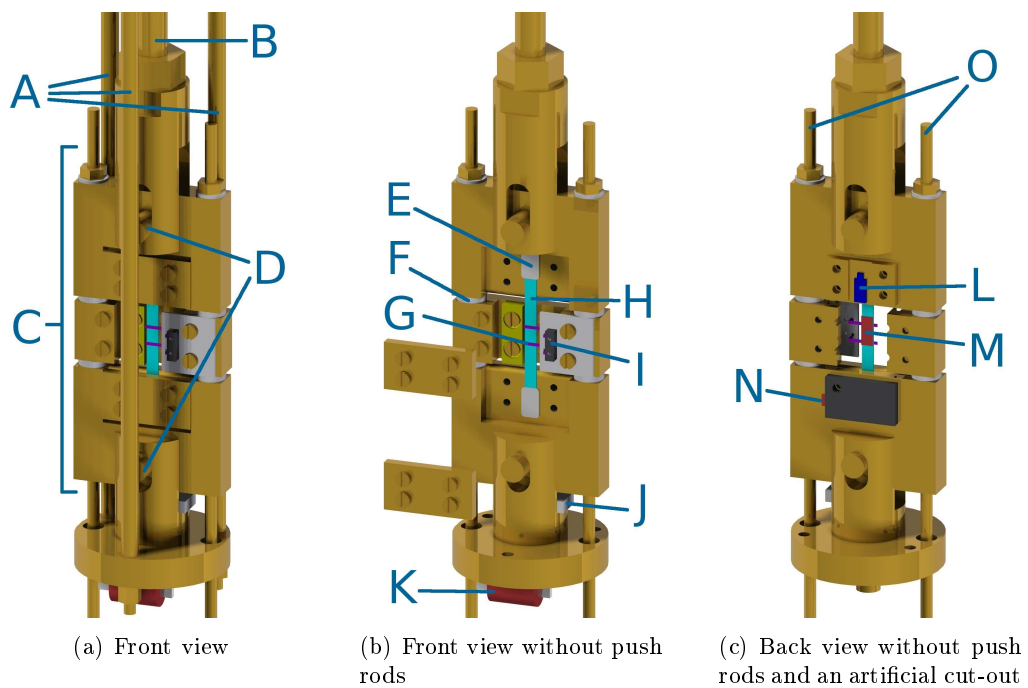


Figure D.8: Detailed CAD-images of the lower cold part of the set up. Note that wires and cables are not depicted. Description: (A) Push rods, (B) pull rod, (C) removable carriage, (D) bolts, (E) indium sheets, (F) PVC-washers, (G) voltage contacts, (H) coated conductor, (I) voltage pins, (J) thermal switch, (K) heating resistor, (L) Hall probe, (M) strain gauge, (N) reference strain gauge on reference coated conductor, (O) guide rods

D Neutron irradiation

- Tensile strain also needs to be measured. In order to measure the strain independently of the temperature, a stress-free strain gauge was assembled close to the sample (N in figure D.8(c)) on a small coated conductor of the same type as the measured sample. Another strain gauge was glued directly onto the coated conductor with epoxy resin (M in fig. D.8(c)), measuring the strain of the sample. Both strain gauges were attached to a tunable Wheatstone bridge as shown in figure D.9. The equilibrium state at zero applied strain was set with a precision potentiometer R_{cal} . The measured bridge voltage is given by:

$$V_{bridge} = \frac{V_{supply}}{4} K \varepsilon \quad (D.1)$$

where V_{supply} is the DC supply voltage, K is the gauge factor given by the strain gauge and ε is the applied strain. Strain gauges for cryogenic use (TML CFLA-3-350-11-4FA-LT) were used in the set up with a gauge factor $K = 2.05 \pm 1\%$. The tensile strain ε can be calculated from equation D.1.

- Heating resistors and thermal switches were placed at the bottom (K and J in figure D.8(b)) and close to the current plugs (H in figure D.7(b)). After the last measurement or after a fault, the computer program automatically starts a heating sequence for controlled heating to room temperature. The thermal switches were placed in series connection with the heating resistors protecting the sample from high temperatures. The upper thermal switch opens at 50°C and the lower switch at 70°. The temperature at the sample never exceeded 40°C during the heating process.
- An accurate Pt100-Class 1/5 resistor was used to measure the temperature close to the sample. The resistor was calibrated in the 17 T set-up with a Cernox-resistor. Nevertheless, the temperature had a constant absolute error of about -0.3 K during all measurements when compared to reference data of liquid nitrogen. One reason for this constant deviation could be a thermo-voltage, as the current was not reversed during one measurement in the tensile stress set-up. However, as the deviation did not change during all measurements and due to lack of time, the temperature sensor was not recalibrated.
- Liquid nitrogen can be automatically filled by a computer controlled magnet valve for cryogenic use (Consarctic SOL DN6 AS R1/4" 24VDC). Two non-calibrated Pt100-Class B resistors were used to detect low and high liquid nitrogen levels in the dewar. Both resistors were insulated and mounted on a push rod.
- The connections above the cold part (H in D.7(b)) were mainly sealed with a PMMA (Poly Methyl MethAcrylate also known as Plexiglas®) tube, surrounding the whole upper part. This casing reduced freezing of air moisture on the set-up and especially along the pull rod.

D Neutron irradiation

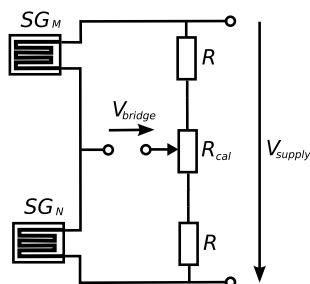


Figure D.9: Electric circuit of the strain gauges

The whole set-up was controlled by a self-written python-framework which was developed in this work and in [56][57]. The open source software Gnuplot [58] and the python binding pyGnuplot [59] were used for visualising data during the measurements. In the programming code, special emphasis was given on simplicity, traceability and the usage of open source software. Nevertheless, to adopt the set-up, basic programming knowledge is required. In order to keep the code small and simple, no code was written for unnecessary graphical user interfaces.

In the course of a master thesis [57], an external USB-ADC/DAC card LabJackU6 [60] was implemented in the set-up in order to set the field of the magnet. Furthermore, the existing stepper motor controller was implemented to control a second stepper motor in order to rotate the magnet.

The external USB-ADC/DAC card has been recently also used to control a self-built relay box to switch the water valve for magnet cooling, the liquid helium valve and the heating resistors. Furthermore, the four-point measurements of the liquid nitrogen level temperature sensors were also performed with the external USB-ADC/DAC card using their internal fixed current source.

The features of the entire set-up are summarised by input and output parameters in the following table.

D Neutron irradiation

Input parameters	Description
I	Current through the sample. Set by the 40 A or 300 A-current source.
F	Force applied to the sample. Set via the first stepper motor position to values between 0 and 1 kN (tested up to 0.5 kN).
$\mu_0 H$	Applied magnetic field. Set via the DAC-card to fields between 0 and 1.4 T.
Θ	Field orientation. Set via the second stepper motor position to angles between 0 and 230°.
Water valve	Cooling water valve (open/close).
LN valve	Liquid nitrogen valve (open/close).
Heater	Heats up the cold part of the set-up.
Output parameters	Description
V	Voltage at the sample, measured by a Keithley 182 Nanovoltmeter.
I	Current through the sample, measured over a 0.1 Ω shunt.
T	Temperature close to the sample, measured with a Pt100 resistor.
B_{Hall}	Magnetic field perpendicular to the sample surface, measured with a Hall sensor.
F	Applied force, measured with a load cell.
ϵ	Applied strain, measured with a Wheatstone bridge and strain gauges.
Φ	Field direction, evaluated from the position of the stepper motor and/or the Hall voltage.
T_{HL}, T_{LL}	Temperatures at the position of the liquid nitrogen level sensors.
Water flow	Flow rate of the cooling water (flow / no flow).

Measurement loop

The complete characterisation at one fixed applied force is done within one measurement loop. A loop starts by increasing the force stepwise from the relaxed state to the desired force. At each step, the self-field I_c is measured. Between each step, the sample returns to the relaxed state and I_c is re-measured. Hence, the dependence of the self-field I_c on the stress/strain as well as the stress-strain dependence, are obtained from these measurements. If the sample does not enter the irreversible region, where the sample is irreversibly damaged, anisotropy measurements begin after reaching the final force. Anisotropy measurements were performed at 0.1 T, 0.2 T, 0.4 T, 0.6 T, 1 T and 1.4 T. After the last measurement, the computer program begins the heating process. It has proved practical to begin the heating process no later than 30 hours after the beginning of the measurement loop. After 30 hours, problems with

D Neutron irradiation

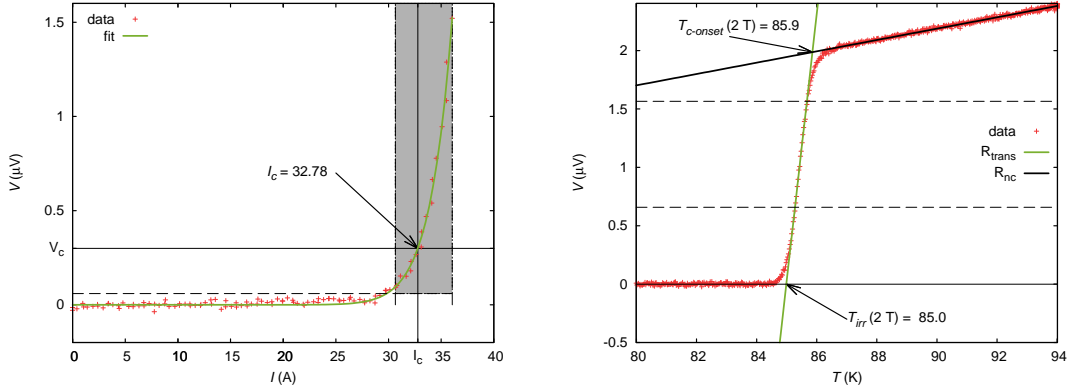
ice formation along the pull rod can influence the measurements. One measurement loop required approximately 44 h, including 18 h of heating. Typically, anisotropy measurements were performed at nine different forces, leading to a net measurement time of typically around 400 hours for one sample.

D.2.5 I_c -Evaluation

The critical current was evaluated at a critical electric field $E_c = 1 \mu\text{V}/\text{cm}$ corresponding to a critical voltage $V_c = l E_c$. Here l denotes the distance between the voltage contacts. The transition between loss free and dissipative phase can be described by the power law:

$$\frac{E}{E_c} = \left(\frac{I}{I_c} \right)^n \quad (\text{D.2})$$

In (D.2), the voltage-current behaviour is characterised by the critical current I_c and the n - value. Both values were evaluated by fitting the measured data. Figure D.10(a) shows an example.



(a) V/I curve of the pristine tape SP12 at 77 K and at 1.5 T. The solid green line is the fit according to (D.2). Note that a DC offset was subtracted before. The grey shaded area marks the region of the fit.

(b) Resistivity of an IRL Roebel single strand at 77 K and 2.0 T. The dashed lines mark the lower and upper limit for the fit of the transition.

Figure D.10: Evaluation of I_c from a V/I curve and $T_c(B)$ from a transport measurement.

D.2.6 Irreversibility line and $T_{irr}(B)$ -evaluation

The critical temperature ($T_c(0)$ or just T_c) is defined as the transition temperature between the normal conducting and the superconducting phase at zero field. In this work, the transition temperature at zero resistivity evaluated from the transition tangent and denoted as $T_{irr}(B)$

D Neutron irradiation

is used for comparison. The evaluation is shown in figure D.10(b). T_c was evaluated at the same criterion as T_{irr} in zero field. T_{irr} is associated with the irreversibility field B_{irr} .

The evaluated values $T_{irr}(B)$ can be plotted versus the applied field. These plots are called “irreversibility line”. The obtained data is presented in section D.3.2.

Besides the definition of $T_{irr}(B)$ and $T_{c-onset}(B)$, figure D.10(b) shows the change of the resistivity of a coated conductor with changing temperature. In the normal conducting region ($T > 86$ K), the current flows mainly through the surrounding copper.

D.3 Results and discussion of transport measurements

D.3.1 Homogeneity of the tapes

In recent years, the long-length homogeneity of coated conductors has continuously improved. A few years ago, the magnetoscan technique, discussed in chapter C.2.1, detected several defects in coated conductors. All samples of state-of-the-art tapes used in this work, were shown to be fairly homogeneous and no large defects were detected in the pristine samples. Figure D.31(a) and D.32(a) on page 116ff. show magnetoscans of a SuperPowerSCS4050 and an AMSC-344C tensile stress sample before testing. The signal in both samples was undisturbed over their entire length, due to the high quality of the superconducting films. The difference in the magnetic field between the two samples originates from the paramagnetic NiW-alloy substrate of the AMSC sample, which amplifies the applied field from the permanent magnet. This paramagnetic field of the NiW-alloy also enhances the AC losses. Hence, several groups try to find non-paramagnetic alloys for the RABiTS process. The field of the permanent magnet field was subtracted from the local field B in the magnetoscan images.

D.3.2 Transport properties in the main field orientations at high fields (0 to 15 T)

The measurements presented in this section were mainly performed in the 17 T-set-up using the samples SP12, AS3 and AC3. Since AS3 and AC3 behave similarly, only AC3 is discussed in the following. The pristine samples were characterised before and after irradiation to $\Phi \cdot t = 10^{22} \text{ m}^{-2}$. In order to compare these results with results at higher fluences, the transport measurements on SP15, SPAP1 and AC4 (up to 6 T) are included. The samples SP15, SPAP1 and AC4 were irradiated to a fluence of $\Phi \cdot t = 1.7 \cdot 10^{22} \text{ m}^{-2}$ and characterised in the 6 T set-up. All samples with the same first letters (e.g. SP12 and SP15) were taken from the same spool and therefore the same pristine performance can be expected. Nevertheless, if the data prior and after irradiation were not obtained from the sample, the fluence is marked with an asterisk (*) in the figures of this section.

D Neutron irradiation

At high fields ($>1\text{T}$), the critical current density depends mainly on the intra-grain currents, whereas the critical current in low fields depends mainly on the misalignment between the grain boundaries in unirradiated coated conductors [15][16]. As previously mentioned, two main mechanisms can generally be expected from neutron irradiation. The first is a reduction of the critical temperature T_c due to oxygen displacements (point defects). The second is an enhancement of the pinning efficiency due to the introduction of uncorrelated pinning centres by fast neutrons. After irradiation J_c is reduced in low fields and enhanced at high fields (at sufficiently low temperatures where the T_c reduction does not play a role) providing evidence that the inter-grain J_c is reduced after irradiation, whereas the intra-grain J_c is enhanced. The latter is explained in a straight forward way by the enhanced pinning due to the additional pinning centres. An accumulation of the mobile point defects at the grain boundary and/or an enhancement of the local field at the grain boundary, due to the enhanced intra-grain J_c was suggested to be responsible for this reduction at low fields [5].

At low temperatures, the pinning efficiency is higher, due to the smaller thermal energy. In particular, smaller defects become more efficient at low temperatures and the enhancement of J_c is after irradiation is more pronounced after the irradiation.

All these mechanisms influence the critical current density J_c . At elevated temperatures close to T_c , the T_c -reduction dominates and J_c decreases even at low fluences. At lower temperatures, the enhancement due to the added pinning centres dominate and J_c increases to a certain fluence $\Phi \cdot t_{max}$, before it decreases as the T_c -reduction becomes dominant. This critical dose depends mainly on field, temperature and on the starting material.

The previously explained effects can be described qualitatively with a temperature scaling law for the pinning force. Note that it is not the author's aim to explain the change of pinning due to neutron irradiation theoretically but to figure out the changes of the critical currents due to neutron irradiation by a strongly simplified model. The reduction of J_c at low fields and the enhancement of J_c at high fields can formally be described by a higher $B_{irr}(0\text{K})$ and B_{c2} in irradiated samples.

In many scaling laws, the pinning force is expressed by:

$$F_p(B, T) \equiv I_c B = Ch(T)f(b) \tag{D.3}$$

where C is a constant, $h(T)$ is a function of temperature and $f(b)$ is a function of the reduced field $b = B/B_{irr}$. The temperature function can be expressed as:

$$h(T) \approx \left(\frac{B_{c2}(T)}{B_{c2}(0)} \right)^\eta \tag{D.4}$$

D Neutron irradiation

where $B_{c2}(0)$ is the upper critical field at $T = 0$ and η is typically ≈ 2 . The upper critical field dependence can be approximated by:

$$B_{c2}(T) \approx B_{c2}(0) \left(1 - \left(\frac{T}{T_c} \right)^\sigma \right) \quad (\text{D.5})$$

where σ is typically ≈ 1.5 in coated conductors. One can rewrite D.4 as:

$$h(T) \approx \left(\left(1 - \left(\frac{T}{T_{c0}} \right)^\sigma \right) \right)^\eta \quad (\text{D.6})$$

The field dependence of the pinning force is often given by [61]:

$$f(b) = b^p (1 - b)^q \quad (\text{D.7})$$

where typical values for p and q are about 0.5 and 3 in coated conductors. The irreversibility field is given by:

$$B_{irr}(T) \approx B_{irr}(0) \left(1 - \left(\frac{T}{T_c} \right)^\sigma \right) \quad (\text{D.8})$$

Using D.6 and D.7 in D.3 gives for the field and temperature dependent critical current:

$$I_c \approx C \left[\left(1 - \left(\frac{T}{T_c} \right)^\sigma \right)^\eta \right] \left[\frac{1}{B} \left(\frac{B}{B_{irr}(T)} \right)^p \left(1 - \frac{B}{B_{irr}(T)} \right)^q \right] \quad (\text{D.9})$$

The left term in D.9 will always decrease with decreasing T_c . The right part depends mainly on $B_{irr}(T)$, which is related to T_c and $B_{irr}(0)$ by D.5. An enhancement of $B_{irr}(T)$ would lead to higher critical currents at higher fields but lower critical currents in lower fields. As previously mentioned, neutron irradiation enhances the upper critical field B_{irr} , but decreases T_c .

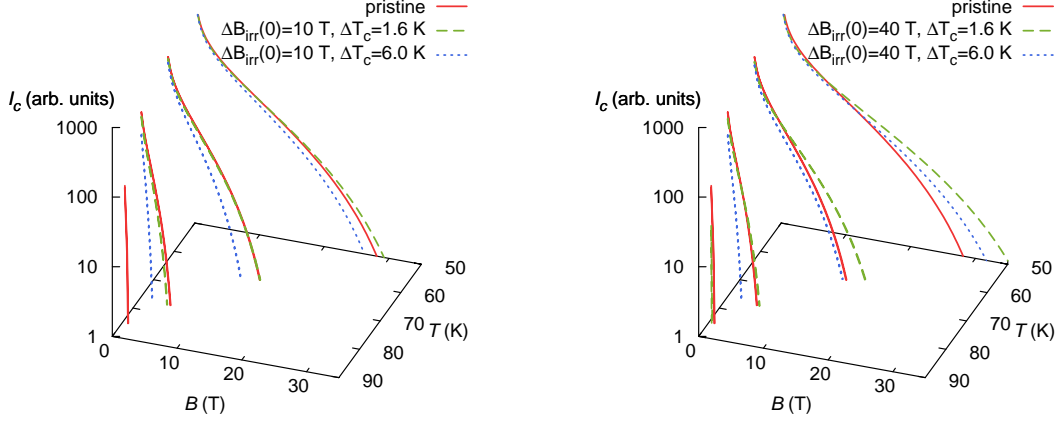
In order to get a feeling for the I_c change after irradiation, two different situations are illustrated in figure D.11 for typical parameters ($p=0.5$, $q=3$, $\sigma = 1.5$, $\eta = 2$, $T_c=89$ K, $B_{irr}(0)=B_{c2}(0)=120$ T).

I_c in the pristine sample is represented by the red solid line ($T_c = 89$ K), I_c in the irradiated sample with a small reduction of $\Delta T_c=1.6$ K is illustrated by the green dashed line and the blue dotted line was calculated by assuming a higher T_c reduction of $\Delta T_c=6$ K.

In D.11(a), a rather small enhancement of B_{irr} is assumed that is similar to the situation for $H||a,b$. At high temperatures, the T_c reduction dominates and I_c in the pristine sample is always higher than in the irradiated sample. At intermediate temperatures, I_c remains more or less the same after irradiation. At low temperatures and high fields, I_c is enhanced for $\Delta T_c=1.6$ K. For the $\Delta T_c=6$ K-assumption, I_c is always reduced.

Figure D.11(b) shows calculations for a rather high enhancement of B_{irr} similar to the situation for $H||c$. In this situation, the irradiated sample with $\Delta T_c=1.6$ K also reaches

D Neutron irradiation



(a) Small enhancement of $B_{irr}(0)$

(b) Strong enhancement of $B_{irr}(0)$

Figure D.11: Changing of I_c by changing of $B_{irr}(0)$ and T_c

higher I_c -values at high fields and temperatures $\lesssim 77$ K. The I_c reduction for the $\Delta T_c = 6$ K-assumption is not as pronounced as in the $H \parallel a, b$ situation, especially at lower temperatures. Crossover situations between pristine and irradiated samples should be observed in measurable field ranges (0 to 15 T) for such a configuration.

At the highest illustrated temperature (85 K), I_c is reduced at all fields in both situations.

Note that p and q in D.7 and D.9 describe the nature of the pinning forces in the superconductor. Therefore, these parameters can change with irradiation as well. In [3] an enhancement of p and q to respectively ≈ 0.7 and ≈ 4 was found after irradiation. Furthermore, the introduced pinning centres are more effective at low temperatures, as previously explained. Hence, a further enhancement at lower temperatures is expected (and therefore a move of the crossover to lower fields). Both changes were not considered in figure D.11, but will be seen in the following sections.

Irreversibility line

T_c is reduced in irradiated samples, due to enhanced impurity scattering caused by point defects and point defect clusters.

Figure D.12 shows the change of $T_{irr}(B)$ at all measured fields for the AMSC tapes. T_c in the pristine samples were 89.6 K and 89.8 K in the 344S and 344C tape, respectively. It is clear from the difference of $T_{irr}(15$ T) that the 344S tape has a steeper slope of the irreversibility line and therefore a slightly higher $B_{irr}(0)$. Hence, the pinning efficiency is slightly better for the 344S tape, resulting in higher current densities at the same temperature. Indeed, transport measurements showed higher critical currents in the 344S tape.

D Neutron irradiation

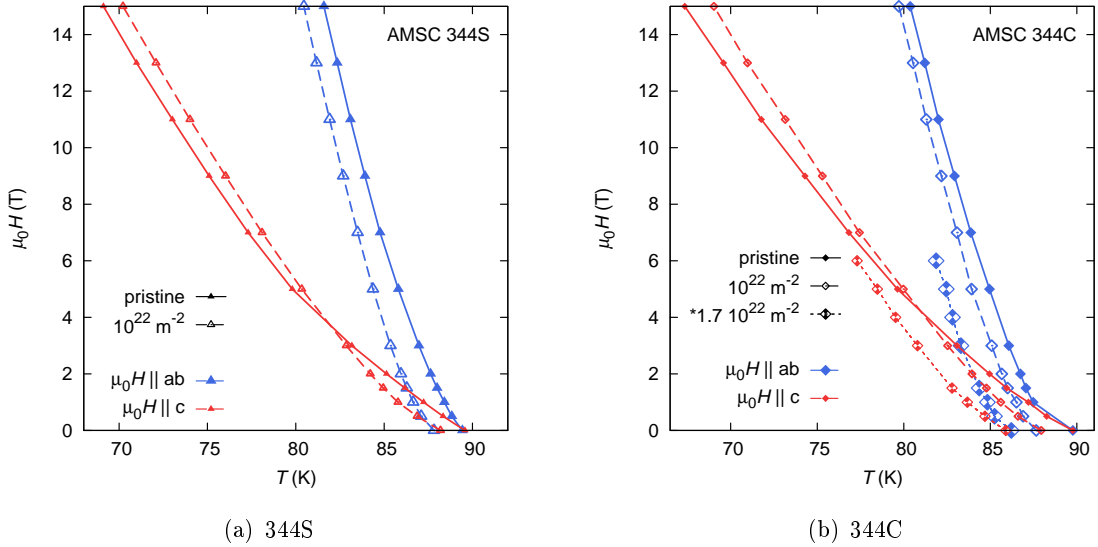


Figure D.12: Irreversibility lines of AMSC pristine and irradiated samples. The data points represent the T_{irr} values at various fields.

In earlier work, a linear reduction of T_c with fluence by about $2 \cdot 10^{22} \text{ K m}^2$ (2 K at a fluence of 10^{22} m^{-2}) was found for YBCO coated conductors [5]. In the analysed samples, the reduction of T_c is 1.4 K for the 344S tape and 1.8 K for the 344C tape at a fluence of 10^{22} m^{-2} . At a fluence of $1.7 \cdot 10^{22} \text{ m}^{-2}$, T_c was reduced to 86.2 K in the 344C conductor, which corresponds to a reduction of $2.1 \text{ K}/10^{22} \text{ m}^{-2}$. The moderate reduction of $T_{irr}(B)$, and therefore the reduction in $B_{irr}(T)$ at high temperatures, is counterbalanced by the irreversibility line becoming steeper and $B_{irr}(T)$ being enhanced at lower temperatures, due to induced defects. The steeper irreversibility lines, especially for $H \parallel c$, show that the pinning efficiency can be further improved by defects. The difference between the steepness of the irreversibility line for $H \parallel c$ between $\Phi \cdot t = 10^{22} \text{ m}^{-2}$ and $\Phi \cdot t = 1.7 \cdot 10^{22} \text{ m}^{-2}$ in figure D.12(b) is significantly smaller than that between the pristine sample and the lower fluence. This decreasing sensitivity due to the defect density could indicate an upper limit for $B_{irr}(0 \text{ T})$.

Figure D.13 shows the irreversibility lines of the SuperPower tapes.

The reduction of T_c in the SuperPower conductors was significantly higher than in the AMSC tapes. At a fluence of 10^{22} m^{-2} , T_c of the SCS4050 conductor was reduced from 92.9 K to 86.7 K in self-field (figure D.13(b)). At a fluence of $1.7 \cdot 10^{22} \text{ m}^{-2}$, T_c decreased to 67.6 K. This strong degradation in the GdBCO tape may originate from the high density of point defects, due to the high absorption of thermal and epi-thermal neutrons. These point defects are pair braking in d-wave superconductors, resulting in a lower T_c . The slope of the irreversibility line changes significantly under irradiation. At 10^{22} m^{-2} , the slope is steep according to a high $B_{irr}(0 \text{ K})$. This change is more pronounced than in the AMSC tapes, which indicates

D Neutron irradiation

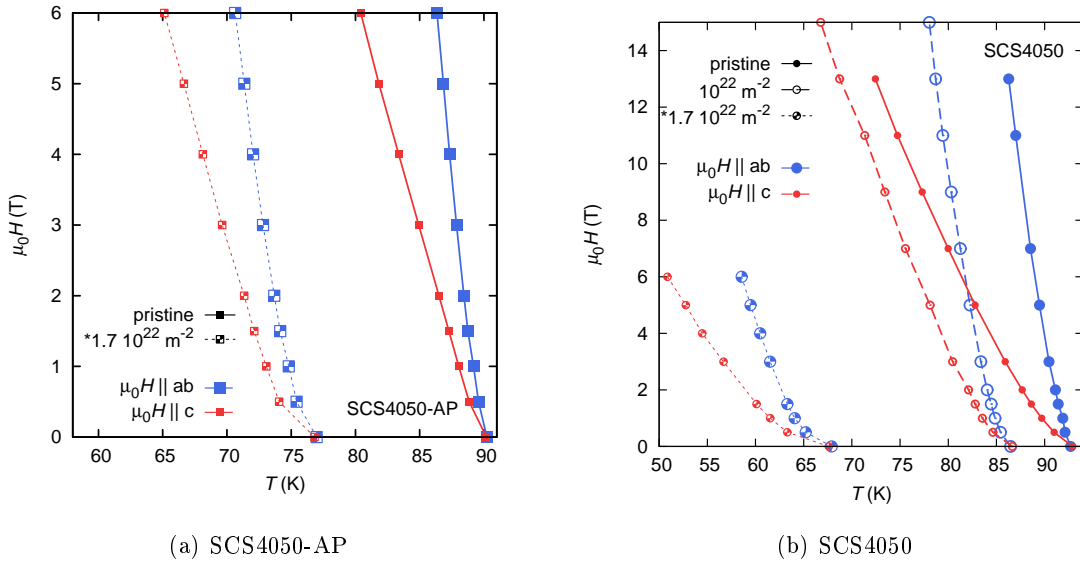


Figure D.13: Irreversibility lines of SuperPower pristine and irradiated samples. The data points represent the T_{irr} values at various fields.

a lower pinning efficiency in the SuperPower conductor in this field direction for the pristine sample. After irradiation to $1.7 \cdot 10^{22} \text{ m}^{-2}$, the irreversibility line becomes less steep again.

The pristine SCS4050AP tape (YGdBCO) has a lower T_c of 90.2 K in self-field (figure D.13(a)). At a fluence of $1.7 \cdot 10^{22} \text{ m}^{-2}$, T_c was reduced to 76.9 K. The lower gadolinium content in this sample leads to a smaller dependence of T_c with respect to neutron irradiation. The slope of the irreversibility line does not change noticeably for both field directions after irradiation, which indicates that the pinning efficiency was already high.

The irreversibility line of the pristine AP-sample is significantly steeper compared to the SuperPower sample without artificial pinning centres for $H||c$. At 6 T, T_{irr} is only 1 K lower in the AP-sample whereas the difference in T_c is 2.7 K (compare $T_{irr}(6 \text{ T})$ in figure D.13(b) with D.13(a)). One can extrapolate that for even higher fields $T_{irr}(B)$ of the AP-sample will exceed that of SCS4050.

Note that in a previous study [62], GdBCO bulk samples did not show a reduction of T_c after irradiation with thermal neutrons at low fluences ($\Phi \cdot t \leq 9.75 \cdot 10^{20}$, $E < 0.5 \text{ eV}$). The strong reduction in T_c is therefore an effect of the high fluence of thermal neutrons and/or an effect of the epi-thermal neutrons. Thermal neutrons are hardly present at fusion coils, whereas epi-thermal neutrons ($0.5 \text{ eV} < E < 0.1 \text{ MeV}$) reach the magnets (see figure A.7 on page 13). Hence, the question of which mechanism lowers T_c in GdBCO is crucial for any application in a fusion coil.

D Neutron irradiation

Critical current density J_c

Until the measurement of the 2009-SuperPower tapes (present tapes), all coated conductors showed an enhancement of J_c at a fluence of $1 \cdot 10^{22} \text{ m}^{-2}$ at 64 K and high fields and a reduction of J_c in low fields. The crossover between reduction and enhancement in the 2007-AMSC samples was at $\sim 8 \text{ T}$ and 0.3 T for fields $H||_{a,b}$ and $H||_c$, respectively [3]. In the current AMSC samples the crossover for $H||_{a,b}$ was found at $\sim 6 \text{ T}$ and the currents for $H||_c$ were enhanced in the entire measurement range (2 T - 15 T), as will be shown later.

In the 2007-SuperPower samples, the crossover at 64 K was at $\sim 6 \text{ T}$ for fields $H||_{a,b}$ but J_c was enhanced in the entire measurement range ($\mu_0 H < 12 \text{ T}$) for $H||_c$ [4].

As in the irreversibility line measurements, the current AMSC tapes correlate with the previous results, whereas J_c was significantly reduced at all fields in the current SuperPower tapes. This reduction is caused by the same effect as the T_c -reduction (higher cross-section for neutron absorption), as discussed in the previous section.

In general, J_c in the pristine SuperPower sample is higher than J_c in the AMSC conductors for $H||_{a,b}$. For $H||_c$ on the other hand, J_c of the SuperPower tapes becomes comparable or even smaller than J_c of the AMSC tapes. Due to the greater thickness of the AMSC samples (two and three times thicker for 344C and 344S, respectively) and the larger width (4.4 mm), the engineering current density is always significantly lower in the AMSC samples.

The critical current densities at different temperatures are discussed in the following in more detail. Since the present AMSC tapes 344C and 344S primarily differ by a constant factor, only the 344C tape is shown. Note that J_c is slightly smaller in the 344C tape whereas J_E is 1.4 times higher due to the smaller conductor thickness.

Low temperature ($T=50 \text{ K}$)

- AMSC (figure D.14(a)): For $H||_c$, the critical current density is enhanced in the entire field range after irradiation. At 6.0 T, the critical current density is 1.9 times higher after irradiation and 1.6 times higher at 15 T. For $H||_{a,b}$, J_c is reduced for fields below 4.25 T. At 15 T, J_c is 1.4 times higher after irradiation. The introduction of efficient pinning centres by neutron irradiation clearly dominates at this temperature. The engineering current density ($J_E \approx 0.5 \cdot 10^8 \text{ Am}^{-2}$) for $H||_{a,b}$ is still too small for fusion magnet applications.
- SP (figure D.14(b)): The pristine sample reaches engineering current densities of more than $2 \cdot 10^8 \text{ Am}^{-2}$ at all fields in the favourable field direction ($H||_{a,b}$). This would be sufficient for fusion coils. Unfortunately, J_E does not reach these high values for $H||_c$. Only $0.3 \cdot 10^8 \text{ Am}^{-2}$ at 15 T is found. After irradiation to $1 \cdot 10^{22} \text{ m}^{-2}$, the critical current density at $H||_c$ is only slightly enhanced for fields below 4 T. At 15 T, J_c is only half

D Neutron irradiation

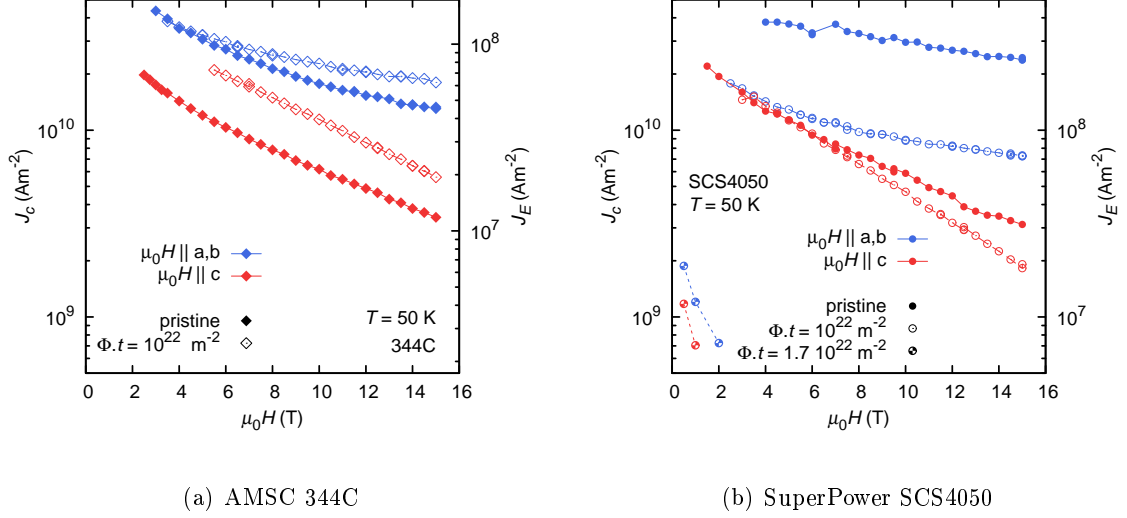


Figure D.14: Critical current densities in the main field orientations at $T=50$ K before and after neutron irradiation

after irradiation. For $H \parallel a,b$, J_c is reduced at all fields. At 4 T and 15 T, J_c is reduced by a factor of 2.6 and 3.4, respectively. As opposed to the AMSC tape, the reduction of T_{irr} by 6.2 K results in a clear reduction of J_c for nearly all fields. At the higher fluence of $1.7 \cdot 10^{22} \text{ m}^{-2}$, the critical currents are reduced by at least one order of magnitude.

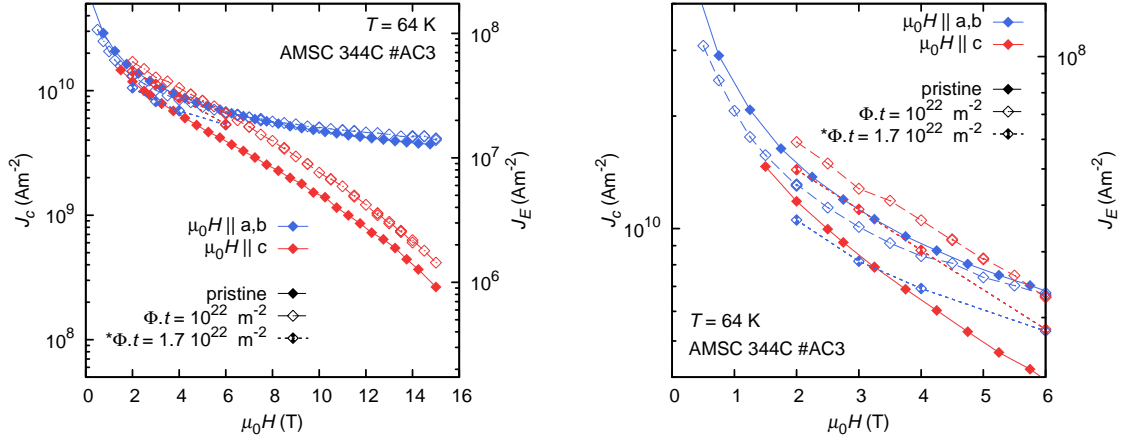
Besides the strong reduction of J_c at $H \parallel a,b$ in the SuperPower tape, the comparable J_c at $H \parallel c$ in both pristine samples is especially striking at 50 K (compare J_c in figure D.14(a) with D.14(b)).

Lowest possible liquid nitrogen temperature ($T=64$ K)

- AMSC (figure D.15): The critical current densities are ≈ 1.5 times higher at all fields ($H \parallel c$) after irradiation up to 10^{22} m^{-2} . For $H \parallel a,b$, J_c is slightly reduced at low fields and slightly enhanced at high fields. The crossover occurs at ~ 6.5 T. At 15 T, the critical current density in the irradiated sample is about 1.1 times higher than in the pristine sample. For lower fields, J_c in the irradiated sample is higher for $H \parallel c$ than for $H \parallel a,b$. The crossover occurs at 6 T. Here, the degradation of the intrinsic pinning due to the displacement of the lattice atoms weakens the intrinsic pinning, whereas the efficiency of uncorrelated pinning is enhanced in the other direction (i.e. $H \parallel c$). This effect occurs at both irradiation levels.

For the higher fluence, J_c is still enhanced for $H \parallel c$, yet less than after the first irradiation step (see figure D.15(b)). Therefore, the fluence optimising J_c is below $1.7 \cdot 10^{22} \text{ m}^{-2}$ at

D Neutron irradiation



(a) Entire experimental field range

(b) Intermediate field range

Figure D.15: AMSC 344C: Critical current densities in the main field orientations at $T=64$ K before and after neutron irradiation at $T=64$ K. Panel (b) shows the intermediate field range in more detail.

64 K. At low fields, J_c is always higher for $H \parallel c$, but a crossover seems to happen at 6 T similar to the lower fluence.

At $H \parallel a,b$, the critical current density reaches only 0.7 to 0.78 times the initial value at 2 T and 6 T, respectively. The red curve in figure D.20(b) on page 106 shows the crossover situation where $J_c(H \parallel c)$ becomes comparable with $J_c(H \parallel a,b)$ at the higher fluence.

- SP (figure D.16(a)): At 64 K, the critical current densities for all field orientations and fields are reduced in the SuperPower tape. The reduction is within the range from 0.77 at 1 T to 0.23 times the pristine J_c at 15 T for $H \parallel c$ and 0.43 at 1 T to 0.27 times the pristine J_c at 15 T for $H \parallel a,b$. Since the temperature of 64 K is closer to $T_c = 86.6$ K after the irradiation, the reduction of J_c is higher than for 50 K. For the highest fluence ($1.7 \cdot 10^{22} \text{ m}^{-2}$ and $T_c = 67.6$ K), the critical current density is smaller by orders of magnitudes and therefore not illustrated (self-field $J_c = 6.75 \cdot 10^7 \text{ Am}^{-2}$).

Boiling temperature of liquid nitrogen ($T=77$ K)

- AMSC (figure D.17): After irradiation to $1 \cdot 10^{22} \text{ m}^{-2}$, the critical current densities for $H \parallel c$ are slightly enhanced for fields above 1.5 T, whereas at lower fields J_c is slightly reduced (see figure D.17(b)). At ~ 6 T, J_c of the pristine and the irradiated sample is similar for $H \parallel c$. From the irreversibility line (figure D.12(b) on page 98), one can

D Neutron irradiation

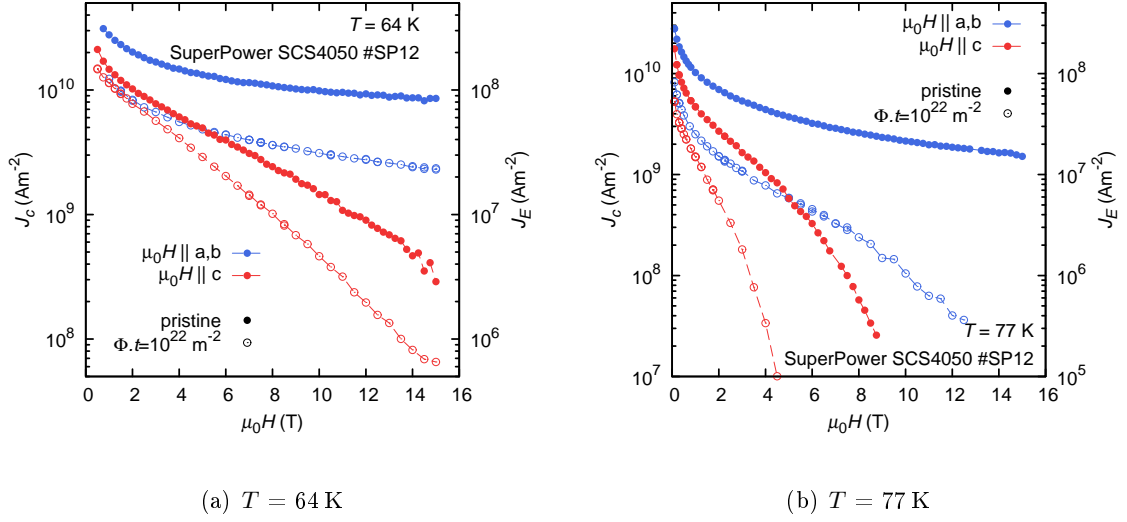


Figure D.16: SuperPower SCS4050: Critical current densities in main field orientations at (a) $T=64$ K and (b) $T=77$ K before and after neutron irradiation.

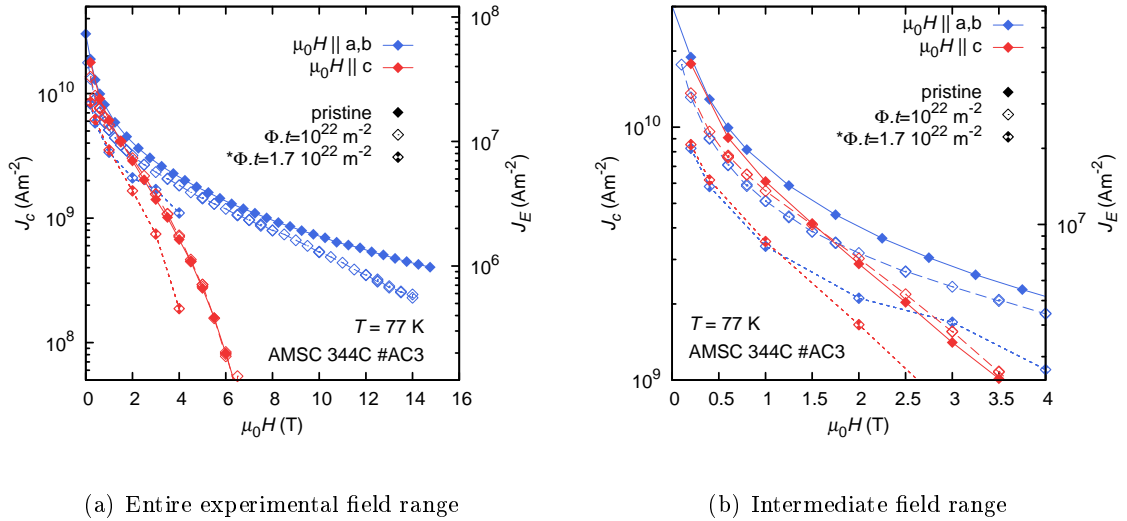


Figure D.17: AMSC 344C: Critical current densities in the main field orientations at $T=77$ K before and after neutron irradiation. Panel (b) shows the intermediate field range in more detail.

D Neutron irradiation

evaluate a slightly enhanced $B_{irr}(77\text{ K})$ for $\Phi \cdot t = 1 \cdot 10^{22} \text{ m}^{-2}$, indicating a higher pinning efficiency. This enhancement is not as pronounced as at $T = 64\text{ K}$ and therefore the effect of the lower T_c more or less cancels the enhancement of B_{irr} at this temperature, leading to a more or less similar J_c before and after irradiation. For $H||a,b$, the critical current density is reduced at all fields. The critical current density is 0.72 and 0.52 times the pristine values at 0.2 T and 15 T, respectively.

After irradiation to $1.7 \cdot 10^{22} \text{ m}^{-2}$, the critical current density is reduced for all fields. This is again evident from the irreversibility line (figure D.12(b)), because $B_{irr}(77\text{ K})$ and $T_{irr}(B)$ are smaller at this fluence level. The reduction is stronger for high fields than for low fields.

- SP (figure D.16(b)): All critical currents are reduced after irradiation. For $H||c$, J_c of the irradiated sample (10^{22} m^{-2}) ranges from 0.30 at 0.1 T to 0.032 times J_c of the pristine tape at 4 T. The irreversibility field $B_{irr}(77\text{ K})$ is also reduced from 9.2 T to 5.8 T after the irradiation (figure D.13(b)). For $H||a,b$, J_c is reduced to 0.30 times of the pristine sample J_c at 0.1 T and to 0.023 times of the pristine sample J_c at 12 T.

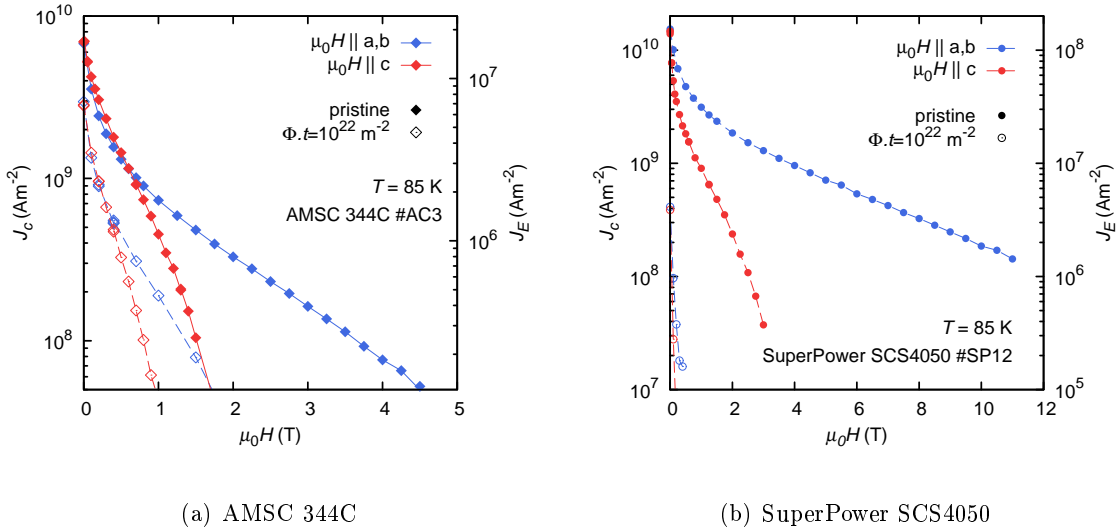


Figure D.18: Critical current densities in the main field orientations at $T=85\text{ K}$ before and after neutron irradiation.

Elevated temperature ($T=85\text{ K}$)

- AMSC (figure D.18(a)): At 85 K, J_c is reduced for all fields. Note that 85 K is already close to the critical temperature and therefore $B_{irr}(85\text{ K})$ is reduced after irradiation as well. The irreversibility field $B_{irr}(85\text{ K})||c$ evaluated from figure D.12(b) is 2.0 T

D Neutron irradiation

and 1.35 T for the pristine and the irradiated sample, respectively. For $H\parallel a,b$, the irreversibility field at 85 K was reduced from 4.9 T to 3.1 T after irradiation. The reduction of $B_{irr}(85\text{ K})$ and T_c results in reduced critical current densities for all fields in both field directions.

- SP (figure D.18(b)): For $H\parallel c$, the irreversibility field at 85 K is reduced from 3.6 T to 0.4 T. Therefore, small critical current densities were only measured at very low fields after irradiation. For $H\parallel a,b$, the drop of $B_{irr}(85\text{ K})$ was even more significant. B_{irr} is reduced from $\approx 17\text{ T}$ before irradiation to 0.7 T after irradiation. This strong reduction of T_c is also responsible for the large reduction of J_c .

D.3.3 Anisotropy at intermediate fields (0 to 6 T)

The samples SP15 (SCS4050), SPAP1 (SCS4050-AP) and AC4 (344C) were used for J_c -anisotropy measurements in the 6 T set-up. All samples were measured before and after irradiation to $\Phi \cdot t = 1.7 \cdot 10^{22}\text{ m}^{-2}$.

Figure D.19 shows the different angular dependence of J_c in the pristine samples at 6 T and 2 T at 64 K. At 6 T, both SuperPower tapes have more or less the same performance at

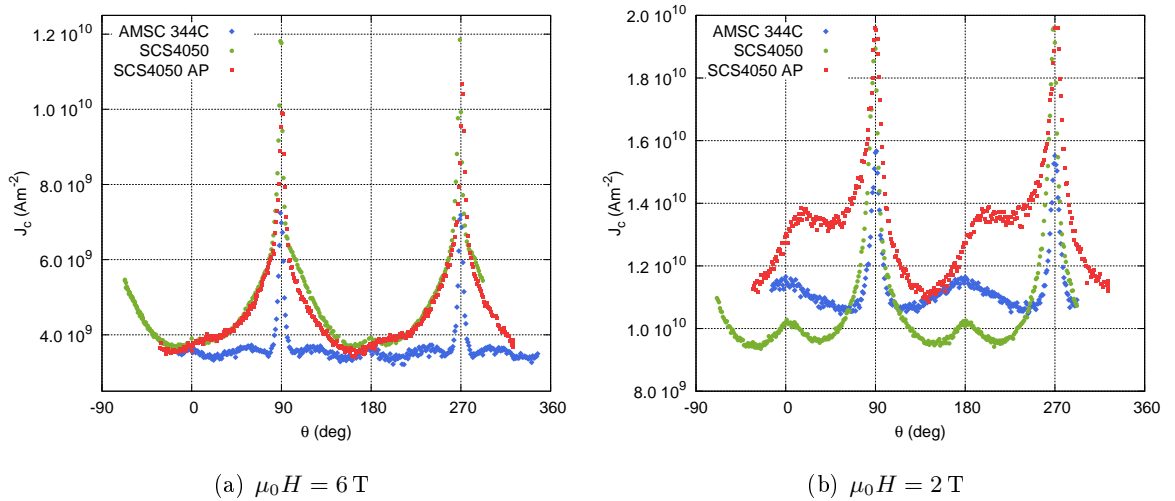


Figure D.19: Angular dependence of the pristine tapes.

64 K. J_c is about 1.2 times higher in sample SCS4050 for $H\parallel a,b$. The reason for this could be a small discontinuity of the CuO-planes due to the c-axis oriented BZO nano-columns in the SCS4050-AP conductor. Therefore, the intrinsic pinning is less effective. The AMSC tape reaches the J_c values of the SuperPower tapes for fields around $H\parallel c$, but not for other field directions. Therefore, the anisotropy is the lowest for the AMSC tape. This low anisotropy indicates a strong over doping of the RE-content in the superconducting layer, which forms un-

D Neutron irradiation

correlated nano-dots during the MOD process, as found in [13]. The AMSC and the SCS4050 tape are completely symmetrical with respect to the c-axis (0° and 180°) at 6 T. The AP-tape on the other hand has a slight asymmetry.

At 2 T, the SCS4050 tape shows the highest anisotropy of all three tapes due to the negligible contribution of uncorrelated pinning centres, which are effective at intermediate and low fields in other tapes. The intrinsic pinning peak occurs clearly, as well as the c-axis peak, which originates from the aligned defects (twin boundaries, dislocations, ...). The SCS4050-AP tape has a smaller anisotropy, but the artificial pinning centres seem to be aligned in preferred directions, leading to a maximum at around 20° (200°). Contrary to the SCS4050-AP, the artificial pinning centres in the 344C tape enhance the properties at all field orientations, which also leads to the lowest anisotropy of the three tapes at 2 T. Note that the angle between the maxima of the SuperPower tapes is not exactly 180° at low fields (< 1 T). This effect is discussed in more detail in section D.4.4. Above a crossover field [63], the intra-granular currents mainly determine J_c and therefore asymmetry effects are hard to find at $\mu_0 H = 6$ T.

Anisotropic properties change significantly due to the irradiation. Figure D.20 shows the changed angular dependence for two different temperatures of the AMSC tape.

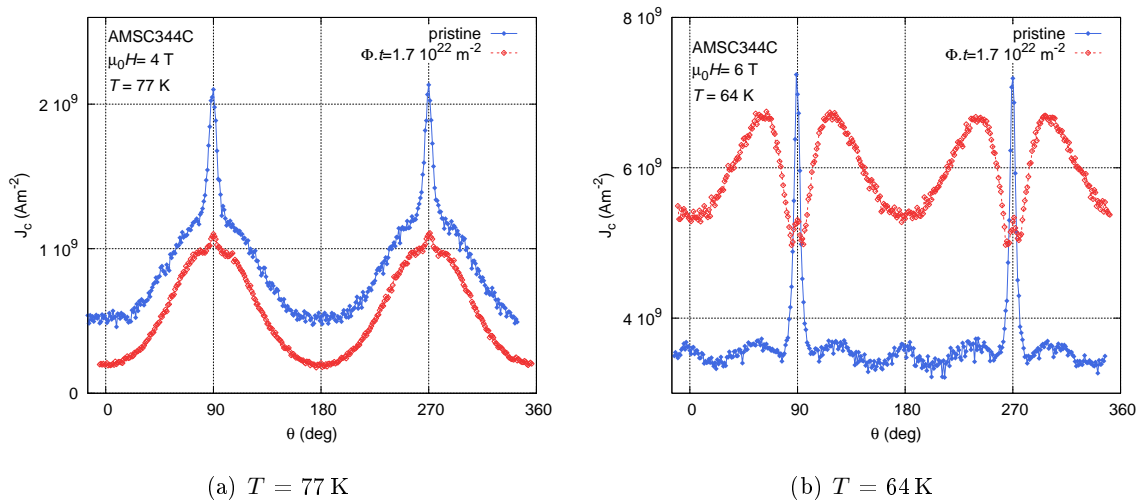


Figure D.20: AMSC 344C: Anisotropy before and after irradiation.

At 77 K and 4 T, the artificial pinning centres in the AMSC tape are not as effective as at low fields and therefore the anisotropy is higher in the pristine samples. This situation does not change after irradiation. The introduced defect structure hardly competes with the consequence of the T_c reduction at these elevated temperature. $B_{irr}(77\text{ K})$ is more or less the same before and after irradiation (extrapolated from $H||c$ in figure D.12(b) on page 98). This results in a slight reduction of J_c at all field angles. The a,b-peak is significantly weaker due to the introduced disorder.

D Neutron irradiation

At 64 K and 6 T, one can see the high efficiency of the introduced uncorrelated pinning centres. J_c is enhanced at all angles, expect close to $H\parallel a,b$. This applied field (6 T) corresponds to the crossover in figure D.15 on page 102, where J_c for $H\parallel c$ becomes as high as for $H\parallel a,b$. At a lower fluence, $J_c(H\parallel c)$ is expected to be even higher than $J_c(H\parallel a,b)$ (according to figure D.15).

Direct comparisons similar to figure D.20 are not possible for the SuperPower tape, since the J_c reduction was too strong.

Each sample will be discussed in detail in the following sections.

SuperPower SCS4050

J_c in the pristine sample (figure D.21) is asymmetric with respect to the c-axis at 64 K and 77 K for low fields. This asymmetry may be caused by tilted planes of GdO_2 precipitates. Due to the absence of BZO nano-columns, the anisotropy is higher than in the SCS4050AP

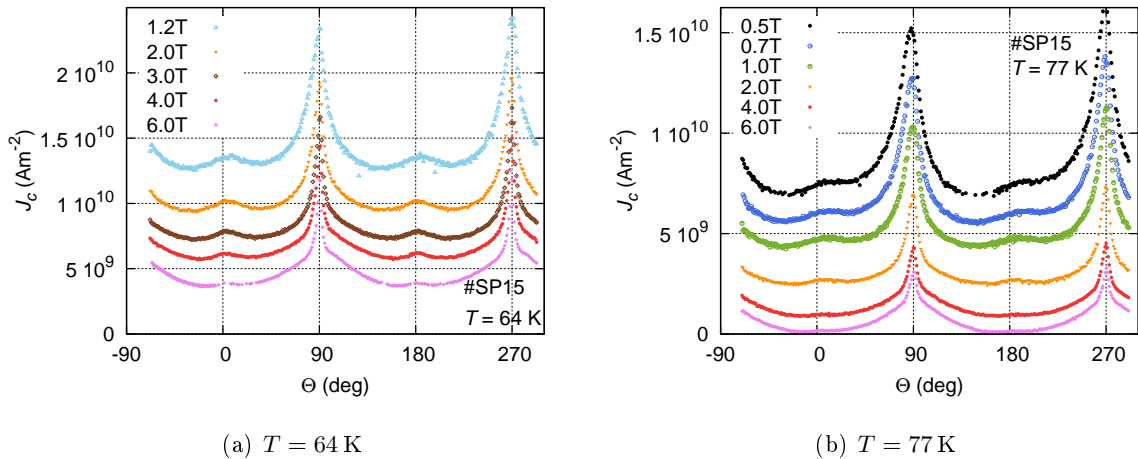


Figure D.21: Angular dependence of the pristine SuperPower SCS4040 tape.

sample for all fields and temperatures. Because of the gadolinium, J_c is reduced by two orders of magnitude ($T_c=68.6$ K) in the irradiated sample. Figure D.22 shows an anisotropy measurement at $T = 50$ K. The critical current density is symmetric to the c-axis even at low fields. No local minima close to the a,b-peaks occur after irradiation at this temperature as T/T_c is still too high.

SuperPower SCS4050AP

The data of the pristine SCS4050AP sample are highly asymmetric at $T = 64$ K and $T = 77$ K at low fields (figure D.23). The nano-columns seem to be correlated and the local maximum in J_c shifts by 20° - 30° from the c-axis. At elevated fields, the BZO nano-columns and the (RE)O₂ nano-participates become ineffective and the angular dependence of J_c is similar to

D Neutron irradiation

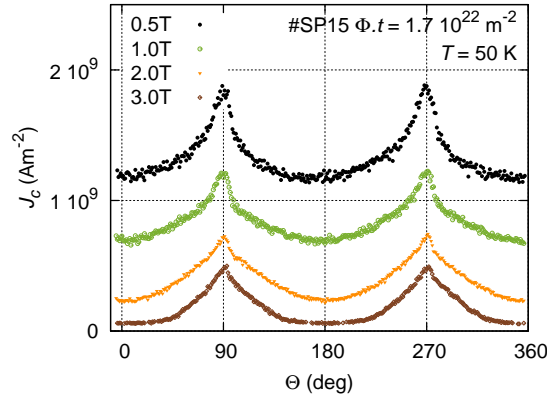


Figure D.22: Angular dependence of the irradiated SuperPower SCS4050 tape.

that in a tape without BZO nano-columns (SCS4050).

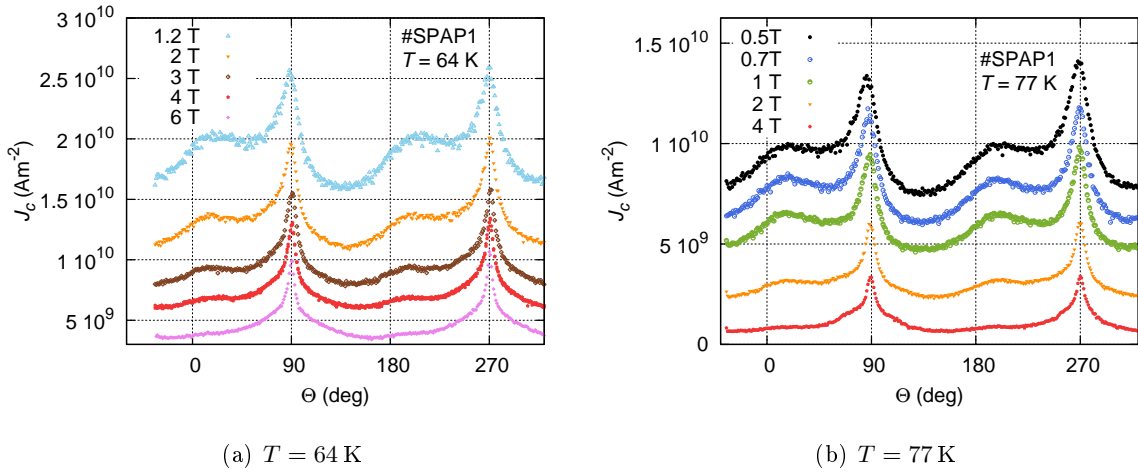


Figure D.23: Angular dependence of the pristine SuperPower SCS4050-AP tape.

After irradiation (figure D.24), J_c is reduced by one order of magnitude at 64 K ($T_c=77.4$ K). The degradation is not as pronounced as in the SCS4050 conductor, as yttrium has only partially been substituted by gadolinium. At 64 K, the a,b-peak is wider than before the irradiation but the anisotropy is not significantly reduced unlike at 50 K where a reduction of the anisotropy is clearly visible.

AMSC 344C

The pristine AMSC tape has a very low J_c -anisotropy at low fields (figure D.25). The RE_2O_3 nano-particles are mostly uncorrelated since no distinct local maximum occurs besides the

D Neutron irradiation

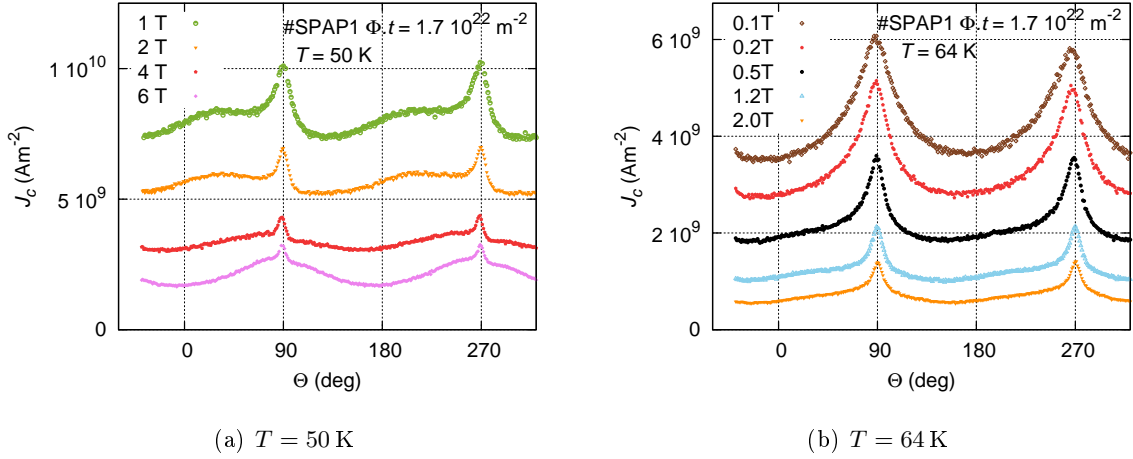


Figure D.24: Angular dependence of the irradiated SuperPower SCS4050-AP tape.

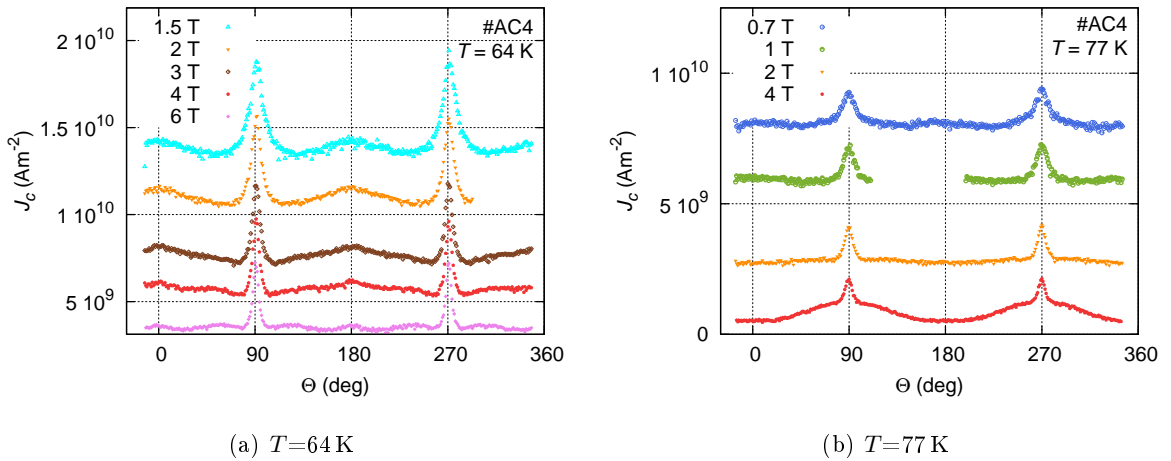


Figure D.25: Angular dependence of the pristine and irradiated AMSC 344C tape. Note, that for field angles between 90° and 180° the temperature was not stable for $\mu_0 H = 1 \text{ T}$ in (b). Hence, the data were omitted in this angular range.

D Neutron irradiation

intrinsic peak. The angular J_c -dependence is always symmetrical. At 64 K the J_c -anisotropy is higher than at 77 K for the same fields and a c-axis-peak is visible. Hence, at low temperatures the nano-dots are not as effective as at high temperatures compared to the intrinsic pinning.

At 64 K (figure D.26(a)), a local maximum develops between fields parallel and perpendicular to the a,b-planes at high fields after irradiation and the currents are smallest close to $H||a,b$ at 3 T and 4 T. At 6 T, the critical current density at $H||c$ equals the critical current

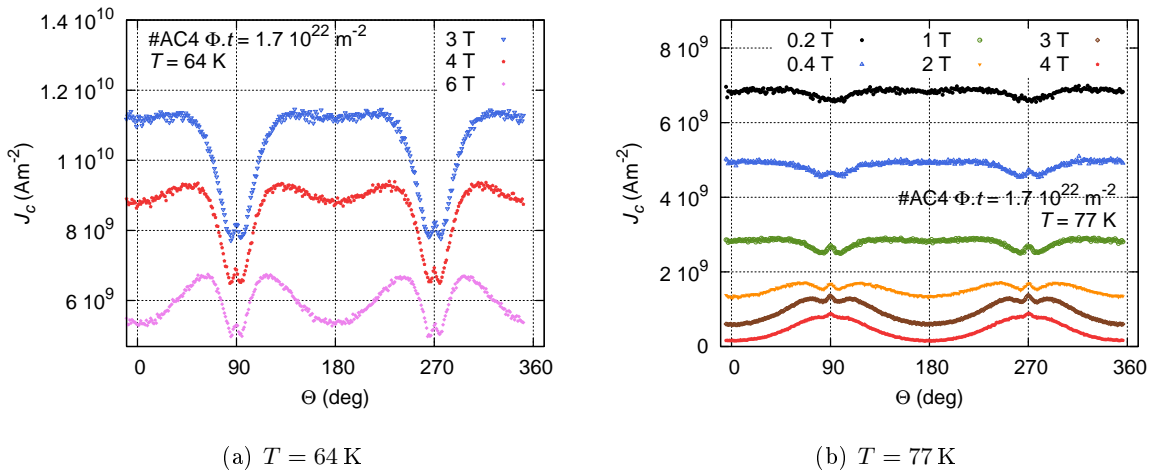


Figure D.26: Angular dependence of the irradiated AMSC 344C tape.

density at $H||a,b$ (see figure D.15(b)). One can conclude from figure D.15 that at even higher fields the intrinsic pinning would again dominate as at 77 K at high fields (figure D.26(b)).

At 77 K (figure D.26(b)), the maximum of the angular dependent J_c occurs around the c-axis for low fields. At higher fields, a local minimum develops once more at the c-axis position. The crossover, where $J_c(H||c)$ becomes smaller than $J_c(H||a,b)$ is also somewhere between 1 T and 2 T (see figure D.17(b)).

D.4 Results and discussion of tensile stress measurements

In BSCCO tapes, the linear dependence of I_c with stress/strain was entirely explained by the pressure dependence of the critical temperature (T_c) [64]. Due to the dependence of I_c on T/T_c (see left part of equation D.9), the sensitivity on stress/strain also changes with temperature. For temperatures close to T_c , the I_c -sensitivity is stronger. Furthermore, the relative change of I_c with stress/strain increases with applied magnetic fields in BSCCO. Additionally, the in-plane stress/strain dependence in BSCCO is isotropic.

The correlation between pressure dependence (T_c dependence) and applied stress/strain is

D Neutron irradiation

more difficult if the in-plane strain dependence of I_c becomes anisotropic as in (RE)BCO. In YBCO single crystals, T_c increases linearly with pressure along the b-axis (1.9 ± 0.2 K/GPa) and decreases with pressure along the a-axis (-2.0 ± 0.2 K/GPa) [65]. Hence, twin boundaries² and in-plane misalignments change the stress/strain dependence. The microscopic structure has to be considered in order to understand the macroscopic behaviour. A qualitative correlation between the uni-axial pressure dependence of T_c and the reversible stress/strain-effect was found in [26]. Figure D.27 shows two different situations in YBCO thin films.

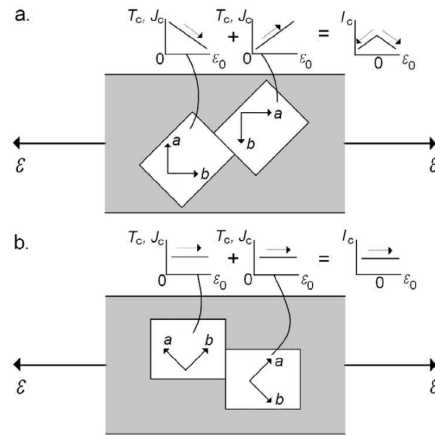


Figure D.27: Explanation of the I_c strain dependence in IBAD-MOCVD (RE)BCO coated conductors, taken from [26]: (a) Twin boundaries are oriented at 45° to the superconducting film. (b) Twin boundaries perpendicular to the tape direction when stress/strain is applied along the superconducting film.

The situation in D.27(a) corresponds to the alignment of the a,b-planes in IBAD-MOCVD (RE)BCO coated conductors (as the SuperPower tape in this work). The a-axis or b-axis is oriented parallel to the tape axis. A current flowing from left to right first flows parallel to the b-axis, but parallel to the a-axis after passing the twin boundary. If stress/strain is applied along the tape direction, T_c and therefore J_c decreases in the left grain and increases in the right grain, as indicated in the inserts. In other words, up to the optimum stress/strain state the right grain limits I_c and afterwards the left grain limits I_c .

If the a- and b-axes of the unit cells are tilted by 45° to the tape direction as in ISD (Inclined-Substrate Deposition) (RE)BCO coated conductors, the opposite T_c - σ/ϵ dependencies cancel each other in each grain and the critical current is no longer sensitive to the stress/strain.

Both situations were measured in [26]. Note that the situation in D.27(b) would also occur, if stress/strain was applied at an angle of 45° to an IBAD-MOCVD conductor. This would have a positive effect in IBAD-MOCVD twisted cables [26].

Note that dislocations on the other hand can introduce a relatively large amount of stress/-

²Neighbouring lattices which are rotated by 90° in the a,b-plane.

D Neutron irradiation

strain and therefore change the initial lattice stress/strain state.

Of further interest is the lower strain sensitivity of GdBCO coated conductors, which was found to be 58% smaller than in YBCO coated conductors [26].

Until now, no tensile stress measurements on irradiated coated conductors have been reported. Therefore, no reference data existed before these measurements were started. Tensile stress measurements on pristine coated conductors show that tensile stress can be applied up to the irreversible stress/strain-limit ($\sigma_{irr}/\varepsilon_{irr}$) without a permanent reduction of the critical current once the stress has been released. On the contrary, as previously mentioned, an ideal stress/strain exists, where a maximum of the critical current is expected.

Due to the missing reference data for irradiated samples and the prototype-status of our set-up, all measurements were performed with high resolution (i.e. in small intervals of angle, field and forces). Therefore, the full characterisation of a sample took about two months (see section D.2.4). Since the measurements on one sample were always terminated when the irreversible region was entered, the sample was damaged and could no longer be used. Hence, in contrast to the transport and anisotropy characterisation, the measurements before and after irradiation could not be performed on exactly the same sample, but on different samples cut from one long piece of a tape.

In particular tensile stress measurements, generally require statistics from many measurements. Note that our results refer to only one sample of each manufacturer, in order to keep the total effort compatible with the available time.

In the following, the irreversible stress/strain limit ($\sigma_{irr}, \varepsilon_{irr}$) is defined as the last stress/strain before I_c in the relaxed state is reduced to 95% of the initial value. The exact irreversible limit of the pristine AMSC 344C tape was not determined, as the sample reached the irreversible limit between two anisotropy measurements at 303 MPa. Hence, only lower limits of the irreversible parameters can be given for this sample.

D.4.1 Stress-strain dependence

The stress-strain dependence was measured at the same time as the self-field I_c - dependence on the stress (between the anisotropy measurements).

SuperPower SCS4050

Figure D.28 shows results for the SuperPower tapes. Right from the beginning, the applied stress led to a permanent deformation in both samples. The yield strength of the substrate (Hastelloy) is 700 MPa at 76 K [66] which correlates to a stress of 347 MPa in the SCS4050 tape. The yield strength is significantly lower than the irreversible stress limit, and therefore, the deformation occurs early in our measurements. A reduction of this deformation

D Neutron irradiation

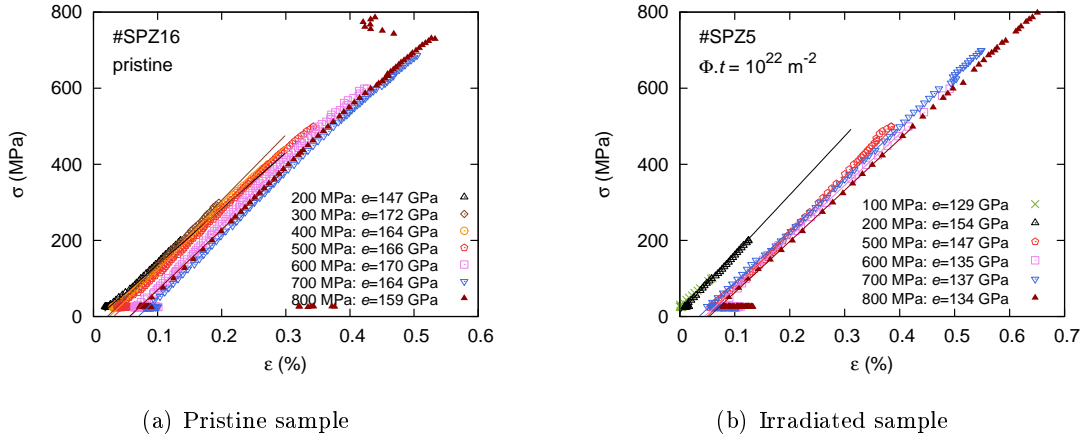


Figure D.28: Stress strain dependence of the SuperPower tape. Different symbols mark different measurements labelled by the maximum of the applied stress after each measurement.

was always observed after heating the sample to room temperature. The Young's modulus or E-modulus (e) of all measurements was evaluated and the results are shown in the legends of the figures. Straight lines mark the fitted linear dependency ($e \cdot \epsilon$).

The maximum deformation was about 0.5% before internal cracks released stress from the pristine sample, which led to a higher strain after relaxing (figure D.28(a)). After the first cracks occurred, the strain without applied stress was higher than 0.3%. The cracks occurred at an applied stress of 740 MPa in this sample. The fitted³ E-modulus in this sample varied between 147 GPa and 172 GPa with a mean value of 163 MPa. These data are similar to values from literature for this sample. The irreversible stress limit was specified to be >550 MPa by the manufacturer. The real limit was significantly higher in our samples.

In the irradiated sample, up to 800 MPa, no significant jump of the strain occurred after relaxing. The highest deformation of the sample was about 0.14% after applying 800 MPa. The fitted E-modulus varied between 129 GPa and 154 GPa with a mean value of 139 GPa. Therefore the measured E-modulus changed to a lower value after irradiation.

Note that the measurements for maximum applied stresses of 300 MPa and 400 MPa were not usable due to ice formation on the pull rod. Therefore, these measurements are not illustrated in figure D.28.

AMSC 344C

Figure D.29 shows the stress-strain dependence of the AMSC 344C conductor. Similar to the

³The lower margin of the fit was always 50 MPa and the upper margin was the maximum applied stress of the previous measurement (e.g. 100 MPa for the 200 MPa measurement).

D Neutron irradiation

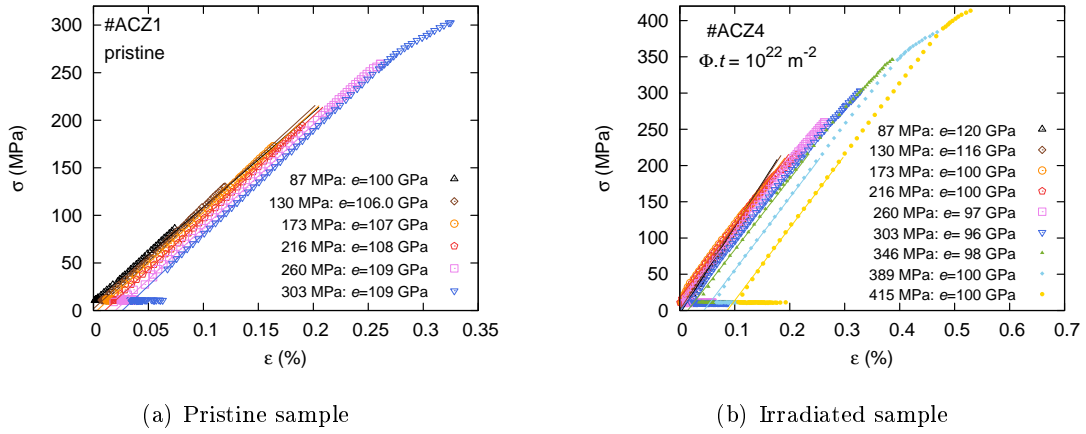


Figure D.29: Stress strain dependence of the AMSC tape. Different symbols mark different measurements labelled by the maximum of the applied stress after each measurement.

SuperPower tapes, the early irreversible deformation was partially cured after heating to room temperature. The yield strength of the substrate (Ni-5at%W) was reported to be 260 MPa [66] at 76 K which correlates to a stress of 84 MPa in the AMSC 344C tape. The yield strength is significantly lower than the irreversible stress limit and, therefore, the deformation once again occurs early in our measurements. The pristine sample (figure D.28(a)) was irreversibly damaged between two anisotropy measurements and therefore only a lower limit of 303 MPa and 0.33% respectively, was determined as irreversible stress and strain limits. The E-modulus varied from 100 GPa to 109 GPa with a mean value of 106 GPa.

The maximum tolerable tensile stress for this sample was specified to be 150 MPa at room temperature by the manufacturer. This value includes a broad safety margin, as our samples were able to withstand at least twice the rated irreversible stress at liquid nitrogen temperatures. In [67] the irreversible strain limit for a similar sample was found to be 0.38% and the E-modulus of the initial slope was 132 GPa.

The irradiated sample (figure D.29(b)) was loaded up to the irreversible limits, which were $\sigma_{irr} = 410$ MPa and $\varepsilon_{irr} = 0.53\%$, respectively. Once more, the irreversible limits are significantly higher than specified by the manufacturer. The E-modulus at higher applied stress varied at around 100 GPa and was therefore slightly lower than in the pristine sample.

D.4.2 Self-field critical current (I_c)

SuperPower SCS4050

In the relaxed state, the critical current in self-field (I_{c0}) of the irradiated sample was about 12% of I_{c0} in the pristine sample. Detailed absolute values are reported in table D.4 on page

D Neutron irradiation

117. Figure D.30(a) shows the change of I_c in the absence of an applied field.

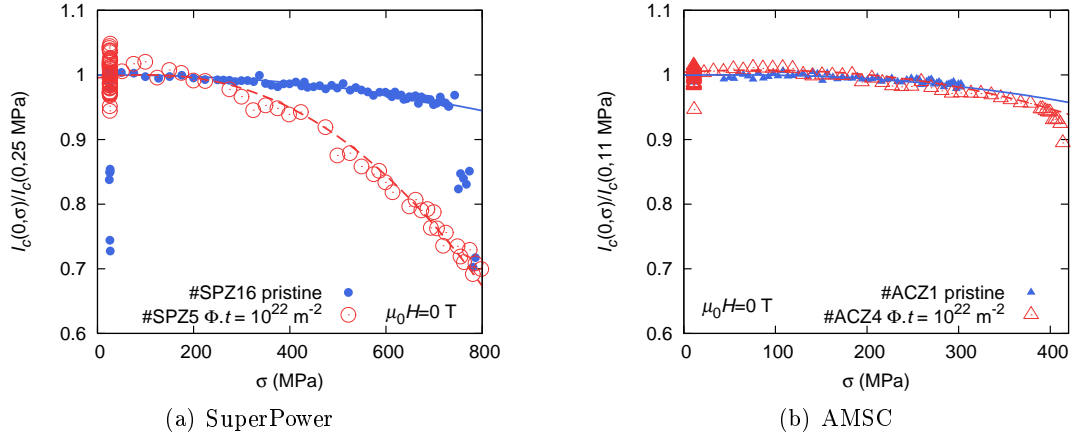


Figure D.30: Stress dependence of the self-field critical current in all measured tapes. The critical currents are normalised by the self-field critical current in the relaxed state I_{c0} (see table D.4 on page 117).

After applying 740 MPa/ $\varepsilon=0.55\%$, the critical current was permanently reduced in the pristine sample. Two major cracks occurred between 740 MPa and 800 MPa. After the initial reduction, I_c was further reduced to 120 A ($\approx 0.83 I_{c0}$) and the remaining strain on the sample after releasing the stress was above 0.3% as previously shown in figure D.28. After applying 790 MPa a second crack reduced I_c to 105 A ($\approx 0.7 I_{c0}$). It was not possible to determine the irreversible destruction via optical inspections, but magnetoscan imaging showed the localised destruction of the superconducting layer, as will be shown in the next section. At the irreversible stress limit of 740 MPa, I_c was only reduced to 95%. Note that measurements of other pristine SCS4050 samples from the same batch showed irreversible limits of stress up to 800 MPa (not shown in this work).

For the irradiated sample, the irreversible stress/strain limit was reached at 800 MPa/ $\varepsilon=0.65\%$. The irradiated sample has greater sensitivity to applied stress than the pristine sample. Close to the irreversible stress limit of 790 MPa, I_c was reduced to 67%. Neutron irradiation didn't influence the irreversible stress/strain limits, whereas the stress/strain-sensitivity of I_c was significantly enhanced. This effect could be explained by the lower T_c and therefore a higher T/T_c ratio in the irradiated tape at 77 K. As previously mentioned, a higher sensitivity for temperatures closer to T_c was found in BSCCO tapes in [24].

AMSC 344C

Figure D.30(b) shows the stress dependence of I_c in the AMSC conductor. The sensitivity of I_c does not change after irradiation at all, but a slight maximum around 100 MPa may exist.

D Neutron irradiation

The pristine sample was irreversibly damaged during the anisotropy measurements at 303 MPa, therefore no data exist for higher stress values. Below 303 MPa ($\varepsilon=0.33\%$), I_c was never reduced to below 98%. I_c of the irradiated sample is reduced to 92% at the irreversible stress limit of 410 MPa ($\varepsilon=0.53\%$).

Note that the absolute I_{c0} was reduced to 76% in the irradiated tape compared to the pristine value.

D.4.3 Homogeneity

Magnetoscan of the pristine samples were performed before and after tensile stress measurements. Before applying stress, both conductors were quite homogeneous with no significant defect (figure D.31(a) and D.32(a)).

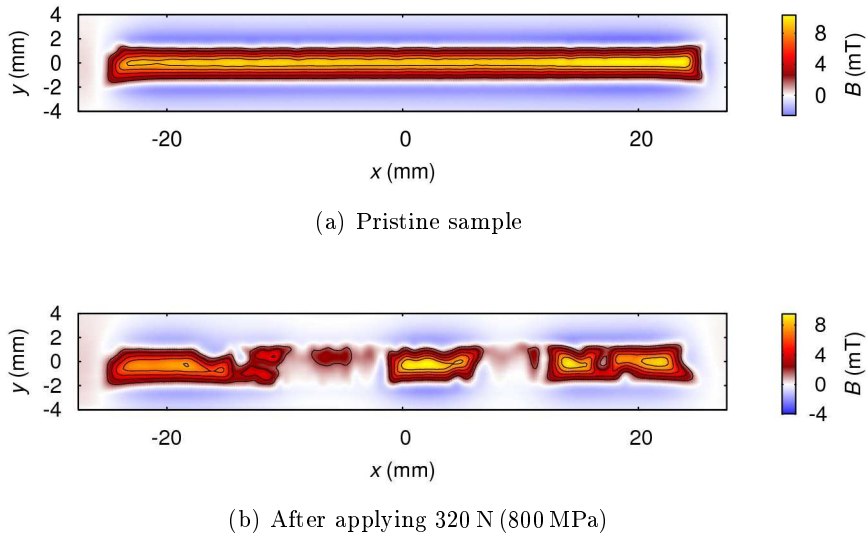


Figure D.31: Magnetoscan of the pristine SuperPower sample before and after the tensile stress measurements.

The pristine AMSC conductor had a slightly lower I_c on the left edge. Since the current contacts were connected over a length of ≈ 15 mm at both edges, this slight I_c reduction can be disregarded.

After applying the maximum load (figure D.31(b) and D.32(b)), both conductors were irreversibly damaged. The superconductor was damaged over a long length and not exclusively along single cracks. In both samples, the centre part (where the voltage contacts and the strain gauge is located) remained nearly intact. The left and right ends, where pressed contacts held the sample, also remained superconducting. Hence, the load of the current terminations does not destroy the sample and good current feed can be ensured.

D Neutron irradiation

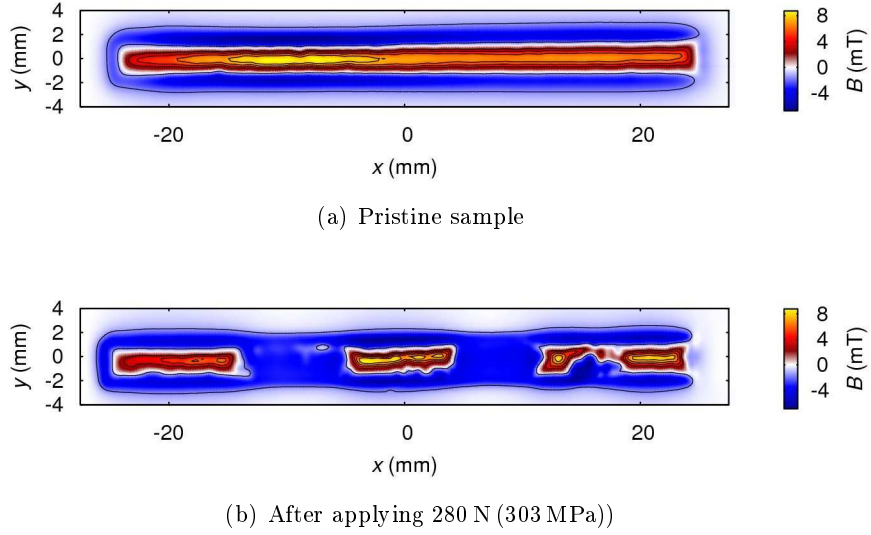


Figure D.32: Magnetoscan of the pristine AMSC sample before and after the tensile stress measurements.

Sample	σ_{irr}	ε_{irr}	$I_{c0}(0T)$	T_{mean}	T_{min}	T_{max}	T_{std}
pristine SP (SPZ16)	740 MPa	0.55 %	142.7 A	77.07 K	76.98 K	77.11 K	0.04 K
irrad. SP (SPZ5)	800 MPa	0.6 %	16.52 A	77.16 K	77.03 K	77.45 K	0.13 K
pristine AMSC (ACZ1)	>303 MPa	>0.33 %	88.4 A	77.27 K	76.93 K	77.47 K	0.16 K
irrad. AMSC (ACZ4)	410 MPa	0.53 %	67.1 A	77.24 K	77.18 K	77.39 K	0.06 K

Table D.4: Summary of the irreversible limits from the self-field measurements.

D Neutron irradiation

D.4.4 Anisotropy

I_c -anisotropy measurements were performed at 0.1 T, 0.2 T, 0.4 T, 0.6 T, 1.0 T and 1.4 T for tensile forces up to 400 N.

For the lowest field ($\mu_0 H=0.1$ T), for an intermediate field ($\mu_0 H=0.6$ T) and for the highest possible applied field ($\mu_0 H=1.4$ T), the critical currents over the whole angular range are summarized in figures D.33 to D.35 and D.39 to D.41 for the SuperPower and the AMSC sample, respectively.

The field was parallel to the tape surface at $\pm 90^\circ$ and perpendicular to the tape surface at 0° . For the SuperPower conductor the left maximum peak ($\approx -90^\circ$) and the right maximum peak ($\approx -90^\circ$) are referred to as Θ_{left} and Θ_{right} , respectively. In the AMSC sample, the peaks are referred to as a,b-peaks, as they are positioned at the classical a,b-peak position of $\pm 90^\circ$.

The colour profile of the 3D figures indicates the relative change of the critical current with regard to I_c at the maximum at about 90° (SuperPower: Θ_{right} or AMSC: Θ_{ab}).

SuperPower SCS4050

The critical currents in the pristine sample at 0.1 T (figure D.33(a)) are asymmetric with respect to the c-axis, due to the tilt of the a,b-plane and/or the Gd_2O_3 precipitates. The

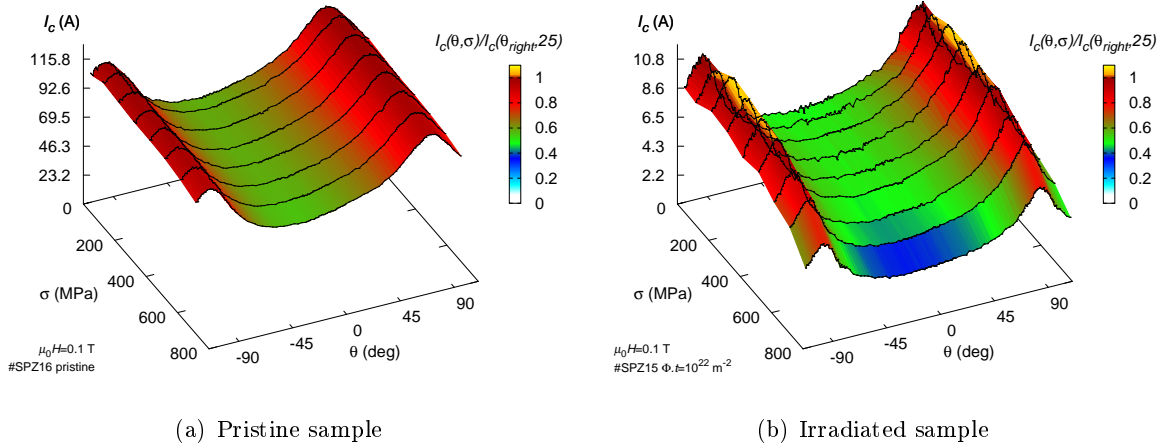


Figure D.33: Anisotropy of the SuperPower tape under tensile stress at $\mu_0 H=0.1$ T.

left maximum is shifted by -11° and the right maximum by -6.5° to the the tape surface in the relaxed state. The minimum is located at around -30° . The ratio between maximum and minimum is about 1.7 and does not change with applied stress. As expected from the self-field measurements, the change that occurs in I_c upon applying tensile stress is rather small. The angular position of the left and right maxima does not change with applied stress.

D Neutron irradiation

The difference between the shift of the two maxima with respect to the tape surface disappears for the irradiated sample at 0.1 T (figure D.33(b)). Both maxima are shifted by about 5.5° to the tape surface in the relaxed state. The asymmetric behaviour changes to a more symmetric one in the irradiated sample. Again I_c^{max}/I_c^{min} does not change with applied stress. It is about 1.8 to 2 and therefore slightly higher than in the pristine sample. The maximum I_c occurs at around 200-300 MPa for all field orientations, which is indicated by the yellow colour in the diagrams (according to a relative enhancement).

At 0.6 T, the critical current of the pristine sample is more symmetric to the c-axis than at 0.1 T (figure D.34(a)). Furthermore, the anisotropy is enhanced. A small local minimum

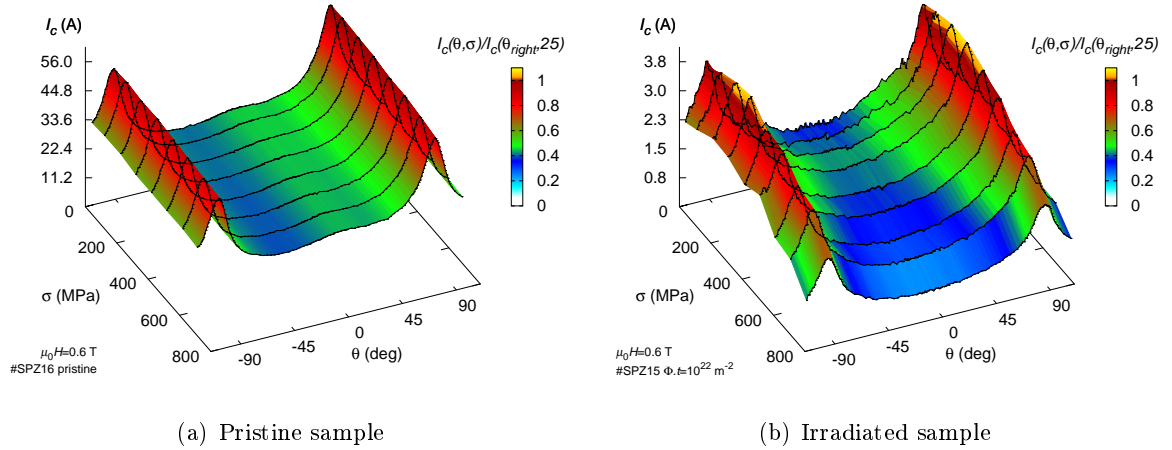


Figure D.34: Anisotropy of the SuperPower tape under tensile stress at $\mu_0 H = 0.6$ T.

occurs at $\approx -35^\circ$ and a small local maximum appears at $\approx 10^\circ$.

The angular dependence of I_c in the irradiated sample is more or less symmetrical to the c-axis (figure D.34(b)). Again, an enhancement of I_c is found at around 200 MPa and the sensitivity on the applied stress is significantly higher than in the pristine conductor.

At 1.4 T (figure D.35), the pristine sample has a slight maximum similar to a conventional c-axis-peak at about 0° . The flux lines are pinned by defects aligned along the epitaxial growth direction. The local minimum at negative angles next to this peak is slightly smaller than the minimum at higher angles. The left maximum is shifted by -4.6° and the right by -3.7° with respect to the tape surface in the relaxed state. The angular dependence of I_c becomes more symmetric at higher fields, as the APCs becomes less effective. The ratio of I_c at the right maximum and at the c-axis-peak is 2.6.

The irradiated sample no longer shows a c-axis-peak at 1.4 T (figure D.35(b)). For both maxima, the shift to the surface is about 4° . The ratio between the right maximum and the

D Neutron irradiation

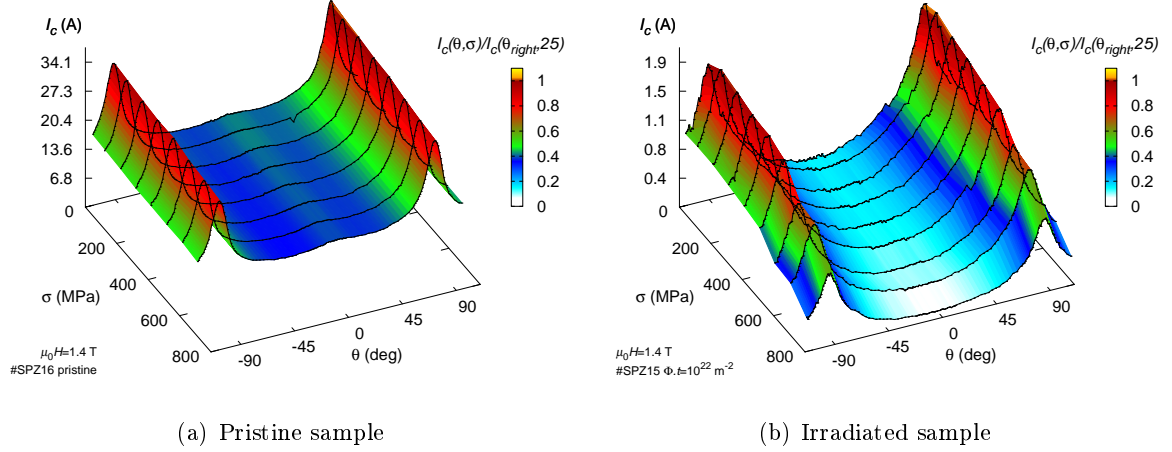


Figure D.35: Anisotropy of the SuperPower tape under tensile stress at $\mu_0 H = 1.4$ T.

minimum located close to 0° is 6.4 indicating a high anisotropy. At 1.4 T, the maximum at about 200 MPa is not observed.

Figure D.36 shows the shift of the maxima with respect to the tape surface, depending on field and stress, in detail. At low fields, the shift of the left maximum is nearly twice as large as

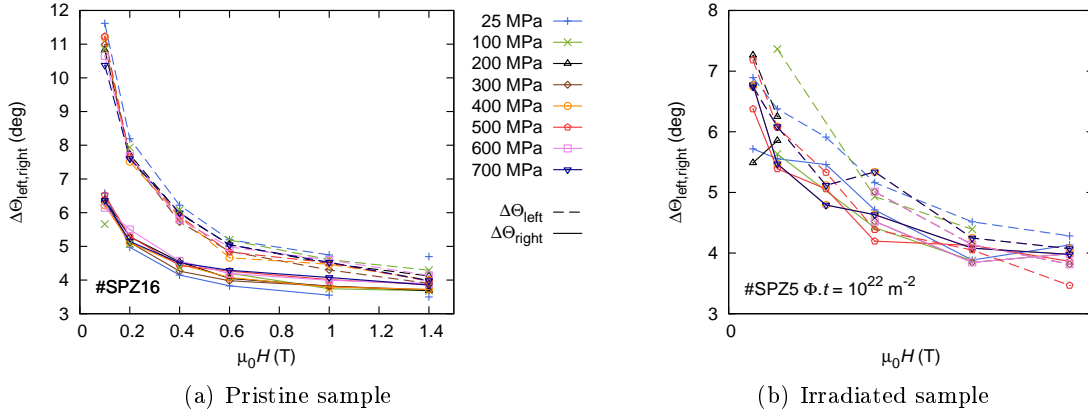


Figure D.36: Peak shift of the left (Θ_{left}) and right (Θ_{right}) maximum with respect to the tape surface. The left peak shifts ($\Delta\Theta_{left}$) are indicated with dashed lines, whereas the right peak shifts ($\Delta\Theta_{right}$) corresponds to the solid lines. The different colours mark different applied stresses.

the shift of the right maximum in the pristine sample (figure D.36(a)). Up to 1.4 T, the shift of both maxima converge to a constant value of about 4° . The decreasing pinning efficiency of the correlated Gd_2O_3 participates explains the shift of the maximum peaks towards their orientation at low fields. The remaining shift of $\approx 4^\circ$ on the other hand is likely to be caused

D Neutron irradiation

by tilted a,b-planes as found in [68]. The difference in the positions of the left and the right peak at low fields is unclear at present.

In the irradiated sample, the difference between both maxima becomes significantly smaller. Nevertheless, the peaks move from $\approx -7^\circ$ (173°) to $\approx -4^\circ$ (176°). Similar to the pristine sample, the peak shift converges at 4° at higher fields, consistent with a tilt of the a,b-planes..

Furthermore, Θ_{right} is always higher than Θ_{left} .

Tensile stress does not influence the angular dependence and therefore the positions of the maxima are also not affected.

As previously found, slightly higher I_c values occur for stresses around 200 MPa in the irradiated samples for fields ≤ 1 T (figure D.33(b) and figure D.34(b)). A more detailed analysis was performed for various fields parallel to the right maxima and for $H \parallel c$ (0°). Figure D.37 and D.38 show the results.

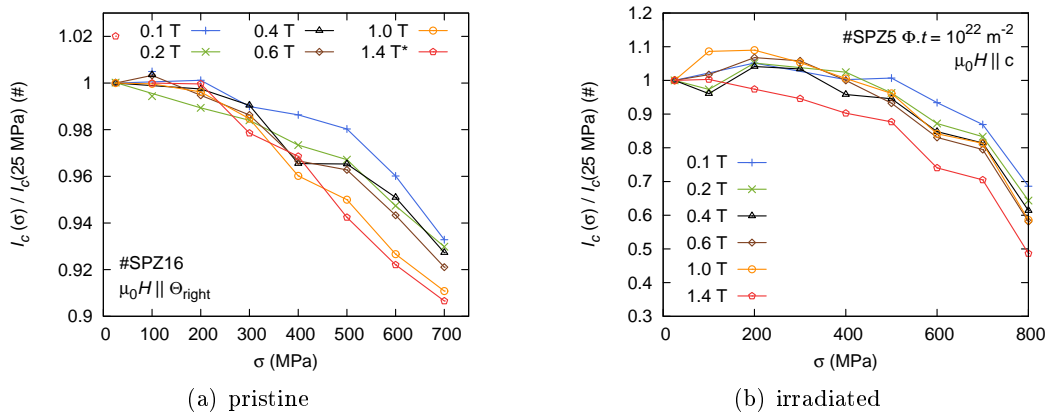


Figure D.37: Stress dependent I_c reduction for various fields parallel to the right maximum peak ($H \parallel \Theta_{right}$). In the pristine sample I_c at 1.4 T was normalised by the I_c -value at 100 MPa, since the temperature was too low during the 25 MPa measurement.

In the pristine sample, I_c is reduced slightly more for $H \parallel \Theta_{right}$ (figure D.37(a)) than for $H \parallel c$ (figure D.38(a)) with increasing field. I_c is reduced to 90% of $I_{c,0}$ at 700 MPa, 1.4 T and $H \parallel \Theta_{right}$. With increasing field the stress dependence of I_c becomes stronger. A similar field dependence was also found in YBCO coated conductors for $H \parallel a,b$ [69].

After irradiation (figure D.37(a)), I_c is reduced to 50% of $I_{c,0}$ at 800 MPa, 1.4 T and $H \parallel \Theta_{right}$. A maximum of the critical current occurs at around 200 MPa for all fields except for the highest applied field of 1.4 T. Furthermore, the highest reduction of I_c is observed at 1.4 T and I_c decreases monotonously with field.

Contrary to $H \parallel \Theta_{right}$, the lowest reduction of I_c occurs at an intermediate field of 0.4 T

D Neutron irradiation

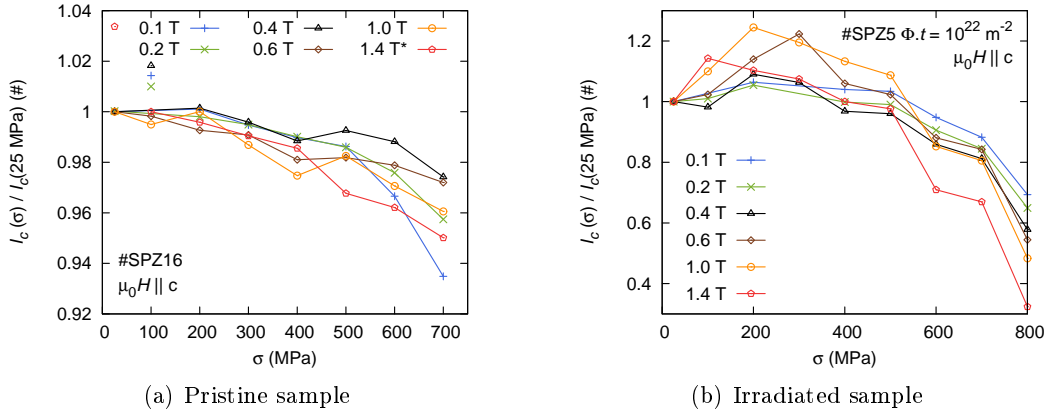


Figure D.38: Stress dependent I_c reduction for $H||c$. In the pristine sample, I_c at 1.4 T was normalised by the I_c -value at 100 MPa, since the temperature was too low during the 25 MPa measurement.

for $H||c$ in the pristine sample (figure D.38(a)). For lower and higher fields the I_c degradation is stronger. A similar behaviour for $H||c$ was found with a maximum I_c at 0.25 T in YBCO conductors [69].

The critical current of the irradiated sample reaches a maximum at an applied stress of 200-300 MPa (figure D.38(b)). At intermediate fields (0.6 T and 1.0 T), significantly higher values of I_c are reached at 200 MPa. On the other hand at higher applied stresses, the critical currents are monotonously reduced with field. Once again, the reduction of I_c is significantly higher in the irradiated sample.

AMSC 344C

Unlike SuperPower tapes, the I_c -angular dependence of the AMSC tape is always symmetric with respect to the c-axis. The APCs introduced during the MOD process form nano-dots, as shown by TEM images [13]. These nano-dots are mostly uncorrelated since the a,b-peak is parallel to the tape surface for all fields and no further maxima appear. As previously explained, the AMSC APCs are very efficient at low fields.

At 0.1 T (figure D.39(a)), only a slight angular I_c -dependence is observed in the pristine sample. Similar to the self-field tensile stress dependence, I_c does not change with applied forces. The critical currents of the irradiated sample (figure D.39(b)) are reduced to $\approx 70\%$ compared with the pristine values. A very slight enhancement of I_c between $H||a,b$ and $H||c$ was observed in the irradiated sample.

At an intermediate field of 0.6 T, the pristine sample has small maxima for $H||a,b$ (figure D.40(a)) and no significant I_c reduction with applied stress. The irradiated sample on the other hand has a clear global maximum for $H||c$, due to the introduced pinning centres.

D Neutron irradiation

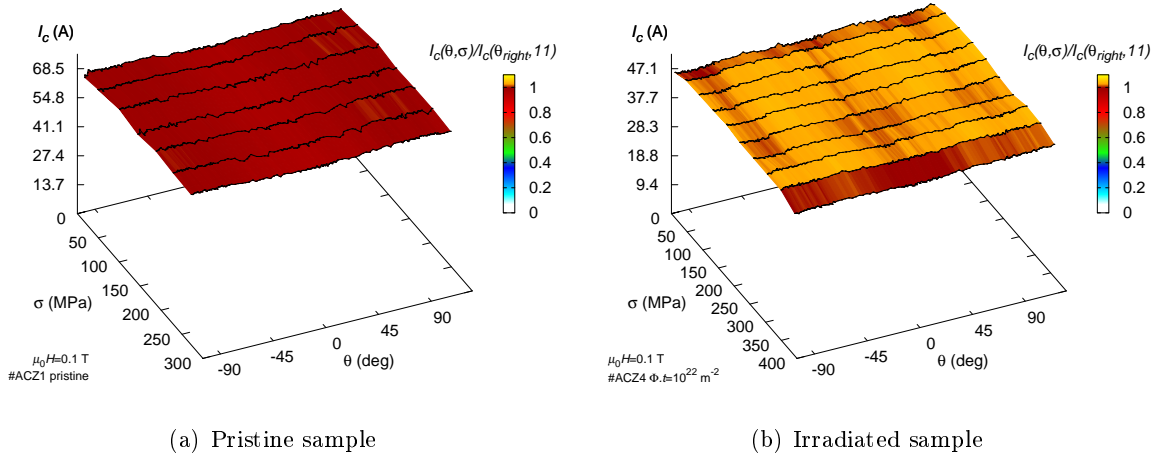


Figure D.39: Anisotropy of the AMSC 344C tape under tensile stress at $\mu_0 H=0.1$ T.

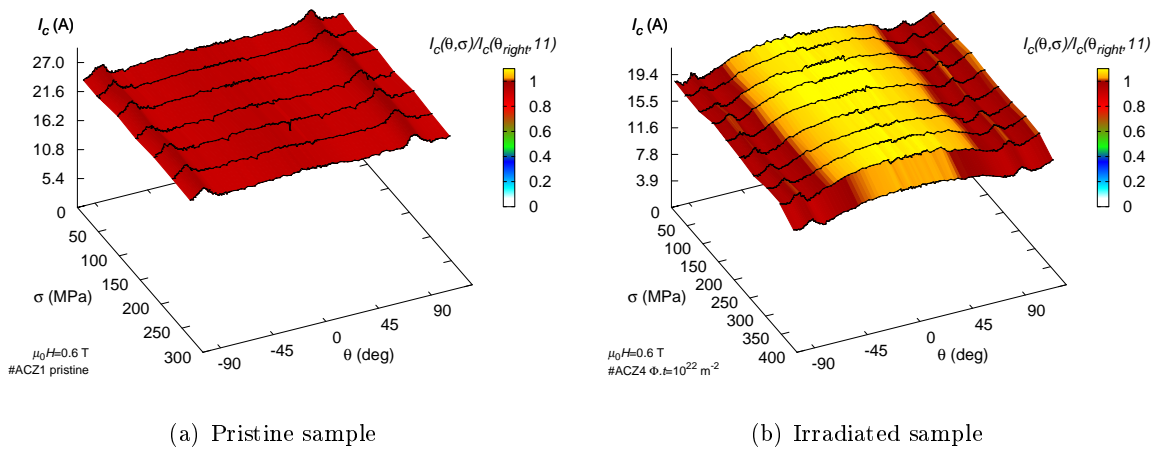


Figure D.40: Anisotropy of the AMSC 344C tape under tensile stress at $\mu_0 H=0.6$ T.

D Neutron irradiation

At 1.4 T, I_c is again the highest at $H||a,b$ in the pristine sample and the anisotropy is rather low (figure D.41(a)). The critical currents of the irradiated sample are enhanced for orien-

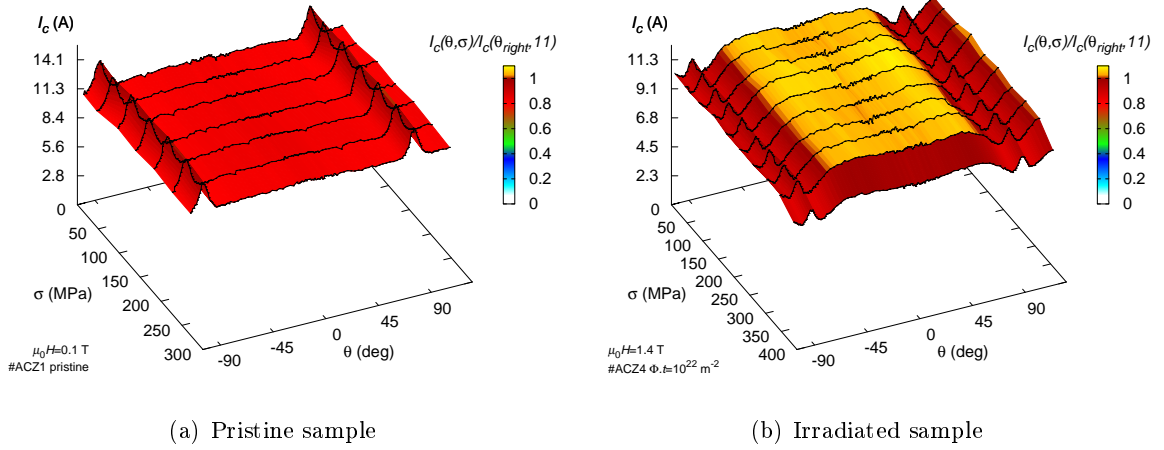


Figure D.41: Anisotropy of the AMSC 344C tape under tensile stress at $\mu_0 H = 1.4$ T.

tations around $H||c$ and local maxima occur around the a,b-peaks (figure D.41(b)). I_c for $H||c$ is nearly equal to the value of the pristine sample

According to figure D.17(a) on page 103, the Θ -dependence will not change significantly with even higher fields at this neutron fluence. Again, only a slight reduction of I_c occurs in relation to the applied force.

A detailed analysis of the stress dependence for $H||c$ and $H||a,b$ is shown in figures D.42 and D.43.

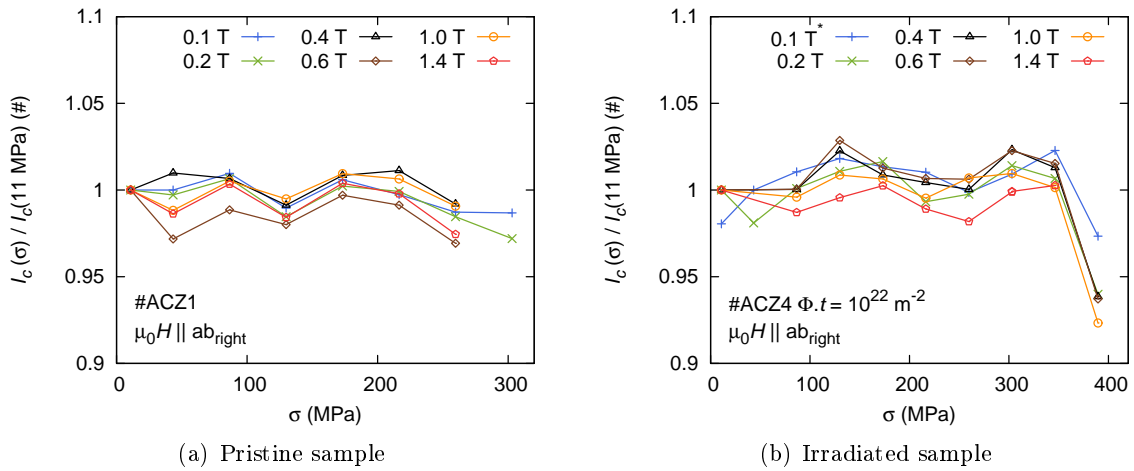


Figure D.42: Stress dependent I_c reduction for $H||a,b$.

D Neutron irradiation

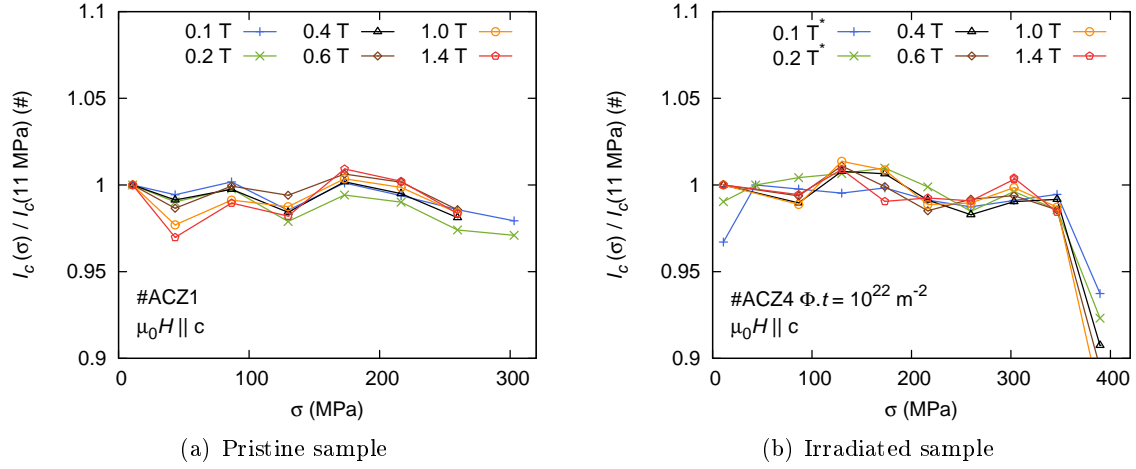


Figure D.43: Stress dependent I_c reduction for $H||c$.

The critical current of the pristine sample never decreases up to the maximum applied stress of 303 MPa (figure D.42(a)). The irradiated sample behaves similarly, but a degradation to $\approx 90\%$ of the initial value occurs at 389 MPa, slightly beyond the irreversible limit of 410 MPa (figure D.42(a)). A field dependence was not observed up to the second highest applied stress of 346 MPa. For the highest applied stress of 389 MPa, the degradation is clearly higher at higher fields. The critical current dependence on applied stress is similar for fields $H||a,b$ and $H||c$.

The stress sensitivity of the AMSC tape does not change after irradiation. Since the closeness of the temperature to the critical temperature is crucial for the change of I_c with applied stress/strain, the lower T_c of the SuperPower tape could be an explanation for the more pronounced change in sensitivity in the SuperPower sample. Hence, the point defects, which cause the T_c reduction, appear to be responsible for the increased stress sensitivity of the SuperPower conductor.

Note that the mechanical and irreversible limits remain more or less the same for both samples before and after neutron irradiation.

E Status of HTS coated conductors for fusion magnet coils

In this final chapter, the requirements on coated conductors specified in A.1 will be discussed.

High critical currents in high magnetic fields at high temperatures

The estimated critical engineering current density of $J_{c,E}^{Demo}(15\text{ T}) \approx 1.2 \cdot 10^8 \text{ Am}^{-2}$ was nearly reached ($\approx 0.9 \cdot 10^8 \text{ Am}^{-2}$) in the pristine SCS4050 conductor at 64 K for the field applied parallel to the a,b-planes. For fields parallel to the c-axis, the critical engineering current density is too low by about one order of magnitude. In 2008, the highest value of $J_{c,E}(15\text{ T}) \approx 0.5 \cdot 10^8 \text{ Am}^{-2}$ was reported in SuperPower YBCO coated conductors [3], which is about a factor of two lower than in the SuperPower SCS4050 conductor investigated in this work.

In recent years, the enhancement of the critical current density in coated conductors has been impressive. Furthermore, SmBCO conductors with increased superconducting layer thickness in short samples (centimetre range) reached about four times higher critical sheet current density when compared with the SuperPower sample of this work. If these remarkable improvements in coated conductor development continue, the desired engineering current densities at 64 K could be reached in the forthcoming years.

The conductor has to withstand neutron irradiation without a performance loss

Unfortunately, unlike YBCO coated conductors, GdBCO coated conductors were not able to withstand the full-neutron-spectrum irradiation of the TRIGA reactor without a significant loss of performance. The high neutron capture cross-section of gadolinium seems to be responsible for the strong reduction of T_c , as the recoil of the excited atoms, when emitting gamma rays, create point defects that disturb the superconducting phase. However, a fusion spectrum consists of significantly less thermal and epi-thermal neutrons (which are mainly captured by the Gd nucleus) than the fission spectrum of the TRIGA reactor. Therefore, the usability of gadolinium and samarium coated conductors for fusion magnet coils, needs to be further investigated.

At 64 K, the YBCO coated conductors investigated in this work always showed an enhancement of J_c at high fields after irradiation. Therefore, YBCO coated conductors once again demonstrate their ability to withstand neutron irradiation.

Homogeneity over long lengths of conductors:

Contrary to previous results [3], no significant local defects in today's commercially available coated conductors were found. Geometrical imperfections and local defects found in narrow prototype Roebel strands should be avoidable in the future. Striating Roebel strands by pico-seconds infra-red laser pulses seems to be a promising technique, as the filaments are well separated from each other by a tiny gap and the coupling is very weak. Nevertheless, the quality of the striated strand is limited by the homogeneity of the underlying coated conductor.

Current sharing between strands with low AC losses

Coupling losses of Roebel loops were investigated in detail. It was found that the losses strongly depended on the width of the tapes. Therefore, one should aspire narrow Roebel strands with small gaps between the strands, which should be filled nearly completely with transverse sections of the strands in order to lower the AC losses.

Currently, no coupled solutions for commercially available Roebel cables exist. The question of how to couple single strands (at certain points or throughout the entire cable) is still open.

Mechanical strength and a low stress dependence of I_c

In the pristine samples, the critical current of both YBCO and GdBCO coated conductors minimally depends on the applied stress. After irradiation, the critical current dependence on stress was significantly enhanced in the GdBCO conductor, whereas nearly no change was observed in the YBCO conductor. This effect is likely to be caused by the lower T_c in the irradiated GdBCO conductor, as the sensitivity of I_c on applied stress becomes higher at temperatures closer to T_c . However, the irreversible limits did not change after irradiation. The irreversible stress limits of coated conductors far exceed those of conventional Nb₃Sn conductors. The irradiated SuperPower tape showed a reversible behaviour up to 800 MPa, which is well beyond the (estimated) required irreversible limit of 500 MPa for a DEMO cable.

Cables with a large heat removal capability

The two main cable-concepts (Roebel cable and coaxial cable) based on coated conductors designs have a good heat removal capability because of the copper stabilisation. Nevertheless, an accurate prediction should consider the cable design and the coolant. Since neither the cable design nor the coolant is specified, this issue was not addressed in this work.

Easy to handle cables (preferably round)

As previously mentioned, the Roebel cable and the coaxial cable are both promising candidates for a future fusion cable design. The main advantage of the Roebel cable is the full

transposition of the strands. On the other hand, the overall current is reduced by self-field effects in the cable. Furthermore, its industrial assembly is rather complicated. Tensile stress applied to a Roebel cable might lead to defects at the (inner) corners of the strand. Therefore, the use of Roebel cables without mechanical reinforcement is questionable. A long length production of a Roebel cable is complicated, but was already demonstrated.

In contrast, the strands of a coaxial cable are not fully transposed, but the concept is easy to scale up and an industrial assembling process is already established. The coated conductors are wound under compressive stress in this cable and therefore the entire cable should withstand even higher stresses than single strands.

Currently, both concepts are subject to research and none of them has proven to be superior yet.

Materials should be inexpensive

(RE)BCO coated conductors are still by far more expensive than conventional LTS conductors. These costs need to be reduced if coated conductors were to be used in fusion coils. The higher costs compared to Nb_3Sn could nevertheless be partially balanced by several cost savings due to the higher operating temperature. Furthermore, radical cost cuts are expected, if thicker superconducting layers could be realised or if coated conductors could be manufactured by chemical methods.

It should be emphasized, once again, that the use of liquid helium as a coolant is no option for a sustainable energy source, since the amount of helium is limited on earth. Therefore, from today's perspective, HTS coated conductors are the only option for future fusion magnet coils.

Promising perspectives for coated conductors and cables for fusion magnet applications can be deduced from our results, but a substantial further development of conductors and cables is needed to meet the requirements of future nuclear fusion plants.

Bibliography

- [1] J. L. Duchateau, “EFDA Contract TW4-TMS-HTSMAG: First Intermediate Report,” *AIM/NTT-2006.004*, 2006.
- [2] C. Baker and M. Abdou, “STARFIRE – A Commercial Tokamak Fusion Power Plant Study,” *ANL/FPP-80-1*, 1980.
- [3] R. Fuger, “Analysis of high temperature superconductors for applications in fusion magnets,” Ph.D. dissertation, TU Wien, 2008.
- [4] M. Chudy, “High temperature superconductors for fusion magnets,” Ph.D. dissertation, TU Wien, 2010.
- [5] M. Eisterer, R. Fuger, M. Chudy, F. Hengstberger, and H. W. Weber, “Neutron irradiation of coated conductors,” *Superconductor Science and Technology*, vol. 23, no. 1, p. 014009, 2010.
- [6] H. Zohm, “What determines the size of DEMO?” Presented at the CMFT Seminar, Hefei, China, October 2010.
- [7] J. L. Duchateau and P. Hertout, “Which superconducting material for the toroidal field system of the fusion DEMO reactor?” *Journal of Physics: Conference Series*, vol. 97, no. 1, 2008.
- [8] M. N. Wilson, *Superconducting Magnets*. Oxford Science Publications, 1983.
- [9] ITER Organization, *Design Description Document, DDD 11 Magnet ITER_D_2MVZNX v2.2*. ITER project documentation, 2009.
- [10] —, *Design Description Document, DDD 1 Magnet, Conductor Design and Analysis*. ITER project documentation, 2001.
- [11] T. Lehner, “Development, Manufacturing and Applications of 2G HTS Wire at SuperPower.” Fall 2011 Workshop University of Illinois, Urbana, IL, U.S.A., November 2011.
- [12] J. D. Jorgensen, M. A. Beno, D. G. Hinks, L. Soderholm, K. J. Volin, R. L. Hitterman, J. D. Grace, I. K. Schuller, C. U. Segre, K. Zhang, and M. S. Kleefisch, “Oxygen ordering and the orthorhombic-to-tetragonal phase transition in $\text{YBa}_2\text{Cu}_3\text{O}_{7-x}$,” *Phys. Rev. B*, vol. 36, no. 7, pp. 3608–3616, September 1987.
- [13] T. G. Holesinger, L. Civale, B. Maiorov, D. M. Feldmann, J. Y. Coulter, D. J. Miller, V. A. Maroni, Z. Chen, D. C. Larbalestier, R. Feenstra, X. Li, Y. Huang, T. Kodankath, W. Zhang, M. W. Rupich, and A. P. Malozemoff, “Progress in nanoengineered microstructures for tunable high-current, high-temperature superconducting wires,” *Advanced Materials*, vol. 20, no. 3, pp. 391–407, 2008.

Bibliography

- [14] Y. Chen, V. Selvamanickam, Y. Zhang, Y. Zuev, C. Cantoni, E. Specht, M. P. Paranthaman, T. Aytug, A. Goyal, and D. Lee, “Enhanced flux pinning by BaZrO₃ and (Gd,Y)₂O₃ nanostructures in metal organic chemical vapor deposited GdYBCO high temperature superconductor tapes,” *Applied Physics Letters*, vol. 94, no. 6, p. 062513, 2009.
- [15] H. Hilgenkamp and J. Mannhart, “Grain boundaries in high- T_c superconductors,” *Rev. Mod. Phys.*, vol. 74, pp. 485–549, May 2002.
- [16] S. Graser, P. J. Hirschfeld, T. Kopp, R. Gutser, B. M. Andersen, and J. Mannhart, “How grain boundaries limit supercurrents in high-temperature superconductors,” *Nature Physics*, vol. 6, no. 8, pp. 609–614, 2010.
- [17] W. Goldacker, R. Nast, G. Kotzyba, S. I. Schlachter, A. Frank, B. Ringsdorf, C. Schmidt, and P. Komarek, “High current DyBCO-ROEBEL Assembled Coated Conductor (RACC),” *Journal of Physics: Conference Series*, vol. 43, no. 1, p. 901, 2006.
- [18] W. Goldacker, A. Frank, A. Kudymow, R. Heller, A. Kling, S. Terzieva, and C. Schmidt, “Status of high transport current ROEBEL assembled coated conductor cables,” *Superconductor Science and Technology*, vol. 22, no. 3, p. 034003 (10pp), 2009.
- [19] R. Badcock, N. Long, M. Mulholland, S. Hellmann, A. Wright, and K. Hamilton, “Progress in the Manufacture of Long Length YBCO Roebel Cables,” *IEEE Transactions on Applied Superconductivity*, vol. 19, no. 3, pp. 3244–3247, 2009.
- [20] S. Terzieva, M. Vojenčiak, F. Grilli, R. Nast, J. Šouc, W. Goldacker, A. Jung, A. Kudymow, and A. Kling, “Investigation of the effect of striated strands on the AC losses of 2G Roebel cables,” *Superconductor Science and Technology*, vol. 24, no. 4, p. 045001, 2011.
- [21] S. Schlachter, W. Goldacker, F. Grilli, R. Heller, and A. Kudymow, “Coated Conductor Rutherford Cables (CCRC) for High-Current Applications: Concept and Properties,” *Applied Superconductivity, IEEE Transactions on*, vol. 21, no. 3, pp. 3021–3024, June 2011.
- [22] J. Šouc, F. Gömöry, B. Klinčok, L. Frolek, M. Vojenčiak, A. Usoskin, and A. Rutt, “AC loss measurement of YBCO cable model,” *IEEE Transactions on Applied Superconductivity*, vol. 17, no. 2, pp. 1718–1721, 2007.
- [23] J. Šouc, M. Vojenčiak, and F. Gömöry, “Experimentally determined transport and magnetization ac losses of small cable models constructed from YBCO coated conductors,” *Superconductor Science and Technology*, vol. 23, no. 4, p. 045029, 2010.
- [24] D. C. van der Laan, X. F. Lu, and L. F. Goodrich, “Compact GdBa₂Cu₃O_{7- δ} coated conductor cables for electric power transmission and magnet applications,” *Superconductor Science and Technology*, vol. 24, no. 4, p. 042001, 2011.
- [25] D. C. van der Laan, L. F. Goodrich, and T. J. Haugan, “High-current dc power transmission in flexible RE-Ba₂Cu₃O_{7- δ} coated conductor cables,” *Superconductor Science and Technology*, vol. 25, no. 1, p. 014003, 2012.

Bibliography

- [26] D. C. Van Der Laan, D. Abraimov, A. A. Polyanskii, D. C. Larbalestier, J. F. Douglas, R. Semerad, and M. Bauer, “Anisotropic in-plane reversible strain effect in $Y_{0.5}Gd_{0.5}Ba_2Cu_3O_{7-\delta}$ coated conductors,” *Superconductor Science and Technology*, vol. 24, no. 11, p. 115010, 2011.
- [27] AdvancedConductorTechnologies. [Online]. Available: <http://advancedconductor.com/>
- [28] H. Weber, H. Böck, E. Unfried, and L. Greenwood, “Neutron dosimetry and damage calculations for the TRIGA MARK-II reactor in Vienna,” *Journal of Nuclear Materials*, vol. 137, no. 3, pp. 236 – 240, 1986.
- [29] M. Frischherz, M. Kirk, J. Farmer, L. Greenwood, and H. Weber, “Defect cascades produced by neutron irradiation in $YBa_2Cu_3O_{7-\delta}$,” *Physica C: Superconductivity*, vol. 232, no. 3–4, pp. 309 – 327, 1994.
- [30] M. Aleksa, P. Pongratz, O. Eibl, F. Sauerzopf, H. Weber, T. Li, and P. Kes, “TEM observation of neutron-induced collision cascades in Bi-2212 single crystals,” *Physica C: Superconductivity*, vol. 297, no. 3–4, pp. 171 – 175, 1998.
- [31] K. E. Sickafus, J. O. Willis, P. J. Kung, W. B. Wilson, D. M. Parkin, M. P. Maley, F. W. Clinard, C. J. Salgado, R. P. Dye, and K. M. Hubbard, “Neutron-radiation-induced flux pinning in Gd-doped $YBa_2Cu_3O_{7-x}$ and $GdBa_2Cu_3O_{7-x}$,” *Phys. Rev. B*, vol. 46, pp. 11 862–11 870, Nov 1992.
- [32] J. Šouc, F. Gömöry, and M. Vojenčiak, “Calibration free method for measurement of the ac magnetization loss,” *Superconductor Science and Technology*, vol. 18, no. 5, p. 592, 2005.
- [33] L. S. Lakshmi, K. P. Thakur, M. P. Staines, R. A. Badcock, and N. J. Long, “Magnetic AC loss characteristics of 2G roebel cable,” *IEEE Transactions on Applied Superconductivity*, vol. 19, no. 3, pp. 3361–3364, 2009.
- [34] Scientific python package. [Online]. Available: <http://www.scipy.org/>
- [35] E. H. Brandt and M. Indenbom, “Type-II-superconductor strip with current in a perpendicular magnetic field,” *Phys. Rev. B*, vol. 48, no. 17, pp. 12 893–12 906, November 1993.
- [36] K. Thakur, A. Raj, E. Brandt, and P. Sastry, “Frequency dependent magnetization of superconductor strip,” *Superconductor Science and Technology*, vol. 24, no. 4, p. 099501, 2011.
- [37] A. Stangl, “Projektarbeit: Wechselfeldverhalten von gekoppelten Hochtemperatur-supraleitern,” TU Wien, 2012.
- [38] E. Pardo, D. . Chen, A. Sanchez, and C. Navau, “The transverse critical-state susceptibility of rectangular bars,” *Superconductor Science and Technology*, vol. 17, no. 3, pp. 537–544, 2004.

Bibliography

- [39] A. A. B. Brojeny, Y. Mawatari, M. Benkraouda, and J. R. Clem, “Magnetic fields and currents for two current-carrying parallel coplanar superconducting strips in a perpendicular magnetic field,” *Superconductor Science and Technology*, vol. 15, no. 10, p. 1454, 2002.
- [40] R. M. Ainbinder and G. M. Maksimova, “Hysteretic characteristics of a double stripline in the critical state,” *Superconductor Science and Technology*, vol. 16, no. 8, p. 871, 2003.
- [41] N. V. Zhelezina and G. M. Maksimova, “Magnetic flux penetration into a superconducting double stripline with an edge barrier,” *Technical Physics Letters*, vol. 28, no. 7, pp. 618–620, 2002.
- [42] J. Emhofer, F. Hengstberger, M. Eisterer, H. Weber, S. Terzieva, W. Goldacker, R. Badcock, and N. Long, “Current and Field Distribution in Meandered Coated Conductors for Roebel Cables,” *IEEE Transactions on Applied Superconductivity*, vol. 21, no. 3, pp. 3389–3392, June 2011.
- [43] M. Eisterer, S. Haindl, T. Wojcik, and H. W. Weber, “’Magnetoscan’: a modified Hall probe scanning technique for the detection of inhomogeneities in bulk high temperature superconductors,” *Superconductor Science and Technology*, vol. 16, no. 11, p. 1282, 2003.
- [44] F. Hengstberger, M. Eisterer, M. Zehetmayer, and H. Weber, “Assessing the spatial and field dependence of the critical current density in YBCO bulk superconductors by scanning Hall probes,” *Superconductor Science and Technology*, vol. 22, no. 2, p. 025011, 2009.
- [45] M. Zehetmayer, R. Fuger, M. Eisterer, F. Hengstberger, and H. W. Weber, “Assessment of the local supercurrent densities in long superconducting coated conductors,” *Applied Physics Letters*, vol. 90, no. 3, p. 032506, 2007.
- [46] E. Zeldov, J. R. Clem, M. McElfresh, and M. Darwin, “Magnetization and transport currents in thin superconducting films,” *Phys. Rev. B*, vol. 49, no. 14, pp. 9802–9822, April 1994.
- [47] N. J. Long, R. Badcock, P. Beck, M. Mulholl, N. Ross, M. Staines, H. Sun, J. Hamilton, and R. G. Buckley, “Narrow strand YBCO Roebel cable for lowered AC loss,” *Journal of Physics: Conference Series*, vol. 97, no. 1, p. 012280, 2008.
- [48] SuperPower Inc. [Online]. Available: <http://www.superpower-inc.com>
- [49] American Superconductor. [Online]. Available: http://www.amsc.com/solutions-products/hts_wire.html
- [50] Bruker ETS. [Online]. Available: <http://www.bruker-est.com/ybco-tapes.html>
- [51] Fujikura Ltd. [Online]. Available: <http://www.fujikura.co.jp/eng/rd/field/mt.html#c5>
- [52] National Nuclear Data Center, Brookhaven National Laboratory ENDF/B-VII.1 library. [Online]. Available: <http://www.nndc.bnl.gov/>

Bibliography

- [53] M. W. Rupich, X. Li, C. Thieme, S. Sathyamurthy, S. Fleshler, D. Tucker, E. Thompson, J. Schreiber, J. Lynch, D. Buczek, K. DeMoranville, J. Inch, P. Cedrone, and J. Slack, "Advances in second generation high temperature superconducting wire manufacturing and R&D at American Superconductor Corporation," *Superconductor Science and Technology*, vol. 23, no. 1, p. 014015, 2010.
- [54] X. Li, M. Rupich, C. Thieme, M. Teplitsky, S. Sathyamurthy, E. Thompson, D. Buczek, J. Schreiber, K. DeMoranville, J. Lynch, J. Inch, D. Tucker, R. Savoy, and S. Fleshler, "The Development of Second Generation HTS Wire at American Superconductor," *Applied Superconductivity, IEEE Transactions on*, vol. 19, no. 3, pp. 3231–3235, June 2009.
- [55] Atominstitut, Vienna University of Technology. [Online]. Available: <http://www.ati.ac.at/>
- [56] M. Hronek, "Projektarbeit: Experimentelles Prototyping einer Messsteuerung unter Python," TU Wien, 2011.
- [57] V. Mishev, "Diplomarbeit: Aufbau eines Anisotropie-Messplatzes für Zugversuche an YBCO-Bandleitern," TU Wien, 2011.
- [58] Gnuplot 4.2. [Online]. Available: <http://www.gnuplot.info/>
- [59] Python interface to legendary Gnuplot program. [Online]. Available: <http://pygnuplot.sourceforge.net/>
- [60] LabJack U6 USB based measurement and automation device. [Online]. Available: <http://labjack.com/u6>
- [61] D. Dew-Hughes, "Flux pinning mechanisms in Typ II superconductors," *Phil. Mag.*, vol. 30, p. 293, 1974.
- [62] G. Brandstätter, M. C. Frischherz, L. Kratzwald, H. W. Weber, and A. E. Petrov, "Thermal-neutron-induced Gd-point defects in $\text{GdBa}_2\text{Cu}_3\text{O}_{7-\delta}$ ceramics," *Physica C: Superconductivity and its Applications*, vol. 307, no. 3-4, pp. 197–201, 1998.
- [63] L. Fernández, B. Holzapfel, F. Schindler, B. de Boer, A. Attenberger, J. Hänisch, and L. Schultz, "Influence of the grain boundary network on the critical current of $\text{YBa}_2\text{Cu}_3\text{O}_7$ films grown on biaxially textured metallic substrates," *Phys. Rev. B*, vol. 67, p. 052503, February 2003.
- [64] D. C. van der Laan, J. F. Douglas, C. C. Clickner, T. C. Stauffer, L. F. Goodrich, and H. J. N. van Eck, "Evidence that the reversible strain effect on critical current density and flux pinning in $\text{Bi}_2\text{Sr}_2\text{Ca}_2\text{Cu}_3\text{O}_x$ tapes is caused entirely by the pressure dependence of the critical temperature," *Superconductor Science and Technology*, vol. 24, no. 3, p. 032001, 2011.
- [65] U. Welp, M. Grimsditch, S. Fleshler, W. Nessler, J. Downey, G. W. Crabtree, and J. Guimpel, "Effect of uniaxial stress on the superconducting transition in $\text{YBa}_2\text{Cu}_3\text{O}_7$," *Physical Review Letters*, vol. 69, no. 14, pp. 2130–2133, 1992.

Bibliography

- [66] J. W. Ekin, *Experimental Techniques for Low Temperature Measurements*. Oxford University Press, 2006.
- [67] N. Cheggour, J. W. Ekin, C. C. Clickner, D. T. Verebelyi, C. L. H. Thieme, R. Feenstra, and A. Goyal, “Reversible axial-strain effect and extended strain limits in Y-Ba-Cu-O coatings on deformation-textured substrates,” *Applied Physics Letters*, vol. 83, no. 20, pp. 4223–4225, 2003.
- [68] Z. Chen, F. Kametani, Y. Chen, Y. Xie, V. Selvamanickam, and D. C. Larbalestier, “A high critical current density MOCVD coated conductor with strong vortex pinning centers suitable for very high field use,” *Superconductor Science and Technology*, vol. 22, no. 5, p. 055013, 2009.
- [69] D. C. Van Der Laan, J. W. Ekin, J. F. Douglas, C. C. Clickner, T. C. Stauffer, and L. F. Goodrich, “Effect of strain, magnetic field and field angle on the critical current density of $\text{YBa}_2\text{Cu}_3\text{O}_{7-\delta}$ coated conductors,” *Superconductor Science and Technology*, vol. 23, no. 7, p. 072001, 2010.

Curriculum vitae

Personal Information

Name	Johann Emhofer
Address	Lavendelweg 15 1220 Wien
Phone	+43 650 5642660
e-Mail	johann@emhofer.priv.at
Date of birth	01.09.1980

Education

Since 1/2009	Vienna University of Technology / Atominstitut PhD research: Analysis of coupled coated conductors for fusion magnet applications
2/2010-5/2010	Research stay at Industrial Research Limited, NZ Loss measurements on Roebel loops by a calibration-free method
10/2000-11/2008	Vienna University of Technology Study of physics Diploma thesis: Manufacturing and Characterisation of MgB ₂ /MgO mixed samples
10/2004-3/2005	Semester abroad at ETH Zürich Project work: Magnetic resonance imaging
9/1994-7/1999	HTL Donaustadt HTL (Höhere Technische Lehranstalt) is a secondary education school that permits students to acquire the university entry qualification and professional training at the same time. Specialisation: Telecommunication

Publications

- J. Emhofer, F. Hengstberger, M. Eisterer, H. Weber, S. Terzieva, W. Goldacker, R. Badcock, and N. Long,
“Current and field distribution in meandered coated conductors for Roebel cables,”
IEEE Transactions on Applied Superconductivity, vol. 21, no. 3, pp. 3389 –3392, June 2011.
- L. Lakshmi, N. Long, R. Badcock, M. Staines, Z. Jiang, K. Thakur, and J. Emhofer,
“Magnetic and transport ac losses in HTS Roebel cable,”
IEEE Transactions on Applied Superconductivity, vol. 21, no. 3, pp. 3311 –3315, June 2011.
- M. Eisterer, J. Emhofer, S. Sorta, M. Zehetmayer, and H. W. Weber,
“Connectivity and critical currents in polycrystalline MgB₂,”
Superconductor Science and Technology, vol. 22, no. 3, p. 034016, 2009.
- A. Shikov, V. Pantsyrny, N. Kozlenkova, L. Potanina, R. Vasilyev, I. Gubkin, E. Nikulenkov, J. Emhofer, M. Eisterer, and H. Weber,
“The Effect of Thermo-Mechanical Treatments on $J_c(T,B)$ and T_{cs} of Nb-Ti Strands,”
IEEE Transactions on Applied Superconductivity, vol. 19, no. 3, pp. 2540 –2543, June 2009.